OPTIMAL BEAMFORMING STRATEGIES AT MMWAVES FOR 5G+ NETWORKS

NANCY VARSHNEY

BHARTI SCHOOL OF TELECOMMUNICATION

INDIAN INSTITUTE OF TECHNOLOGY DELHI

APRIL 2023

OPTIMAL BEAMFORMING STRATEGIES AT MMWAVES FOR 5G+ NETWORKS

by

NANCY VARSHNEY

Bharti School of Telecommunication

Submitted
in fulfillment of the requirements of the degree of Doctor of Philosophy

to the

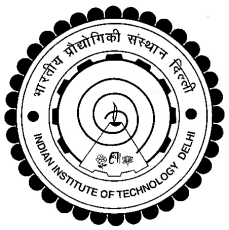

INDIAN INSTITUTE OF TECHNOLOGY DELHI

APRIL 2023

Certificate

This is to certify that the dissertation entitled **Optimal Beamforming Strategies at mmWaves for 5G+ Networks**, submitted by **Ms. Nancy Varshney**, a Research Scholar, in the *Bharti School Of Telecommunication*, *Indian Institute of Technology Delhi*, *New Delhi*, *India*, for the award of the degree of **Doctor of Philosophy**, is a record of an original research work carried out by her under my supervision and guidance. The dissertation fulfills all requirements as per the regulations of this Institute and in my opinion has reached the standard needed for submission. Neither this dissertation nor any part of it has been submitted for any degree or academic award elsewhere.

Prof. Swades De
(Supervisor)
Department of Electrical Engineering
Indian Institute of Technology Delhi
New Delhi, 110016, India.

Acknowledgements

First and foremost, thanks to the Almighty for showering his blessings on me that have helped in accomplishing this dissertation.

I would then like to express my sincere gratitude to my supervisor, Prof. Swades De, for giving me an opportunity to pursue Ph.D. at IIT Delhi. His passion for academia, discipline, and determination towards his work has always motivated me to work harder. His continuous guidance, valuable advice, and confidence in our pursued research work led to the fruition of this dissertation. It was a great privilege and honor to work under his supervision. I am extremely thankful to him for presenting me the opportunity to work as visiting scholar at Aalto University, Finland.

I would like to present my sincere gratitude to Prof. Riku Jäntii for his insightful advice during my research at Aalto University, Finland. I would then like to thank my committee members, Prof. Sheshan Srirangrajan, Prof. Prof. Aparna Mehra, and Prof. Arpan Chattopadhyay for their valuable suggestions that have helped address important aspects in this dissertation.

I take this opportunity to thanks Prof. K.V.S Srinivas from IIT (BHU) Varanasi for encouraging me to pursue career in research. I would like to thank my colleagues Dr. Suraj Suman, Dr. Vini Gupta, Mr. Ashutosh Balakrishnan, Ms. Ragini Jain, Ms. Kirandeep, and Dr. Farheen Chisti at IIT Delhi for their friendly support during this journey. I would also like to thank Dr. Reza Ghazalian at Aalto University, for having intellectual discussion that strengthened my research aptitude. I am grateful to all my seniors, lab-mates of the Communication Networks Research Group (CNRG), and friends at IIT Delhi, whose cooperation and encouragement have made this journey a memorable one.

Most importantly, I profoundly thanks my parents, Mr. Avdhesh Varshney and Mrs. Sarita Varshney, my brother Mr. Shubham Varshney, my sister-in-law Mrs. Nidhi Varshney and the other family members for their consistent support, and encouragement during my Ph.D. study. Without their constant support and inspiration, this acknowledgment and PhD dissertation would have never appeared. I am indebted to the sacrifices my parents

have made to shape my career and I dedicate this dissertation to them.

Nancy Varshney
(2018BSZ8118)

Abstract

Beyond fifth generation (5G+) communication aims to provide a 3-dimensional ubiquitous network to support high data rates caused by device proliferation. To aid 5G+ communications, three spectrum bands are being investigated: sub-6 GHz, millimeter-wave (mmWave), and terahertz frequencies. Higher frequency range has the advantage of increased bandwidth availability, but it also has its own set of challenges such as increased signal attenuation, reduced cell range, increased computational and hardware complexities, and increased hardware cost. However, substantial research has been conducted to demonstrate the feasibility of communication at higher frequencies. This dissertation focuses specifically on mmWave-enabled communications for serving users under different 2-dimensional as well as 3-dimensional network. The number of radio frequency (RF) chains that can be deployed at a device is a bottleneck in the mmWave range due to high hardware power consumption and hardware complexity. This, in turn, presents challenges in designing precoders and combiners, parameter estimation, signal processing, and user scheduling. Therefore, the objective of this dissertation is to investigate and design energy and spectrally efficient reduced complexity terrestrial and aerial mmWave communications frameworks/architectures with a limited number of RF chains.

The first topic investigates sectored-cell framework for a 2-dimensional multi-user terrestrial mmWave communications when the user population exceeds the number of RF chains available at the gNodeB. This framework is analyzed in the context of a single RF chain that serves all sectors of a cell in a round-robin manner with equal sector sojourn time. The idea is to partition the cell into identical sectors and serve multiple users simultaneously that fall within each sector at a given epoch using a single steerable beam generated from a uniform linear antenna array coupled to an RF chain at the gNodeB. Consequently, a large number of users are served with a limited number of RF chains. An optimization problem is formulated for combined resource allocation of orthogonal frequency division multiple (OFDM) symbols to users in a sector and sector beamwidth optimization in order to maximize average long-term user rate and system energy efficiency. Through simulation results, it is verified that serving multiple users over orthogonal frequency division multiple access with a single RF chain a sectored cell system model achieves better performance than serving single user per RF chain at a time. Additionally, the effect of localization error on the optimum beamwidth, which results from position estimation, is also studied.

The second part of the dissertation extends the study of the sectored-cell framework with a single RF chain to the case of multiple RF chains at gNodeB. Because of its low complexity, the sub-array based or partially connected hybrid precoder is considered, in which each RF chain, connected to a separate antenna array, generates one steerable beam. Notably, the presence of sidelobes causes inter-beam interference when concurrent beams are generated from multiple RF chains. Therefore, the optimal beamwidth is estimated while accounting for inter-beam interference and beam squint. Furthermore, an optimal number of RF chains at the gNodeB is estimated by accounting for power waste in RF units. A variable time frame structure for the sectored-cell framework is also proposed for a standalone mmWave communications system with variable transmission time interval units as short as one OFDM symbol long. The frame structure for enhanced mobile broadband (eMBB) services is typically made up of slots with a fixed number of OFDM symbols, and the smallest transmission time interval unit is equivalent to one slot duration, as defined by the 3rd Generation Partnership Project (3GPP) New Radio (NR) in Release 15. Furthermore, 3GPP guidelines have suggested a separate beam management phase for the initial gNodeB-user beam pair to establish the best gNodeB-user beam pair to be used for subsequent data transfer in data transmission mode. During the beam management phase, narrow beams must scan the area multiple times before granting users channel access. As a result, using a fixed frame structure along with separate beam management and data transmission phase causes significant initial access delays. Furthermore, because beam training overhead is often low for beam search operations, the wideband mmWave channel is underutilized during the beam training phase. Therefore, a modified sector-wise initial access procedure is proposed, which offers decreased initial access delay and increased bandwidth utilization. The proposed variable time frame structure, along with the modified initial access procedure, offers an improved average and the geometric mean of long-run user rates, especially in the case of non-homogeneous user distribution in the area.

The third part of the dissertation studies in detail the effect of beam squint in wideband mmWave communication. The beam squint effect is caused by the use of a large number of antenna elements connected per RF chain to generate a narrow beam in order to overcome high attenuation at mmWaves. The direction of maximum beam gain in beam squint varies with frequency. Based on this observation, a new reduced complexity joint OFDM resource allocation and beamforming strategy is proposed, which employs beam squint to maximize system performance using sub-array hybrid precoder at the transmit-

ter to serve a clustered user population greater than the number of RF chains. Numerical results demonstrate that the proposed sequence for designing RF precoder, baseband precoder, and subcarrier allocation using beam squint provides a greater increase in spectral efficiency at mmWaves than at sub-6 GHz.

The fourth part of the dissertation explores the feasibility of using an unmanned aerial vehicle (UAV) as a fronthaul unit at mmWaves and contrasts its performance with that at the sub-6 GHz range for ad hoc communication. The ideal user grouping method in a 3-dimensional environment with UAV-assisted mmWave communications is investigated for a system with a user population much higher than the number of RF chains available at the UAV. Similar to the analysis of multiple RF chains in terrestrial communication, multiple users per beam are served employing OFDMA. The optimal number of RF chains at the UAV is estimated to maximize the sum rate while satisfying minimum user rate specifications with a given UAV power constraint. Since UAV performance is constrained by battery size, so it is assumed that the UAV is equipped with a solar panel to harvest solar energy in order to increase operational hours. The effect of additional weight because of the solar panel on the performance of the UAV is also analyzed.

Finally, the dissertation's last part studies the feasibility of using an existing backscatter device infrastructure in an indoor environment to provide data support to an obstructed user at mmWaves. When in idle mode, the backscatter device is used to reflect the incoming signal to desired direction without modulating the data stream. This analogous to a distributed reconfigurable intelligent surface (RIS) system in which the tags acts as distributed RIS in indoor environment. Both users and backscatter devices in the mmWave range will have multiple antenna elements, increasing the system's complexity. The challenge, however, is to estimate the angle's direction using a single RF chain at the user. Therefore, a link establishment procedure is proposed that includes estimation of angle of arrival using the retro-reflective property of the antenna array, beamforming design at the user, and beamforming at the backscatter devices.

सार

पांचवीं पीढ़ी (5G+) से परे संचार का उद्देश्य 3-आयामी सर्वव्यापी प्रदान करना है उपकरण प्रसार के कारण उच्च डेटा दरों का समर्थन करने के लिए नेटवर्क। 5G+ की सहायता के लिए संचार, तीन स्पेक्ट्रम बैंड की जांच की जा रही है: उप-6 गीगाहर्ट्ज, मिलीमीटरवेव (mmWave), और टेराहर्ट्ज़ फ़्रीक्वेंसी। उच्च आवृत्ति रेंज का लाभ है बढ़ी हुई बैंडविड्थ उपलब्धता, लेकिन इसकी अपनी चुनौतियों का एक सेट भी है जैसे कि वृद्धि सिग्नल क्षीणन, कम सेल रेंज, कम्प्यूटेशनल और हार्डवेयर जटिलताओं में वृद्धि, और हार्डवेयर लागत में वृद्धि हुई। हालाँकि, पर्याप्त शोध किया गया है उच्च आवृत्तियों पर संचार की व्यवहार्यता प्रदर्शित करने के लिए। यह शोध प्रबंध विशेष रूप से अलग-अलग के तहत उपयोगकर्ताओं की सेवा के लिए एमएमवेव-सक्षम संचार पर ध्यान केंद्रित करता है 2-आयामी और साथ ही 3-आयामी नेटवर्क। रेडियो आवृत्ति की संख्या (आरएफ) श्रृंखलाएं जिन्हें डिवाइस पर तैनात किया जा सकता है, एमएमवेव रेंज में एक बाधा है उच्च हार्डवेयर बिजली की खपत और हार्डवेयर जटिलता के लिए। यह, बदले में, प्रस्तुत करता है प्रीकोडर और कंबाइनर डिजाइन करने में चुनौतियां, पैरामीटर अनुमान, सिग्नल प्रोसेसिंग, और उपयोगकर्ता शेड्यूलिंग। इसलिए, इस शोध प्रबंध का उद्देश्य जांच करना है और डिजाइन ऊर्जा और वर्णक्रमीय रूप से कुशल कम जटिलता स्थलीय और हवाई mmWave संचार ढांचे/आर्किटेक्चर सीमित संख्या में आरएफ श्रृंखलाओं के साथ।

पहला विषय द्वि-आयामी बहु-उपयोगकर्ता के लिए सेक्टर-सेल ढांचे की जांच करता है स्थलीय mmWave संचार जब उपयोगकर्ता जनसंख्या की संख्या से अधिक हो जीएनओडीबी पर उपलब्ध आरएफ चेन। इस ढांचे का विश्लेषण एक के संदर्भ में किया जाता है आरएफ श्रृंखला जो एक सेल के सभी क्षेत्रों को समान क्षेत्र के साथ राउंड-रॉबिन तरीके से सेवा प्रदान करती है ठहरने का समय। विचार यह है कि सेल को समान क्षेत्रों में विभाजित किया जाए और कई की सेवा की जाए एक साथ उपयोगकर्ता जो एक ही स्टीयरेबल का उपयोग करके किसी दिए गए युग में प्रत्येक क्षेत्र में आते हैं पर एक आरएफ श्रृंखला के लिए युग्मित एक समान रैखिक एंटीना सरणी से उत्पन्न बीम gNodeB. नतीजतन, बड़ी संख्या में उपयोगकर्ताओं को सीमित संख्या में आरएफ के साथ सेवा दी जाती है जंजीर। ऑर्थोगोनल के संयुक्त संसाधन आवंटन के लिए एक अनुकूलन समस्या तैयार की जाती है एक सेक्टर और सेक्टर में उपयोगकर्ताओं के लिए फ्रीक्वेंसी डिवीजन मल्टीपल (ओएफडीएम) प्रतीक औसत दीर्घकालिक उपयोगकर्ता दर और सिस्टम ऊर्जा को अधिकतम करने के लिए बीमविड्थ अनुकूलन क्षमता। सिमुलेशन परिणामों के माध्यम से, यह सत्यापित किया जाता है कि कई उपयोगकर्ताओं को

सेवा प्रदान की जा रही है ऑर्थोगोनल फ्रीक्वेंसी डिवीजन मल्टीपल एक्सेस एक सिंगल आरएफ चेन के साथ एक सेक्टर सेल सिस्टम मॉडल एक समय में प्रति आरएफ श्रृंखला एकल उपयोगकर्ता की सेवा से बेहतर प्रदर्शन प्राप्त करता है। इसके अतिरिक्त, इष्टतम बीमविड्थ पर स्थानीयकरण त्रुटि का प्रभाव, जिसके परिणामस्वरूप स्थिति अनुमान से भी अध्ययन किया जाता है।

शोध प्रबंध का दूसरा भाग सेक्टर-सेल ढांचे के अध्ययन का विस्तार करता है gNodeB पर एकाधिक RF श्रृंखलाओं के मामले में एकल RF श्रृंखला के साथ। इसके कम होने के कारण जटिलता, उप-सरणी आधारित या आंशिक रूप से जुड़े हाइब्रिड प्रीकोडर को माना जाता है जो प्रत्येक आरएफ श्रृंखला, एक अलग एंटीना सरणी से जुड़ा हुआ है, एक स्टीयरेबल बीम उत्पन्न करता है। विशेष रूप से, साइडलोब्स की उपस्थिति समवर्ती बीम के दौरान इंटर-बीम हस्तक्षेप का कारण बनती है कई आरएफ श्रृंखलाओं से उत्पन्न होते हैं। इसलिए, इष्टतम बीमविड्थ का अनुमान है इंटर-बीम हस्तक्षेप और बीम स्किंट के लिए लेखांकन करते समय। इसके अलावा, एक इष्टतम जीएनओडीबी में आरएफ श्रृंखलाओं की संख्या का अनुमान आरएफ में बिजली की बर्बादी के हिसाब से लगाया जाता है इकाइयों। सेक्टर-सेल ढांचे के लिए एक परिवर्तनीय समय सीमा संरचना भी प्रस्तावित है परिवर्तनीय संचरण समय अंतराल के साथ एक स्टैंडअलोन एमएमवेव संचार प्रणाली इकाइयां एक ओएफडीएम प्रतीक जितनी छोटी होती हैं। उन्नत मोबाइल के लिए फ्रेम संरचना ब्रॉडबैंड (eMBB) सेवाएं आमतौर पर निश्चित संख्या में OFDM वाले स्लॉट से बनी होती हैं प्रतीक, और सबसे छोटी संचरण समय अंतराल इकाई एक स्लॉट अवधि के बराबर है, रिलीज में तीसरी जनरेशन पार्टनरशिप प्रोजेक्ट (3GPP) न्यू रेडियो (NR) द्वारा परिभाषित के रूप में 15. इसके अलावा, 3GPP दिशानिर्देशों ने इसके लिए एक अलग बीम प्रबंधन चरण का सुझाव दिया है उपयोग किए जाने वाले सर्वोत्तम gNodeB-उपयोगकर्ता बीम जोड़ी को स्थापित करने के लिए प्रारंभिक gNodeB-उपयोगकर्ता बीम जोड़ी डेटा ट्रांसमिशन मोड में बाद के डेटा ट्रांसफर के लिए। बीम प्रबंधन के दौरान चरण, उपयोगकर्ताओं को चैनल देने से पहले संकीर्ण बीम को क्षेत्र को कई बार स्कैन करना चाहिए पहुँच। नतीजतन, अलग बीम प्रबंधन के साथ एक निश्चित फ्रेम संरचना का उपयोग करना और डेटा ट्रांसमिशन चरण महत्वपूर्ण प्रारंभिक पहुँच विलंब का कारण बनता है। इसके अलावा, क्योंकि बीम सर्च ऑपरेशंस, वाइडबैंड एमएमवेव के लिए बीम ट्रेनिंग ओवरहेड अक्सर कम होता है बीम प्रशिक्षण चरण के दौरान चैनल का कम उपयोग किया जाता है। इसलिए, एक संशोधित क्षेत्रवार प्रारंभिक पहुँच प्रक्रिया प्रस्तावित है, जो प्रारंभिक पहुँच विलंब को कम करती है और बैंडविड्थ उपयोग में वृद्धि। प्रस्तावित परिवर्तनीय समय सीमा संरचना, साथ में संशोधित प्रारंभिक पहुंच प्रक्रिया, एक बेहतर औसत और ज्यामितीय माध्य प्रदान करती है लंबी अवधि की उपयोगकर्ता दरों में, विशेष

रूप से गैर-सजातीय उपयोगकर्ता वितरण के मामले में क्षेत्र।

शोध प्रबंध के तीसरे भाग में वाइडबैंड में बीम स्क्विंट के प्रभाव का विस्तार से अध्ययन किया गया है एमएमवेव संचार। बीम स्क्विंट प्रभाव बड़ी संख्या के उपयोग के कारण होता है एक संकीर्ण बीम उत्पन्न करने के लिए प्रति आरएफ श्रृंखला से जुड़े एंटीना तत्वों की संख्या mmWaves पर उच्च क्षीणन पर काबू पाएं। बीम में अधिकतम बीम लाभ की दिशा भेंगापन आवृत्ति के साथ बदलता रहता है। इस अवलोकन के आधार पर, एक नया कम जटिल जोड़ओएफडीएम संसाधन आवंटन और बीमफॉर्मिंग रणनीति प्रस्तावित है, जो बीम को नियोजित करती है ट्रांसमीटर पर उप-सरणी हाइब्रिड प्रीकोडर का उपयोग करके सिस्टम प्रदर्शन को अधिकतम करने के लिए भेंगापन आरएफ श्रृंखलाओं की संख्या से अधिक संकुल उपयोगकर्ता आबादी की सेवा करने के लिए। न्यूमेरिकल परिणाम प्रदर्शित करते हैं कि आरएफ प्रीकोडर, बेसबैंड प्रीकोडर डिजाइन करने के लिए प्रस्तावित अनुक्रम, और बीम स्क्विंट का उपयोग करते हुए सबकैरियर आवंटन वर्णक्रमीय में अधिक वृद्धि प्रदान करता है उप -6 गीगाहर्ट्ज की तुलना में एमएमवेव्स पर दक्षता।

शोध प्रबंध का चौथा भाग मानव रहित हवाई का उपयोग करने की व्यवहार्यता की पड़ताल करता है mmWaves पर एक फ्रंटहॉल इकाई के रूप में वाहन (यूएवी) और उसके साथ इसके प्रदर्शन की तुलना करता है तदर्थ संचार के लिए उप-6 गीगाहर्ट्ज रेंज में। ए में आदर्श उपयोगकर्ता समूहीकरण विधि यूएवी-समर्थित एमएमवेव संचार के साथ 3-आयामी वातावरण की जांच की जाती है उपलब्ध आरएफ श्रृंखलाओं की संख्या की तुलना में बहुत अधिक उपयोगकर्ता आबादी वाली प्रणाली के लिए यूएवी। स्थलीय संचार में एकाधिक आरएफ श्रृंखलाओं के विश्लेषण के समान, एकाधिक प्रति बीम उपयोगकर्ताओं को OFDMA नियोजित किया जाता है। आरएफ श्रृंखलाओं की इष्टतम संख्या न्यूनतम उपयोगकर्ता दर विनिर्देशों को संतुष्ट करते हुए यूएवी को योग दर को अधिकतम करने का अनुमान है किसी दिए गए यूएवी पावर की कमी के साथ। चूंकि यूएवी का प्रदर्शन विवश है बैटरी का आकार, इसलिए यह माना जाता है कि यूएवी सौर फसल के लिए सौर पैनल से लैस है परिचालन घंटे बढ़ाने के लिए ऊर्जा। अतिरिक्त वजन के प्रभाव के कारण यूएवी के प्रदर्शन पर सौर पैनल का भी विश्लेषण किया जाता है।

अंत में, निबंध का अंतिम भाग मौजूदा बैकस्कैटर का उपयोग करने की व्यवहार्यता का अध्ययन करता है किसी बाधित को डेटा समर्थन प्रदान करने के लिए एक इनडोर वातावरण में उपकरण अवसंरचना एमएमवेव्स पर उपयोगकर्ता। निष्क्रिय मोड में होने पर, बैकस्कैटर डिवाइस का उपयोग इनकमिंग को दर्शाने के लिए किया जाता है डेटा स्ट्रीम को संशोधित किए बिना वांछित दिशा में संकेत।

यह ए के अनुरूप है वितरित पुनर्विन्यास योग्य बुद्धिमान सतह (आरआईएस) प्रणाली जिसमें टैग वितरित के रूप में कार्य करता है इनडोर वातावरण में आरआईएस। mmWave में उपयोगकर्ता और बैकस्कैटर डिवाइस दोनों रेंज में कई एंटेना तत्व होंगे, जो सिस्टम की जटिलता को बढ़ाएंगे। चुनौती, हालाँकि, उपयोगकर्ता पर एकल RF श्रृंखला का उपयोग करके कोण की दिशा का अनुमान लगाना है। इसलिए, एक लिंक स्थापना प्रक्रिया प्रस्तावित है जिसमें कोण का अनुमान शामिल है ऐन्टेना ऐरे के रेट्रो-रिफ्लेक्टिव गुण का उपयोग करते हुए, बीमफॉर्मिंग डिज़ाइन पर उपयोगकर्ता, और बैकस्कैटर उपकरणों पर बीमफॉर्मिंग।

Contents

List of Figures

List of Tables

List of Symbols

$\mathbf{a} \in \mathbb{R}^{N \times 1}$	A real vector of size $N \times 1$
$\mathbf{A} \in \mathbb{R}^{M \times N}$	A real-valued matrix of size $M \times N$
$\mathbf{0}_{M \times N}$	$M \times N$ matrix of zeros
$\boldsymbol{I}_N$	$N \times N$ identity matrix
$\mathbf{A}_{m,n}$	$(m,n)^{th}$ element of the matrix $\mathbf{A}$
$\text{Tr}\{\mathbf{A}\}$	Trace of the matrix $\mathbf{A}$
$\mathbf{a}[m]$	m^{th} element of the vector $\mathbf{a}$
$\|\mathbf{a}\|_2$	Standard l_2-norm of the vector $\mathbf{a}$
$(\cdot)^T$	Transpose of the vector/matrix
$(\cdot)^H$	Transpose of the vector/matrix
$(\cdot)^\dagger$	Moore-Penrose pseudo inverse of the vector/matrix
$\text{diag}(\cdot)$	Standard diagonalization operation on a vector
$\|\cdot\|$	Cardinality operation
$\bigcup$	Set union operation
dom f	Domain of the function f
$\mathcal{O}$	Algorithm run-time complexity
$\mathcal{L}(\cdot)$	Lagrangian operator

List of Abbreviations

mmWave	Millimeter Wave
5G+	Beyond 5th Generation
RF	Radio Frequency
OFDM	Orthogonal Frequency Division Multiplexing
OFDMA	Orthogonal Frequency Division Multiple Access
eMBB	enhanced Mobile Broadband
NR	New Radio
UAV	Unmanned Aerial Vehicle
RIS	Reconfigurable Intelligent Surface
WLAN	Wireless Local Area Network
UE	User Equipment
gNB	gNodeB
LoS	Line-of-Sight
SNR	Signal-to-Noise Ratio
ADC	Analog-to-Digital Converter
DAC	Digital-to-Analog Converter
SDMA	Spatial Division Multiplexing
MIMO	Multiple-Input-Multiple-Output
JSDM	Joint Spatial Division Multiplexing
WMMSE	Wegihted Minimum Mean Squared Error
MPC	Multi Path Component
CSI	Channel State Information
SVD	Singular Value Decomposition
ML	Maximum Likelihood
AoA	Angle-of-Arrival
DFT	Discrete Fourier Transform

MUSIC	MUltiple Signal Classification
TTI	Transmission Time Interval
3GPP	3rd Generation Partnership Project
HPBW	Half Power BeamWidth
IA	Initial Access
EIRP	Effective Isotropic Radiated Power
GPS	Global Positioning System
ToA	Time-of-Arrival
QoS	Quality-of-Service
2-D	2-Dimensional
ULA	Uniform Linear Array
NLoS	Non Line-of-Sight
NP	Non-deterministic Polynomial time
KKT	Karush-Kuhn-Tucker
MOP	Multi-objective Optimization Problem
SOP	Single-objective Optimization Problem
FNBW	First Null BeamWidth
EAoA	Effective AoA
CRLB	Cramér-Rao Lower Bound
FIM	Fisher Information Matrix
PEB	Position Error Bound
SA	StandAlone
NSA	Non-StandAlone
UL	UpLink
DL	DownLink
TDMA	Time Division Multiple Access

UMi	Uran-Micro
WRR	Weighted Round Robinn
SS	Synchronization Signal
RACH	Random Access CHannel
PRACH	Physical Random Access CHannel
RAR	Random Acceess Response
PDCCH	Physical Downlink Control CHannel
PUCCH	Physical Uplink Control CHannel
IAD	Initial Access Delay
IUI	Inter-User Interference
s.t.	such that
UPA	Uniform Planar Array
ZF	Zero-Forcing
MMSE	Minimum Mean Squared Error
PV	PhotoVoltaic
AP	Access Point
OMP	Orthogonal Matching Pursuit
AEB	Angle Error Bound
RMSE	Root Mean Squared Error

Chapter 1

Introduction

1.1 Background

Wireless networks handle more traffic than ever as more people and devices consume more data. There are two methods to improve the efficiency of wireless communication networks. The first strategy is to increase the channel's spectral efficiency, which has already been extensively researched. The second option is to increase the bandwidth availability. However, all traffic is congested on the same radio-frequency spectrum bands. The bandwidth bottleneck at the microwave frequency spectrum has become a driving factor in investigating higher frequency bands for the beyond fifth generation (5G+) communication wireless networks. The millimeter wave (mmWave) band, which spans 30 to 300 GHz, offers massive bandwidth and has thus been proposed as an essential component of the 5G+ technology for providing multi-gigabit indoor and outdoor communication services. The emergence of the IEEE 802.11ad wireless local area network (WLAN) standard at 60 GHz [1] demonstrates the viability of indoor implementation of mmWave communications. The frequency bands proposed for outdoor mmWave communications are centered at 28 GHz, 38 GHz, 73 GHz, and in the 81–86 GHz range, depending on considerations of high propagation and penetration losses [2]. Currently, parts of the mmWave spectrum are mostly used by satellite and radar operators, but their applications are expanding to medicine, astronomy, meteorology, and communications. Future 5G+ networks will incorporate mmWave technology in conjunction with other 5G+ technologies such as mobile edge computing, unmanned aerial vehicles (UAVs), reconfigurable intelligent surfaces (RIS), backscatter communication, and integrated communication and sensing.

The 5G+ communication envisions to provide 3D ubiquitous coverage. UAV-assisted communication integrated with terrestrial communication will play a vital role in delivering unprecedented coverage. Inherent ease of deployment and freedom of movement will allow UAVs to act as aerial base stations and aerial relays. A UAV provide a higher probability for line-of-sight (LoS) links, and can be flexibly deployed cost-effectively to support high-rate communication for remote areas or emergency situations. This is especially helpful at mmWaves, where terrestrial communication often suffers complete blockage of signals from buildings, trees, humans, etc., [3, 4]. The study in [5, 6] conducted ray-tracing simulations using the Wireless Insite tool by Remcom to study the urban air-to-ground channel for UAVs deployed at low altitudes of 80-120 meters at 28 GHz and observed that coverage improves up to certain altitudes because of better LoS connectivity that in turn improves the achievable SNR.

In addition, RIS will further provide a cost-effective solution to overcome the drawbacks of mmWave communications [7]. The RIS can be set to relay mmWave signals via pencil beams to circumvent obstructions between transmitter and receiver, thereby establishing a virtual LoS link and enhancing the system's spectral efficiency at a reduced capital cost. Another contemporary technology is backscatter communication that will play a crucial role in the development of smart indoor environments in near future by connecting low-power wireless devices. By leveraging the existing backscatter infrastructure, the performance of an indoor mmWave communication system can be improved without incurring any extra capital cost.

The later part of this dissertation explores the integration of mmWave with two significant technologies, namely UAV and backscatter device as RIS , to provide services to user equipment (UE) that suffers from the obstruction of their direct link from the serving gNodeB (gNB).

1.2 Beamforming at mmWaves

Even though mmWave frequency bands have a lot of potential owing to their considerable bandwidth, the signal path loss at mmWaves is several dB more than legacy sub-6 GHz bands. Fortunately, the tiny wavelengths of mmWave frequencies allow for the packaging of a large number of antenna components to be placed in the same area. Thus, multiple antennas are used to achieve antenna gain to overcome the large path loss [8]. Multiple antenna technology is a key enabler in implementing effective mmWave communication

systems. A multiple antenna structure can be designed in numerous ways to achieve various objectives. The first is to achieve antenna gain, which involves using all antennas connected to a radio frequency (RF) chain to create a single highly directive beam to improve the signal-to-noise ratio (SNR). This is also known as analog beamforming. An RF chain typically includes oscillators, a mixer, an analog-to-digital converter (ADC)/digital-to-analog converter (DAC), filters, and amplifiers. The second objective is to provide diversity gain by generating multiple low directivity beams that transmit redundant data streams to improve the bit error rates. The third objective is to provide to provide multiplexing gain by generating multiple low directivity beams for simultaneous data streams to increase spectral efficiency, also known as spatial division multiple access (SDMA). In legacy sub-6 GHz communication systems, the multiple-input-multiple-output (MIMO) concept, also called digital beamforming, is employed wherein multiple antennas connected to an equal number of RF chains are used to achieve either diversity gain or multiplexing gain [9]. In MIMO technology, the output beam radiation pattern is controlled by adjusting the angle and magnitude of each antenna's signals to constructively or destructively add signals at the desired location.

Utilizing a large number of power-hungry RF chains at mmWaves, as in digital beamforming, is not viable. In contrast, analog beamforming utilities a single RF chain, resulting in significantly lower power usage. However, it only allows for generating a single beam, and spatial data stream multiplexing is not possible. Therefore, hybrid beamforming has been presented in the literature as a trade-off between analog and digital beamforming. It provides increased spectrum efficiency over analog beamforming by consuming less energy than digital beamforming. A hybrid beamformer has N_{RF} RF chains connected to N_t antenna elements such that $N_t \gg N_{RF}$, capable of generating N_{RF} data streams simultaneously. A survey in [10] discussed various hybrid precoding architectures in indoor and outdoor mmWave communications. A hybrid precoder architecture can be either a fully-connected type or a partially-connected (also known as a subarray) type. In fully-connected hybrid precoder architecture, all the N_t antenna elements are connected to all N_{RF} RF chains using adders. In partially-connected hybrid precoder architecture, N_t antenna elements are divided into non-overlapping sets, and each set of antenna elements is connected to a single RF chain [11, 12].

A multi-antenna mmWave communication system requires joint optimization of the beamformer at the gNB and combiner at UE. Further, in a UAV-assisted mmWave communication system, the UAV serves as a fronthaul unit and is connected via a backhaul

link to a nearby terrestrial gNB. Therefore, it requires joint optimization of beamforming designs at the gNB, the UAV, and the UE. On the contrary, in an RIS-assisted mmWave communication system, the RIS acts as a passive relay. In general, a RIS consists of a large number of reflecting elements where each element can be reconfigured independently of others. Because of the passive nature of RIS, the joint optimization of beamforming designs for gNB, UE, and RIS is much more challenging [13].

1.3 Prior Art on Beamforming at mmWaves

The main challenge of hybrid beamforming design is to optimize the system performance under constraints of reduced RF chains and reduced signaling overhead. Due to complex-interconnected architecture, the signal processing of a fully-connected hybrid precoder is difficult, and hence, a partially-connected hybrid precoder is preferred over it [12]. The survey in [10] presented key beamforming techniques to design hybrid precoders like codebook-based design, compressive sensing-based design, machine learning-based design, and optimization-based designs. Furthermore, hybrid precoding algorithms have been optimized for single UE, multi-UE, and MIMO mmWave systems over both wideband frequency-selective and narrowband channels. Additionally, several beamforming concepts have been put forth in the literature for RIS-assisted communication systems and UAV-assisted mmWave communication systems. Following is a brief overview of the pertinent literature relevant to this dissertation.

1.3.1 Beamforming in Wideband mmWave System

Most of the prior works on mmWaves consider narrowband channels [11,12,14], whereas practical mmWave channel is frequency-selective due to large bandwidth and beam squint effect. For the wideband mmWave channel, the authors in [15] designed a hybrid precoder using a single-carrier and assigned different numbers of data streams to the UEs equipped with multiple RF chains. Some of the existing works on multi-user hybrid beamforming on wideband mmWave channel focused on using spatial division multiple access (SDMA) and obtained orthogonality on data streams to UEs via joint RF and baseband precoding schemes based on channel information and correlation. To use wideband channel effectively, in [16], different UEs were multiplexed over different subcarriers of the OFDM symbol, using a fully-connected hybrid precoder at the gNB. However, each UE data

stream was modulated using a separate RF chain, hence requiring $N_{RF} = M$. Similarly, work in [17, 18] scheduled UEs so as to provide a dedicated beam per UE based on the assumption of sparse UE distribution.

With the growing number of data-intensive devices, thousands of mobile devices will be used per square kilometer area. Therefore, serving each UE by a dedicated RF chain might not be possible as it would significantly increase the hardware cost and power consumption of the gNB. When $M \gg N_{RF}$, to maximize the multi-UE diversity, sub-optimal SDMA schemes were considered with UE scheduled in the time domain. In [19], the authors suggested grouping of UEs based on the correlation in angular dimension using joint spatial division multiplexing (JSDM) algorithm, with data of each UE being modulated by a separate RF chain. In this algorithm, the baseband-RF precoding of a hybrid precoder, having each of the N_{RF} RF chains connected to all the N_t antenna elements (fully-connected structure), was implemented in two stages. However, as stated in [19], the selection of the number of eigenmodes during pre-beamforming in JSDM is a non-trivial optimization problem. This approach gets complex with an increased UE population, as it creates additional inter-group interference (a result of imperfect block diagonalization). The complexity of grouping M UEs in a pre-beamforming algorithm at the RF level increases with M as $\mathcal{O}(M^2)$. Besides high complexity, the selection of appropriate N_{RF} is itself challenging while keeping hardware cost and power within budget. A low-complexity selection combining algorithm was proposed in [20] to cater to high UE density by scheduling only a subset of UEs with good channel conditions in the time domain. In [21], a subchannel constrained fully-connected hybrid precoding was designed over OFDM symbol with a limit on the total number of UEs per subcarrier. The authors assumed a prior UE-subcarrier allocation to jointly design the RF and baseband precoders. To serve multiple UEs using OFDM, authors in [22] used sparsity-based digital precoding to jointly estimate subcarrier and hybrid precoder design for a fully-connected hybrid architecture wherein they used weighted minimum mean squared error (WMMSE) method to optimize baseband precoder [22].

1.3.2 Beamforming for UAV-assisted Wideband mmWave System

The majority of research work on UAV-assisted communication has been undertaken in the sub-6 GHz frequencies, covering optimal 3D placement, path planning, channel modeling, backhaul connectivity, security and privacy challenges, energy limitations, and

many other [23, 24]. However, the sub-6 GHz study cannot be applied to mmWaves since its channel model, and antenna designs are different [25]. For different UAV heights and blockage scenarios, the authors in [26] investigated the mmWaves outage probability. The work in [27] studied UAV as an aerial relay node to provide flexible aerial backhaul links when the terrestrial links suffer blockages. The work in [28] studied the optimal placement and orientation of mmWave enabled UAV as a base station so that the users have guaranteed LoS coverage. In [29], mmWaves enabled UAV was deployed to serve multiple UE over narrowband channels and the beamformer at UAV was designed such that each UE gets a dedicated data stream generated from a single RF chain. To overcome inter-beam interference, the authors in [30] designed hybrid precoder to maximize the rate of each UE by steering the beam towards its dominant multipath component (MPC) while maintaining the minimum rate constraint of the rest of the UEs. This approach is feasible when the number of UEs is not more than the number of RF chains. In a multi-UE scenario, with the number of UEs greater than the number of RF chains available at the UAV, the work in [31] designed the RF precoder so as to form sectors and served multiple UEs in each sector employing orthogonal frequency division multiple access (OFDMA). For this system, the authors studied the sum rate variation as a function of deployment height, the number of antennas, and backhaul link capacity. In [32], beam space precoding via discrete lens arrays was analyzed to reduce UAV hardware cost to support a multi-UE communication at mmWaves.

1.3.3 Beamforming for RIS-assisted Wideband mmWave System

Optimal design of RIS phase shifts is critical for maximizing the RIS performance gain. A large number of studies has been undertaken for single RIS-assisted and multi-RIS assisted mmWave communications in variety of scenarios like for terrestrial and aerial communication for narrowband as well as wideband channel, for coverage extension to a single or group of aerial or terrestrial UEs in indoor and outdoor communications, among others [33].

The multi-antenna backscatter devices can be used at mmWaves analogous to distributed RIS-assisted mmWave communication system, in which the multi-antenna backscatter devices are essentially the same as small sized RISs distributed over an area. Authors in [34] reported the use of multi-antenna tags for backscatter communication at mmWave range. A multi-antenna tag, when in idle mode, can be utilized to direct the incoming

signal from the access point (AP) to the legacy UE by optimizing the coefficients of the reflecting elements. It is noteworthy that a tag in this scenario just reflects the incoming signal; it does not modulate the incoming data in any way thereby creating a virtual path between the AP and UE. The authors in [35] suggested employing backscatter devices with MIMO systems at sub-6 GHz to create an artificial rich scattering environment. The results demonstrated enhanced system performance. Furthermore, similar to RIS, the reflection coefficient vector of multi-antenna tags can be optimized using CSI or angular information estimated during beam training [36].

The mmWave channel is sparse in angular domain due to low dispersion at higher frequencies. This property can be used to overcome high training costs of CSI based RIS beamforming. A discrete Fourier transform (DFT) codebook was used in [37] to estimate AoA to design RIS beamformer. In [38], RIS beamforming weights were designed based on the required angle of reflection to serve a UE. It was demonstrated that estimating the phase difference between two RIS elements is sufficient for designing the RIS beamformer. Moreover, a closed-form expression was derived for phase shift calculation using only three measurements. The authors in [39], proposed a modified MUSIC based estimator to estimate AoAs. Random beamforming was proposed in [40], which provides nearly acceptable long-run performance while requiring no CSI or AoA information.

1.4 Other Beamforming Elements Addressed in This Dissertation

1.4.1 Effect of Wideband mmWave Channel on Beamforming: Beam Squint

Hybrid beamforming allows spatial channel reuse with a small number of RF chains. However, in a wideband mmWave channel, the deployment of a large number of antenna elements to form narrow spatial beams leads to beam squint effect. Different antennas receive time-delayed copies of the same signal that give rise to beam squint in frequency domain wideband channels, i.e., different subcarriers (SCs) of the OFDM symbol see different AoA for the same path. Several works considered mmWave channel employing OFDM in designing hybrid beamforming precoder, but they did not consider beam squinting. In [41], RF and baseband precoders were designed for wideband channels us-

ing OFDM without factoring beam squint effect, i.e., it considered the array response to be frequency independent. Besides, the authors in [41] suggested allocating the same UE over the wideband channel by assuming a high correlation among subchannels due to the sparse nature of the mmWave channel. However, due to the beam-squinting effect of large antenna arrays and the surrounding environment, this is not always true [42]. Further, in a sub-array connected hybrid beamformer, it is not possible to design different steering weight vector of a RF precoder of a sub-array for each subcarrier. It is so because the signal fed to the antenna sub-array connected to a RF unit is a time domain signal that is sum of signals over all subcarriers. Hence, current studies on sub-array hybrid precoding schemes consider that the RF precoder is the same over the whole bandwidth [43].

Most of the hybrid precoder design optimization works focus on optimizing the baseband precoder to reduce inter-user interference and the number of RF chains as in [42] where interference beam squint on channel estimation was minimized by optimally designing the zero-forcing precoder. To compensate for the beam squint effect, the authors in [44, 45] proposed a fully-connected hybrid precoder design in which an RF precoder common to all subcarriers was constructed using angle-of-departure information, and the baseband precoder was optimized to compensate for the resulting beam squint effect. By considering the use of double phase shifter-based architectures, the authors in [46] proposed the design of frequency-dependent RF precoder/combiner strategies of a fully-connected hybrid precoder to control beam squint.

1.4.2 Medium Access Control (MAC) Layer Aspects of Beamforming

Besides the implication on the physical layer, the beamforming at mmWaves affects the MAC layer features as well, like initial access procedure, frame structure, and minimum transmission time interval (TTI), among others. According to the 3rd Generation Partnership Project (3GPP) New Radio (NR), the communication at mmWaves (also referred to as the FR2 range in 3GPP NR) is divided into two phases- beam training and data transmission phase. During the beam training phase, the cell area is divided into identical sectors of angular width equal to half-power beamwidth (HPBW) of the gNB beam, and the gNB performs initial access (IA) to determine the optimal gNB-UE beam pairs and to acquire additional UE parameters. The beam training occurs periodically to update channel and UE related information. Several approaches for IA, namely, exhaustive

Table 1.1: Existing MAC protocols for standalone mmWave systems

References	Frame flexibility	UE Scheduling	IA	Limitations
IEEE 802.11ad [54, 55]	fixed slot boundaries	single UE per RF beam; multiple UEs scheduled in spatial and time domain	hierarchical search	IA delay increase with narrow beams at gNB and UE; not suitable for cellular communications
3GPP NR [52, 56]	flexible uplink (UL) and DL resource allocation in a slot; fixed slot boundaries	not specified	exhaustive search	significant IA delay; bandwidth under-utilization during beam training phase
Frame structure [53]	flexible UL and DL resource allocation in a slot; fixed slot boundaries but flexible TTI	single UE per RF beam at a time	exhaustive search	variable TTI optimized only for short packets transmission; dedicated TDMA scheduling results in bandwidth under-utilization; assumes perfect beam alignment

search, hierarchical search, and context-information-based search, have been investigated in the literature [47–49]. The authors in [50] compared the latency of different combinations of directional beamforming and omnidirectional transmission IA protocols. A multi RF-chain sub-array technique is proposed in [51] for optimizing hierarchical codebook using beam widening. Since hierarchical search is better suited for point-to-point indoor communications, exhaustive brute search is the IA method suggested for 5G NR cellular scenarios [52]. The authors in [52] presented a survey on 3GPP NR MAC layer design at mmWave frequencies and studied the implications of its various parameters on IA and beam training. In [53], the authors proposed directional mmWave communications using a flexible frame structure based on variable TTI and proved that variable TTI offers various advantages, such as reduced latency and flexible scheduling. Table 1.1 summarizes the existing mmWave MAC layer protocols.

1.5 Research Gaps and Problem Identification

1. In a multi-user wideband mmWave communication system, dedicating a data stream generated from an RF unit to a single UE at a time over a wideband mmWave channel will lead to high scheduling complexities and poor system performances.

2. Besides, the increasing computational complexity, determining dominant channel eigenmodes for achieving perfect orthogonality among data streams via joint RF and baseband becomes more difficult as the user population grows.

3. Furthermore, the two-phase communication results in under-utilization of wide mmWave bandwidth as the beam training data is usually very small. Further, in 3GPP NR a slot is proposed to be composed of 14 OFDM symbols for enhanced mobile broadband (eMBB) applications at the mmWave range [57]. This fixed frame structure again results in resource under-utilization, specially in beam training phase, and fairness discrepancies among UEs in the mmWave systems.

4. Considering the above points, what should the best strategy be for providing service to $M \gg N_{RF}$ UEs over a wideband mmWave channel, while also taking into account a variety of factors such as spectral efficiency, energy efficiency, UE fairness, number of RF chains, computational complexity, beam squint, practical antenna array radiation pattern, and UE distribution type.

5. There has been little consideration given to selecting an RF precoder that accounts for beam squint. The few studies that looked into beam squint treated it as interference and designed RF and baseband precoders to mitigate its effects. However, we are of the view that rather than treating it as interference, beam squint can be utilized to improve the spectral efficiency of the system.

6. The power dissipation from numerous RF chains operating at mmWaves is a problem for energy-constrained UAVs in particular. This necessitates investigation into the optimal number of RF chains to be deployed at UAVs while taking into account practical antenna array radiation patterns and inter-beam interference and optimal UE grouping strategy to serve a large UE population.

7. In indoor environment, the idea of using multi-antenna tags, acting as distributed RIS, to serve obstructed UE over using a fixed RIS placed at a fixed position to serve the obstructed UE needs to be analyzed.

8. In an RIS-assisted system, the computational complexity of RIS beamforming with SVD increases exponentially with the channel matrix size. In addition, predicting the cascaded CSI is challenging and expensive due to the need to estimate every channel characteristic, including AoAs and propagation path gain products. Further, estimating AoA using MUSIC in AoA-based RIS beamforming is inefficient, especially for small devices that can have maximum 4 RF chains at mmWaves (as given in 3GPP NR specifications). Therefore, reduced complexity beamforming designs with RF chain constraints must be investigated.

In this dissertation, the above mentioned research gaps are addressed by investigating and proposing low complexity system frameworks to efficiently utilize the wideband mmWave channel, with Chapter 2 and Chapter 3 delving into the first four gaps and offering a sectored cell-framework as a solution to efficiently serve a large user population over the wideband mmWave channel. Chapter 4 analyzes the fourth research gap and presents a joint RF, baseband, and subcarrier allocation strategy that cleverly leverages beam squint. In Chapter 5, the sixth research gap is tackled, and a comprehensive optimization of the performance of a solar power UAV-assisted mmWave communication is presented. Finally, Chapter 6 addresses the last two research gaps by proposing a low-power and low-complexity alternative to enhance the performance of blocked users in indoor environments, utilizing passive RIS.

Thus, it is envisaged that the insights provided in this dissertation will aid in designing and improving the physical and MAC layer aspects of mmWave communication systems for future 5G+ networks.

1.6 Organization

Rest of the dissertation is organized in the following chapters:

Chapter 2 - Optimal Beamforming with Single Beam for Multi-user Wideband mmWave Communications: This chapter proposes a sectored-cell framework to serve multiple UEs with a single RF chain generating a steerable beam. Depending on user density and distribution, the optimal beamwidth for a sub-array hybrid precoder in sectored-cell framework is estimated for different scenarios to provide minimum rate support to all users across the wideband mmWave channel.

Chapter 3 -Multi-RF Beamforming for Multi-user Wideband mmWave Communications: In this chapter the analysis of sectored-cell framework is extended to the case of multiple concurrent beams generated using sub-array hybrid precoder. The analysis considers the inter-beam interference from sidelobes of concurrently active beams. The optimal beamwidth and optimal number of beams are estimated jointly for achieving maximum average long-run user rate of homogeneously distributed UEs. Additionally, a variable time frame structure is presented that conducts sector-wise IA using an analog beam, with simultaneous access to all users within a sector while improving fairness of

long-run user rates in non-homogeneously distributed UEs as well.

Chapter 4 - Joint Beamforming and Subcarrier Allocation with Beam Squint in Wideband mmWave Communication Systems: In wideband mmWave communications, the design of RF precoder and subcarrier allocation are intertwined. Based on this observation, this chapter proposes a sub-array hybrid precoder design wherein first RF precoder and subcarrier allocation are designed jointly leveraging beam squint and following that the baseband precoder is designed by transforming weighted sum-rate maximization into WMMSE optimization problem.

Chapter 5 - Sustainable UAV-assisted Multi-user Wideband mmWave Communications: This chapter studies the feasibility of using UAVs at mmWaves deployed at low altitudes to serve a user population higher than the number of RF chains available at the UAV. Optimal UE clustering method and optimal number of beams at UAV are estimated for energy sustainable UAV operation. Further, the battery capacity and solar panel are jointly optimized for the solar-powered UAV.

Chapter 6 - Reduced Complexity Beamforming for RIS-assisted Indoor mmWave Communications: This chapter discusses RIS-assisted mmWave communication for indoor mmWave communication using backscatter devices as distributed RIS. An AoA estimator using single RF chain at UE is proposed and then RIS (or backscatter devices) and UE beamformers are designed using estimated AoAs.

Chapter 7 - Concluding Remarks and Future Directions: This chapter outlines the key contributions of this dissertation and discusses potential future research directions.

Chapter 2

Optimal Beamforming with Single Beam for Multi-user Wideband mmWave Communications

2.1 Introduction

With increasing density of data-hungry devices per unit area, allocating single highly-directed beam per user in millimeter-wave communications is not practical. Therefore there is a need to model a system of lower complexity that can provide reliable and fair services while optimally serving multiple users over a single beam and optimally utilizing the available resources in mmWave multi-user cellular communications. As mentioned earlier, analog beamforming offers the most economical and reduced complexity designs; coupled with scheduling capabilities, it can provide satisfactory Quality-of-Service (QoS) to the UEs with high energy efficiency at the gNB. The limitation of analog beamforming is that only a single beam per RF chain can be generated, and spatial data stream multiplexing is not possible. To this end we observe that, recent technological advancements have made it possible to switch and steer the beam of phased antenna arrays within negligible time (order of a few nanoseconds), thus making it possible to schedule angularly-apart UEs in the time domain using a single narrow beam.

For an analog beam, the authors in [2] surveyed several codebook designs and optimization techniques to find optimum beamwidth with reduced protocol overhead in a two-level exhaustive beam search procedure and also to reduce transmitter-receiver beam misalignment. However, these optimization problems target only indoor communication

where single UE is served per RF chain, which is feasible only for small indoor population [58]. The performance of such schemes degrades in outdoor mmWave communication with high user density.

Another notable point is that most of the mmWave research focus on improving data rates and overcoming blockage effects through enhanced SNR (or radiated power density) by increasing transmit beamforming gain. For example, the approach in [59] estimates the optimal beamwidth that provides increased signal strength at the UE to overcome blockage effects. But increased power density causes elevated radiation hazard in the environment. The Federal Communications Commission (FCC) guidelines have defined limits on peak equivalent isotropically radiated power (EIRP) for communication over mmWaves to ensure health safety [60]. Accordingly, we are motivated to study the mmWave system performance while maintaining the same radiation level in the cell.

In this chapter, we consider a 2-dimensional (2-D) scenario where a single analog beam serves a cell in a time-multiplexed fashion while keeping the EIRP level same in the cell, invariant of the antenna gain. The cell is sectorized into S similar disjoint sectors based on HPBW Θ of the analog beam. S decreases with increasing Θ, and vice versa. We aim to find optimal sectorization scheme S^* instead of optimal beamwidth Θ^* because of mathematical convenience. The beam sweeps the area in either clockwise or counterclockwise direction. As Θ decreases, the total transmit power required to cover the same cell range per sector decreases, and the channel spatial reuse factor of the cell increases, whereas the time delay between the next schedule of each sector increases. Unlike in [19], the complexity of UE grouping algorithm in this model is independent of UE population. In the proposed scheme, multiple UEs are served simultaneously using OFDM in a single time slot per RF chain. Depending on UE density and distribution, a smaller value of Θ may result in certain sectors having no UEs at all. In that case, the total cell sweep time can be reduced by not scheduling those sectors, thereby saving transmit energy. We ask the following question: What should be the optimum width of transmitted signal beam to cater to a specific UE distribution while jointly maximizing the average long-run UE data rate and energy efficiency of the gNB?

To the best of our knowledge, this mmWave system behaviour has not been studied in the literature. Moreover, with huge bandwidth availability in mmWaves, employing time division multiple access scheduling to angularly spreaded UEs with large fixed time slots (e.g., 1 ms) may not be efficient [53]. We note that, in FCC guidelines, 5G systems can have variable-duration transmission units according to services and applications context.

Thus, it is also worth studying the effect of variable scheduling based on different factors, such as UE distribution and channel conditions, on system performance.

Additionally, UE localization using global positioning system (GPS) in conventional cellular communication has an error range in meters. Such high error is not tolerable in mmWaves employing directional beams. In mmWaves there are various localization methods, such as ray tracing, exhaustive beam searching, and RF-based ranging methods. The ray tracing method requires detailed surrounding and multipath components information, whereas exhaustive searching entails a large beam training data. The complexities of both these methods are proportional to the number of antenna elements at the gNB and the UE. Two most popular localization methods in mmWaves are AoA and time-of-arrival (ToA) [61]. Localization accuracy in mmWaves outdoor scenarios, with large antenna array at the gNB, single antenna at the UE, and line-of-sight paths using AoA and ToA methods, were studied in [62, 63]. It was shown in [63] that use of extended Kalman filtering can achieve sub-meter accuracy even for mobile devices. In [62] it was noted that, for static UEs with transmit beamforming, the position estimation error is inversely proportional to antenna array size. Along this line, with analog beamforming at gNB, keeping EIRP constant irrespective of beamwidth, the effect of localization might have some role in deciding the optimal sector beamwidth in downlink mmWave communications. This is also an aspect of investigation in this chapter.

2.1.1 Contribution

Key contributions of this chapter are as follows:

a) A prototype employing a single analog beam to cater to the outdoor UE population in wideband mmWave communications using a sectored-cell with time multiplexing approach is proposed ans analyzed. A narrow beam of optimally-chosen beamwidth, generated from an RF chain, serves multiple UEs during the beam sojourn time using the OFDMA scheme, as opposed to single UE per beam in the existing literature. The effect of channel frequency selectivity along with the minimum QoS requirements of each UE is considered in performance evaluation. As an extension, a comparison between a single beam system and multiple beams system is also studied; it is noted that while transmission over multiple analog beams may achieve a higher average long-run UE rate with respect to the single analog beam system, it is always at the cost of reduced gNB energy efficiency.

b) An optimization problem is formulated to find the optimum sectorization scheme for the single analog beam system that maximizes the average long-run UE rate (average of all UEs' rates with each UE rate averaged over cell sweep time) and gNB energy efficiency. It is observed that a Pareto optimal trade-off exists between average long-run UE rate and gNB energy efficiency.

c) A method of reduced complexity is proposed to estimate optimal sectorization scheme for average long-run UE rate maximization for a given UE population.

d) For catering to non-homogeneous UE distribution using single beam, a variable-time scheduling per sector is formulated. The studies reveal that, for non-uniformly distributed UEs, variable time scheduling scheme provides considerably improved performance in terms of maximum achievable average long-run UE rate as well as gNB energy efficiency.

e) Lower bounds on UE position estimation error is derived for analog beamforming using a practical antenna radiation pattern of the array. The impact of position error on the optimal beamwidth selection is also investigated.

2.1.2 Chapter Organization

The remaining chapter is organized as follows. System model is presented in Section 2.2. Sector sum rate maximization and optimum sector beamwidth optimization problem along with analysis are presented in Section 2.3. Simulation results are presented in Section 2.4, and the chapter is summarized in Section 2.5.

2.2 System Model

Consider a 2-D multi-user outdoor cellular scenario as shown in Fig. 2.1. Let there be a gNB with one RF unit and M UEs $\{\mathrm{x}_1, \mathrm{x}_2, ..., \mathrm{x}_M\}$, distributed over a cell. Each UE x_i has a distribution according to some probability function $\mathcal{Q}(\cdot)$ in $\mathbb{R}^2$. Let $\mathcal{S}$ be a set; its elements denote the total number of sectors S in a cell when it is sectorized into equal and identical regions of angular width Θ, i.e, $\mathcal{S} = \{S | S = \lceil 2\pi/\Theta \rceil, \Theta_{min} \leq \Theta \leq \Theta_{max}\}$. Let s denote the index of a particular sector, i.e., $s = \{1, \ldots, S\}$ when the total number of sectors is $S \in \mathcal{S}$. Then, the probability of finding a UE in the sth sector of a given sectorization $S \in \mathcal{S}$ scheme given by $\mathcal{Q}(s)$ [64]. In case of uniform UE distribution, the

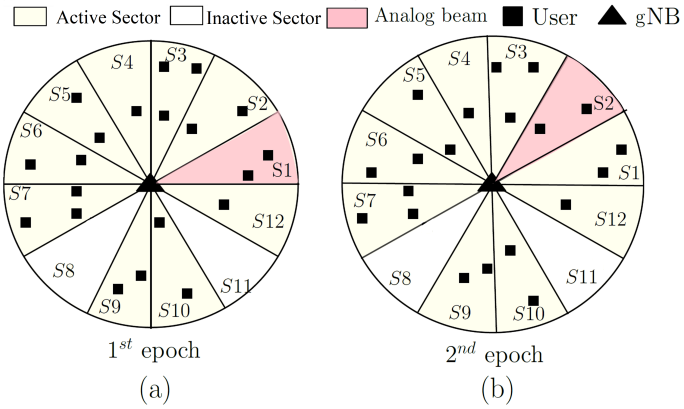

Figure 2.1: Pictorial representation of a 2-D single cell with 20 independent and uniformly distributed UEs, served by a single analog beam in two consecutive epochs when the cell sectorization scheme is $S = 12$ sectors. Here, sector $S8$ and $S11$ do not have any UEs.

probability of finding a UE in a sector is $\mathcal{Q}(s) = 1/S$ for $s = 1, \ldots, S$. To model non-uniform UE distribution a cell is divided into Z identically wide zones with the probability of distribution of each UE in the zth zone being p_z, such that $\sum_{z=1}^{Z} p_z = 1$.

2.2.1 mmWave Channel Model

In this chapter UEs are considered to be equipped with a single omnidirectional antenna, i.e., $N_r = 1$ and gNB has a ULA consisting of N_t identical isotropic antenna elements connected to an RF chain. The maximum ULA gain is at steering angle $\phi = 0^o$ and is equal to $G_t = N_t G_0$, where G_0 is single antenna element gain. The beam gain G_t is assumed constant and equal to maximum gain within the sector and zero outside [58]. The HPBW of a beam is $\Theta \approx 2/N$ radians, that divides the cell into $S = \lceil 2\pi/\Theta \rceil$ similar disjoint sectors. Let P_{tot} be the total transmit power available at the gNB. EIRP $(= P_{tot} G_0)$ of the BS is kept constant so that the cell coverage is static irrespective of the beam directivity. Therefore, to maintain the same SNR at UE at a distance d, the transmit power requirement in a sector of Θ HPBW is calculated as:

$$P_t = \frac{\text{EIRP}}{G_t} = \frac{P_{tot}}{N_t}. \tag{2.1}$$

At mmWave frequencies there exists either a LoS link or NLoS link between UE and gNB due to large difference in attenuation of first order and higher order signals. The probability of a link being in LoS for kth UE at distance d_k from gNB is expressed as

$$\Pr(d_k) = \min(d_1/d_k, 1)(1 - e^{-d_k/d_2}) + e^{-d_k/d_2}, \tag{2.2}$$

where $d_1 = 18$ and $d_2 = 36$. Additionally, the path loss for LoS and NLoS link are obtained as [65]

$$\begin{aligned} \text{PL}_{LOS}(d_k) &= 61.4 + 20\log_{10}(d_k) + \mathcal{N}(0, 33.64) \text{ [dB]} \\ \text{PL}_{NLOS}(d_k) &= 72.0 + 29.2\log_{10}(d_k) + \mathcal{N}(0, 75.69) \text{ [dB]}. \end{aligned} \tag{2.3}$$

Therefore, for the kth UE, at a distance d_k from gNB the pathloss PL_k is expressed as

$$\text{PL}_k = \begin{cases} \text{Pr}(d_k)10^{\text{PL}_{LOS}(d_k)/10}, & \text{LOS} \\ (1 - \text{Pr}(d_k))10^{\text{PL}_{NLOS}(d_k)/10}, & \text{NLOS}. \end{cases} \tag{2.4}$$

Let $\gamma_{n,k}$ be a parameter that denotes the combined channel state and location information of the kth UE, at a distance d_k, over the nth subcarrier, which is expressed as:

$$\gamma_{n,k} = \frac{G_t G_r |h_{n,k}|^2 \text{PL}_k}{N_0 B / N_c}. \tag{2.5}$$

Here, N_c is the total number of subcarriers from G_t and G_r are respectively transmitter and receiver antenna gain, N_0 is the noise power spectral density, B is the total channel bandwidth, $h_{n,k}$ is small scale channel parameters of kth UE over nth subcarrier that is Rician distributed for LoS path and Rayleigh distributed for NLoS path.

Thus, the data rate $r_{n,k}$ for the kth UE over the nth subcarrier is

$$r_{n,k} = \frac{B}{N_c}\log_2(1 + P_{n,k}\gamma_{n,k}), \tag{2.6}$$

where $P_{n,k}$ is the power of kth UE over nth subcarrier. In order to perform water-filling over the subcarriers, perfect channel knowledge of all UEs is considered at the gNB.

2.3 Problem Formulation and Analysis

This section describes the problem formulation for optimal sectorization scheme S^* (or optimal sector beamwidth Θ^*) in a cell under different scenarios. Firstly, we estimate S^* that maximizes the average long-run UE rate and gNB energy efficiency, assuming perfect UE location knowledge at the gNB. Next, when the gNB has only an estimated position of the UEs using analog beamforming, we derive a lower bound on localization error and incorporate it to find S^*.

2.3.1 Optimal Sectorization Scheme with Perfect UE Location Information

Here we present the steps involved in estimating S^* for the model described in Section 2.2. For a sectorization scheme, $S \in \mathcal{S}$ each of the sectors has a full channel for its use. Hence, the sum rate of a sector during its schedule time, i.e., instantaneous sum rate, can be maximized independently. Consequently, the problem of finding optimal beamwidth can be divided into two parts. First, for a given value of S, we find the instantaneous sum rate for all of the active sectors (sectors with at least one UE) independently. After that, using an exhaustive search over all sectorization schemes $S \in \mathcal{S}$, we estimate S^* that maximizes the average long-run UE rate and gNB energy efficiency. Further, we provide a reduced complexity method that estimates a sub-optimal sectorization scheme $\hat{S}^*$ for a given UE population without exhaustive search.

2.3.1.1 Instantaneous Sum Rate Maximization per Sector

Instantaneous sum rate maximization problem using OFDM in sth sector of a sectorization scheme $S \in \mathcal{S}$, with minimum instantaneous rate constraint R_0 per UE (except for the UEs in outage) and maximum available transmit power P_t (given by (2.1)), is formulated as:

$$
\begin{aligned}
(\mathcal{P}1): \max_{\pi_{n,k}, P_{n,k}} \quad & \sum_{k=1}^{K_s} \sum_{n=1}^{N_c} r_{n,k} \pi_{n,k} \\
\text{s.t.} \quad & C11: \sum_{k=1}^{K_s} \pi_{n,k} \leq 1, \ \forall n; \ C12: \sum_{n=1}^{N_c} r_{n,k} \pi_{n,k} \geq R_0, \ \forall k \\
& C13: \pi_{n,k} \in (0,1), \ \forall n,k; \ C14: \sum_{k=1}^{K_s} \sum_{n=1}^{N_c} P_{n,k} \leq P_t; \ C15: P_{n,k} \geq 0, \ \forall n,k
\end{aligned}
\tag{2.7}
$$

where the UE$-$subcarrier association variable $\pi_{n,k} = 1$ if kth UE assigned nth subcarrier; 0 otherwise. The resources are allocated only to $K_s \subseteq K_s'$ UEs that are not in complete outage. Here, K_s' is the set of UEs falling in the sth sector such that $\bigcup_{s \in S} K_s' = M$. We define kth UE to be in outage if $\max\limits_{n \in \mathcal{N}_c} \{\gamma_{n,k}\} < \gamma_{th}$. Here, γ_{th} is the threshold channel state value, $k = 1, 2, \cdots, K_s$.

$\mathcal{P}1$ jointly allocates subcarriers and power to maximize the achievable sum rate and is a mixed-integer non-convex programming problem. Such problems are Non-deterministic

Polynomial time (NP)-hard and not computationally efficient. The Lagrangian of $\mathcal{P}1$ is formulated as:

$$\begin{aligned}\mathcal{L}(\pi_{n,k}, P_{n,k}, \bar{\eta}_k, \bar{\lambda}) &= \sum_{k=1}^{K_s}\sum_{n=1}^{N_c} r_{n,k}\pi_{n,k} + \sum_{k=1}^{K_s}\bar{\eta}_k\left(\sum_{n=1}^{N_c} r_{n,k}\pi_{n,k} - R_0\right) - \bar{\lambda}\left(\sum_{k=1}^{K_s}\sum_{n=1}^{N_c} P_{n,k} - P_t\right)\\ &= \sum_{n=1}^{N_c}\sum_{k=1}^{K_s}\left(r_{n,k}\pi_{n,k}\left(1+\bar{\eta}_k\right) - \bar{\lambda}P_{n,k}\right) - \sum_{k=1}^{K_s}\bar{\eta}_k R_0 + \bar{\lambda}P_t\\ &= \sum_{n=1}^{N_c}\mathcal{L}_n\left(\pi_{n,k}, P_{n,k}, \bar{\eta}_k, \bar{\lambda}\right) - \sum_{k=1}^{K_s}\bar{\eta}_k R_0 + \bar{\lambda}P_t\end{aligned} \tag{2.8}$$

where $\bar{\lambda}$ is the Lagrange multiplier for power constraint $C14$ and $\bar{\eta}_k\ \forall k$ are the Lagrange multipliers for rate constraint $C12$. In order not to violate complementary slackness condition $\bar{\lambda} \geq 0, \bar{\eta}_k \geq 0\ \forall k$. The binary variable constraints $C11, C13$, and positive power constraint $C15$ are not included into the Lagrangian formulation to circumvent unnecessary complexity but are considered at later stage. This method will not alter the solution. Further, the optimization problem satisfies the time-sharing condition [66]. Hence, the duality gap is zero, i.e., the dual function solution is same as the primal function solution. The Lagrangian dual function is:

$$\begin{aligned} g(\bar{\eta}_k, \bar{\lambda}) = \max_{\pi_{n,k}, P_{n,k}} \quad & \mathcal{L}(\pi_{n,k}, P_{n,k}, \bar{\eta}_k, \bar{\lambda}) \\ \text{s.t.}: \quad & C11, C13, C15. \end{aligned} \tag{2.9}$$

The above equation can be decomposed into the following N_c independent problems as:

$$\begin{aligned} g'(\bar{\eta}_k, \bar{\lambda}) = \max_{P_{n,k}} \quad & \mathcal{L}_n(\pi_{n,k}, P_{n,k}, \bar{\eta}_k, \bar{\lambda}) \\ \text{s.t.}: \quad & C15. \end{aligned} \tag{2.10}$$

Assuming kth UE is active on nth subcarrier, (2.10) reduces to

$$\begin{aligned} g'(\bar{\eta}_k, \bar{\lambda}) = \max_{P_{n,k}} \quad & \pi_{n,k}\frac{B(1+\bar{\eta}_k)}{N_c}\log_2(1+P_{n,k}\gamma_{n,k}) - \bar{\lambda}P_{n,k} \\ \text{s.t.}: \quad & C15. \end{aligned} \tag{2.11}$$

(2.11) is concave in $P_{n,k}$. Hence by Karush-Kuhn-Tucker (KKT) condition the solution to optimal power allocation $P'_{n,k}$ is:

$$\frac{\partial\mathcal{L}_n(\pi_{n,k}, P_{n,k}, \bar{\eta}_k, \bar{\lambda})}{\partial P_{n,k}} = \frac{(B/N_c)\pi_{n,k}\gamma_{n,k}(1+\bar{\eta}_k)}{(\ln 2)(1+P_{n,k}\gamma_{n,k})} - \bar{\lambda} = 0. \tag{2.12}$$

Incorporating the constraint $C15$, from (2.12) we have

$$P'_{n,k} = \left[\frac{(B/N_c)\pi_{n,k}(1+\bar{\eta}_k^*)}{(\ln 2)\bar{\lambda}^*} - \frac{1}{\gamma_{n,k}} \right]^+ \tag{2.13}$$

where $[x]^+ = \max(x, 0)$, $\bar{\lambda}^*$ is the optimal dual variable corresponding to power constraint, and $\bar{\eta}_k^*$ is the optimal dual variable corresponding to minimum rate constraint of the kth UE.

The Lagrangian variables are updated using sub-gradient based approach [67] as follows:

$$\begin{aligned} \bar{\lambda}^{(i+1)} &= \left[\bar{\lambda}^{(i)} - \bar{\epsilon}^{(i)} \left(P_t - \sum_k \sum_n P_{n,k}^* \right) \right]^+ \\ \bar{\eta}_k^{(i+1)} &= \left[\bar{\eta}_k^{(i)} - \bar{\epsilon}^{(i)} \left(\sum_n \pi_{n,k}^* r_{n,k} - R_0 \right) \right]^+ \forall k \end{aligned} \tag{2.14}$$

where $\bar{\epsilon}^{(i)}$ is the step size at ith iteration and is chosen according to the constant step size policy, independent of iteration number. Update of $\bar{\eta}_k$ ensures the minimum rate constraint. Finally, the UE$-$subcarrier combination is selected that offers the maximum sum rate while satisfying minimum rate constraint of all the UEs.

Proposed sub-optimal algorithm: The above exhaustive search method requires the execution of water-filling algorithm for at least $K_s^{N_c}$ times. To address this, we convert the optimization problem $\mathcal{P}1$ into a sub-optimal problem of lower complexity, leveraging the fact that sum rate maximization incurs a negligible penalty when only channel adaptive subcarrier allocation is performed [68]. The steps involved in sub-optimum optimization approach are:

(i) To reduce complexity at a starting resource allocation step, we divide the total transmit power P_t equally among all the subcarriers, i.e., if $\pi_{n,k} = 1$ then $P_{n,k} = P_t/N_c$.

(ii) Initially we allocate each subcarrier to a UE with the best channel condition without considering the rate constraints $C12$ [68]. Hence, the initial optimal UE–subcarrier association to the nth subcarrier is found as $k'(n) = \underset{k}{\text{argmax}}\, r_{n,k}$.

(iii) Subcarrier allocation from step (ii) does not satisfy the constraint $C12$. Therefore, we carry out the subcarrier allocation on a user-by-user basis for all UEs to satisfy the minimum rate constraints (unless they are in complete outage) using cost function approach [68]:

$$c_{n,k} = \frac{(r_{n,k'(n)} - r_{n,k})}{r_{n,k}}$$

where $k'(n)$ is the user that is initially assigned to nth subcarrier from step (ii). The cost function is proportional to the reduction in overall sum rate. For kth UE that does not satisfy the constraint $C12$, the $\tilde{n}$th subcarrier assigned to meet its minimum rate requirements is found as $\tilde{n} = \underset{n}{\text{argmin}}\, c_{n,k}$. Further, during subcarrier reallocation the $\tilde{n}$th subcarrier that was initially associated to $k'(\tilde{n})$th UE should not be reallocated to another UE if this reallocation violates the minimum rate constraint of the original UE, i.e., $\tilde{n}$th subcarrier is not allocated to kth UE if $R(k') - r_{\tilde{n},k'} < R_0$, where $R(k') = \sum_{n=1}^{N_c} \pi_{n,k'} r_{n,k'}$.

Remark 2.1. *$\mathcal{P}1$ has a feasible solution if $K_s \leq N_c$ and the value of R_0 is appropriately chosen. In case $K_s > N_c$ the subcarriers are assigned to only N_c UEs having best channel conditions among K_s UEs, with minimum rate requirement fulfilment of only N_c UEs while the remaining $K_s - N_c$ UEs will be considered in outage in that cycle of sector sweep.*

Remark 2.2. *When the value of K_s is very low, the subcarrier allocation algorithm does not utilize the channel capacity to its maximum, as there may be some subcarriers that are not assigned to any UE due to deep fade. When the K_s increases, the probability of a subcarrier being in deep fade simultaneously for all the UEs decreases, thereby increasing overall sum rate (channel utilization). However, when the value of K_s is sufficiently high, assigning a subcarrier to a UE whose rate constraint was not satisfied earlier (from step (ii)), instead of the UE with best channel gain over the subcarrier, leads to a decrease in overall sum rate.*

(iv) During UE–subcarrier assignment in steps (ii) and (iii), equal power allocation per subcarrier is considered, as given in step (i). Hence, in order not to violate minimum rate constraints of UEs while executing water-filling, each UE is offered a share of total transmit power proportional to the number subcarriers assigned to it. Therefore, the problem of power assignment to UEs further reduces to solving power allocation to each UE over its set of assigned subcarriers, independent of other UEs. Hence, the power assignment optimization of kth UE over its assigned set of subcarriers Ω_k (step (iii)) is expressed as:

$$\begin{aligned} (\mathcal{P}2) : \max_{P_{n,k}} \quad & \sum_{n \in \Omega_k} r_{n,k} \\ \text{s.t.} \quad & C21 : \sum_{n \in \Omega_k} P_{n,k} \leq \frac{|\Omega_k| P_t}{N_c};\ C22 : P_{n,k} \geq 0, \forall n \in \Omega_k. \end{aligned} \tag{2.15}$$

The Lagrangian of $\mathcal{P}2$ is formulated as:

$$\mathcal{L}_k(\{P_{n,k}\}_{\forall n\in\Omega_k},\lambda_k) = \sum_{n\in\Omega_k} r_{n,k} - \lambda_k \sum_{n\in\Omega_k}\left(P_{n,k} - \frac{|\Omega_k|P_t}{N_c}\right) \tag{2.16}$$

where λ_k is the dual variable associated with maximum power constraint $C21$.

Since (2.16) is concave in $P_{n,k}$, from KKT conditions it follows:

$$\begin{aligned}\frac{\partial\mathcal{L}_k(\{P_{n,k}\}_{\forall n\in\Omega_k},\lambda_k)}{\partial P_{n,k}} &= \frac{(B/N_c)\pi_{n,k}\gamma_{n,k}}{\ln 2(1+P_{n,k}\gamma_{n,k})} - \lambda_k = 0\\ P^*_{n,k} &= \left[\frac{(B/N_c)\pi_{n,k}}{\ln 2\lambda^*_k} - \frac{1}{\gamma_{n,k}}\right]^+\end{aligned} \tag{2.17}$$

where λ^*_k is the optimal dual variable corresponding to power constraint of the kth UE and is found using sub-gradient method with sufficiently small constant step size $\hat{\epsilon}$, given as:

$$\lambda_k^{(i+1)} = \left[\lambda_k^{(i)} - \hat{\epsilon}^{(i)}\left(\frac{|\Omega_k|P_t}{N_c} - \sum_k\sum_n P^*_{n,k}\right)\right]^+. \tag{2.18}$$

Steps (i) to (iv) solve the original constrained problem in a sub-optimum way. The optimal solution of $\mathcal{P}1$ is an upper bound on the sub-optimum solution obtained using $\mathcal{P}2$. Both the solutions show similar behaviour on varying parameters, which we have verified via simulation in Section 2.4. Thus, to calculate the instantaneous rate of all the UEs in the active sectors sub-optimum approach is used that significantly reduces computation complexity.

Remark 2.3. *In this chapter, S^* is estimated by comparing system performance over all sectorization schemes $S \in \mathcal{S}$, which is a relative analysis. Hence, the qualitative nature of the solution of $\mathcal{P}1$ is of more interest than its quantitative nature. Therefore, the instantaneous rate allocation can be done with other resource allocation techniques as well.*

2.3.1.2 Sector Beamwidth Optimization

We use the average long-run UE rate to evaluate the QoS of the system from UE's perspective. Let t_s be the time spent by the beam in sth sector and $R_{k,s}$ be the instantaneous rate of kth UE in the sth sector during beam sojourn time t_s of the sectorization scheme

$S \in \mathcal{S}$. Also, let $\mathcal{S}_I(S) = \{s|K_s \neq 0, \forall s \in \{1, \ldots, S\}\}$ denote the support of s of a particular $S \in \mathcal{S}$. Then long-run data rate $\hat{R}_{k,s}$ of kth UE in sth sector is:

$$\hat{R}_{k,s} = \frac{R_{k,s}t_s}{\sum_{s\in\mathcal{S}_I(S)} t_s}. \tag{2.19}$$

Hence, the average of long-run UE rate in sectorization scheme S is:

$$\bar{R}(S) = \frac{1}{M} \sum_{s\in\mathcal{S}_I(S)} \sum_{k=1}^{K_s} \hat{R}_{k,s}. \tag{2.20}$$

Solving for the optimal resource allocation for sum rate maximization with rate constraints result in non-uniform rate distribution among the UEs. Therefore, we use Jain's fairness index [69] to characterize fairness of the long-run UE rate distribution. In general it is defined as:

$$J(S) = \frac{1}{M} \frac{(\sum_{j=1}^{j=M} \hat{R}_j)^2}{\sum_{j=1}^{j=M} (\hat{R}_j)^2} \tag{2.21}$$

where $\hat{R}_j$ is the long-run UE rate of jth UE. Another parameter of interest is the energy efficiency at gNB achieved by a particular sectorization scheme $S \in \mathcal{S}$. Energy efficiency is defined as the ratio of total number of bits transmitted to the total energy consumed in transmitting those bits. For a sectorization scheme S, it is given as:

$$\bar{E}(S) = \frac{\sum_{s\in\mathcal{S}_I(S)} \sum_{k=1}^{K_s} (R_{k,s}t_s)}{\sum_{s\in\mathcal{S}_I(S)} (\sum_{n=1}^{N_c} \sum_{k=1}^{K_s} P_{n,k}t_s)}. \tag{2.22}$$

To find S^* that maximizes $\bar{R}$ and $\bar{E}$, the multi-objective optimization problem (MOP) is expressed as:

$$(\mathcal{P}3) \quad \text{MOP}: \quad \underset{S\in\mathcal{S}}{\text{argmax}} [\bar{R}(S) \;\; \bar{E}(S)]. \tag{2.23}$$

Both average long-run UE rate $\bar{R}$ and gNB energy efficiency $\bar{E}$ are functions of S. It is possible that the two objectives are of conflicting nature, i.e., in choosing the optimal sectorization scheme S^*, there exists a trade-off between $\bar{E}$ and $\bar{R}$. In such a situation the solution to MOP problem consists of a complete set of dominated solutions, known as the Pareto Set.

Definition: A decision vector $S^* \in \mathcal{S}$ is Pareto-optimal if there exists no other feasible decision vector $\tilde{S} \in \mathcal{S}$ that dominates S^*, i.e., S^* is strictly better than $\tilde{S}$ in all objectives.

In order to find Pareto-optimal points, we use single-objective optimization problem (SOP) approach [70] for a given $\bar{R}$ (i.e., fixing the value of one of the objectives) as shown

below:

$$(\mathcal{P}4) \quad \text{SOP}(\bar{R}) : \underset{S \in \mathcal{S}}{\text{argmax}}\ \bar{E}(S). \tag{2.24}$$

For a given value of $\bar{R}$, let S^* be an optimal solution of $\mathcal{P}4$, with corresponding objective value $\bar{E}^*$. Then S^* is a Pareto-optimal solution to MOP. This process is repeated for different values of $\bar{R}$, and thus a set of Pareto optimal $(\bar{R}, \bar{E}^*)$ combinations is achieved.

Proposed reduced-complexity method: The method discussed so far performs exhaustive search over all $S \in \mathcal{S}$ in order to determine the optimal number of sectors S^* that maximizes average long-run UE rate for a given UE population. This procedure needs to be re-executed if the UE population changes. To reduce online computation requirements, we propose a reduced-complexity method for estimating sub-optimal $\hat{S}^*$ that achieves maximum average long-run UE rate without having to solve the complete optimization problem when the UE population changes.

In fixed time scheduling, let $t_1 = t_2 = \cdots = t_S = T$, then total cell sweep time is $\sum_{s \in \mathcal{S}_I(S)} t_s = T \times |\mathcal{S}_I(S)|$. From (2.19) and (2.20), average long-run UE rate is:

$$\bar{R}(S) = \frac{\sum_{s \in \mathcal{S}_I(S)} \sum_{k=1}^{K_s} R_{k,s} t_s}{M \sum_{s \in \mathcal{S}_I(S)} t_s} = \frac{\sum_{s \in \mathcal{S}_I(S)} \sum_{k=1}^{K_s} R_{k,s} t_s}{M \times T \times |\mathcal{S}_I(S)|}. \tag{2.25}$$

Since it is assumed that a given value of $S \in \mathcal{S}$ partitions the cell into identical disjoint sectors, the resource allocation of a sector is independent of other. Another notable point is that the individual sector's sum rate is a function of the number of UEs K_s present in sth sector (see *Remark* 2.2) and of sectorization scheme S (because of variation of path loss with Θ).

Let for a sectorization scheme $S \in \mathcal{S}$ and M uniformly distributed UEs, each active sector has $K_s \approx M/|\mathcal{S}_I(S)|$ UEs with corresponding sector sum rate R_{sum} during T. Then, (2.25) can be approximated as:

$$\bar{R}(S) \approx \frac{|\mathcal{S}_I(S)| \times R_{sum} \times T}{M \times T \times |\mathcal{S}_I(S)|} = \frac{R_{sum}}{M}. \tag{2.26}$$

Hence, maximization of the average long-run UE rate is essentially to maximize the sum rate of each sector for a given UE population. To maximize R_{sum} we need to solve the optimization problem $\mathcal{P}1$ for $1 \leq K_s \leq N_c$. But $\mathcal{P}1$ is an NP-hard problem. Therefore, we solve it in a sub-optimum way as described in Section 2.3.1.1. Thereafter, to find sub-optimal sectorization scheme $\hat{S}^*$ with reduced complexity method, we use a dictionary based approach. In this, a *dictionary* containing the sector sum rates corresponding to all

combinations of sectorization schemes and the number of UEs in a sector is pre-calculated at gNB using the statistical channel and UE distribution. The dictionary is then used to directly find $\hat{S}^*$ for any given UE population.

The maximum number of UEs supported per sector is equal to the number of subcarriers. Let the dictionary $\mathcal{R}_{\mathbf{sum}}$ be a matrix of sector sum rates with dimensions equal to $|\mathcal{S}| \times N_c$. Hence, $\mathcal{R}_{\mathbf{sum}}(S, K_s)$ corresponds to the sum rate when the sectorization scheme is S and number of UEs in a sector is K_s. Once $\mathcal{R}_{\mathbf{sum}}$ is known, $\hat{S}^*$ for M uniformly distributed UEs is found as:

$$\hat{S}^* = \underset{S \in \mathcal{S}}{\operatorname{argmax}}\ \mathcal{R}_{\mathbf{sum}} \left(S, \left\lceil \frac{M}{S} \right\rceil \right). \tag{2.27}$$

Similarly, maximization of average long-run UE rate with non-uniformly distributed UEs is synonymous to maximizing throughput of the highest populated zone which is the driving factor of the overall cell throughput. So, in case of M non-uniformly distributed UEs $\hat{S}^*$ is found as:

$$\hat{S}^* = \underset{S \in \mathcal{S}}{\operatorname{argmax}}\ \mathcal{R}_{\mathbf{sum}} \left(S, \left\lceil \frac{M p^{max}}{S/Z} \right\rceil \right) \tag{2.28}$$

where Z is the total number of zones in a cell, and $p^{max} = \max_z \{p_z\}$ where $z = 1, 2 \ldots, Z$.

2.3.1.3 Variable Time Scheduling

To account for the possibility of non-uniform UE distribution in a cell we study two scheduling schemes, namely, fixed time scheduling and variable time scheduling. In fixed time scheduling, $t_s = T$ if $K_s \neq 0$; 0 otherwise. In variable time scheduling, the schedule time t_s of each active sector is a function of the number of UEs in the that sector, i.e., $t_s \propto {K_s}^{\alpha}$, where α is the shaping parameter that governs the nature of scheduling time. $\alpha = 0$ corresponds to a fixed time scheduling scheme. Besides, we observe that as Θ decreases the number of UEs located within a sector decreases. Also, the spatial frequency reuse factor of the cell is improved. As a result, UEs benefit from spatial multiplexing gain which provides improved fairness among UEs.

Lemma 1: For a fixed α and $K_s \leq N_c$, Jain's fairness index J is an increasing function of S, when resource allocation is performed using sum rate maximization approach.

Proof: Given in the Appendix A.

We consider fairness index of fixed time scheduling scheme $J_{\alpha_0}(S^*)$ at $\alpha = \alpha_0 = 0$ as a benchmark for the variable time scheduling. Here, S^* is the optimal sectorization scheme such that $S^* = \underset{S \in \mathcal{S}}{\operatorname{argmax}}\ \bar{R}_{\alpha_0}(S)$. Thus, the benchmark of the maximum average

Algorithm 2.1 α_R search algorithm

Input: $R_{k,s}\ \forall S \in \mathcal{S}$
Output: α_R
Initialize: $j = 1, \alpha_R = \alpha_0 = 0, \hat{\delta} = 0.1$
Find: $S^* = \underset{S\in\mathcal{S}}{\text{argmax}}\ \bar{R}_{\alpha_0}(S), \bar{R}_{opt} \leftarrow \bar{R}_{\alpha_0}(S^*)$
while $\alpha_j = \alpha_{j-1} + \hat{\delta}$ **do**
    Compute: $\bar{R}_{\alpha_j}(S)$, $J_{\alpha_j}(S), \bar{E}_{\alpha_j}(S)\ \forall S$
    if $J_{\alpha_j}(S = 360) < J_{\alpha_0}(S^*)$ **then**
        break; (*Stopping condition*)
    end if
    for $i = S^* : 360$ **do**
        if $J_{\alpha_j}(i) \geq J_{\alpha_0}(S^*)$ & $\bar{R}_{\alpha_j}(i) > \bar{R}_{opt}$ & $\bar{E}_{\alpha_j}(i) \geq \bar{E}_{\alpha_0}(S^*)$ **then**
            $\alpha_R = \alpha_j, \bar{R}_{opt} = \bar{R}_{\alpha_j}(i), S'^* = i$
        end if
    end for
    increment j
end while

long-run UE rate and energy efficiency are $\bar{R}_{\alpha_0}(S^*)$ and $\bar{E}_{\alpha_0}(S^*)$, respectively. Algorithm 2.1 and algorithm 2.2 find the optimum shaping parameter α_R and α_E that maximizes the average long-run UE rate and energy efficiency, respectively, without compromising on fairness achieved with fixed scheduling scheme at S^*. Let S'^* and S''^* be the optimal sectorization scheme at α_R obtained using algorithm 2.1 and α_E obtained using algorithm 2.2, respectively.

The input to the Algorithm 2.1 is the instantaneous rate $R_{k,s}$ of all UEs, obtained in Section III-A1; $\bar{R}_{\alpha}(S)$, $J_{\alpha}(S)$, and $\bar{E}_{\alpha}(S)$ are calculated using the relation $t_s \propto K_s^{\alpha}$ in (2.20), (2.21), and (2.22), respectively for all possible sectorization schemes $S \in \mathcal{S}$. Next, a counter j is initialized with a suitable step size $\hat{\delta}$. For the jth iteration, we search for α_R (if any) such that $\bar{R}_{\alpha_R}(S'^*) > \bar{R}_{\alpha_0}(S^*)$ while maintaining the required conditions $J_{\alpha_R}(S'^*) \geq J_{\alpha_0}(S^*)$ and $\bar{E}_{\alpha_R}(S'^*) \geq \bar{E}_{\alpha_0}(S^*)$. The iteration continues to increment α_j and update α_R till a stopping condition is met (as given in the algorithms). The stopping condition is explained as follows. When α is sufficiently high, variable time scheduling scheme allocates more time to the sectors with high value K_s and nearly zero time to sparsely populated sectors, thus degrading the fairness, i.e., $J_{\alpha}(S) < J_{\alpha_0}(S)$

Algorithm 2.2 α_E search algorithm

Input:$R_{k,s}$ $\forall S \in \mathcal{S}$
Output:α_E
Initialize: $j = 1, \alpha_E = \alpha_0 = 0$, $\hat{\delta} = 0.1$
Find: $S^* = \underset{S \in \mathcal{S}}{\text{argmax}}\ \bar{R}_{\alpha_0}(S), \bar{E}_{opt} = \bar{E}_{\alpha_0}(S^*)$
while $\alpha_j = \alpha_{j-1} + \hat{\delta}$ **do**
    Compute: $\bar{E}_{\alpha_j}(S)$, $J_{\alpha_j}(S)$, $\bar{R}_{\alpha_j}(S)$ $\forall S$
    if $J_{\alpha_j}(S = 360) < J_{\alpha_0}(S^*)$ **then**
        break; (*Stopping condition*)
    end if
    for $i = S^* : 360$ **do**
        if $J_{\alpha_j}(i) \geq J_{\alpha_0}(S^*)$ & $\bar{E}_{\alpha_j}(i) > \bar{E}_{opt}$ & $\bar{R}_{\alpha_j}(i) \geq \bar{R}_{\alpha_0}(S^*)$ **then**
            $\alpha_E = \alpha_j, \bar{E}_{opt} = \bar{E}_{\alpha_j}(i), S''^* = i$
        end if
    end for
    increment j
end while

$\forall S$. However, from Lemma 1 we know that for a fixed value of α the fairness index $J_\alpha(S) \geq J_\alpha(S^*)$ for $S > S^*$. Combining the above two deductions, the feasible search region of α_R, given a benchmark fairness index, is given by the condition $J_\alpha(S = 360) \geq J_\alpha(S'^*) \geq J_{\alpha_0}(S^*)$ (we take the maximum possible number of sectors $S = 360$). Therefore, during the search for α_R in Algorithm 1 we keep incrementing α_j till we have $J_{\alpha_j}(S = 360) \geq J_{\alpha_0}(S^*)$; otherwise the optimal shape parameter search algorithm stops. Similarly, Algorithm 2.2 describes the steps to find the shaping parameter α_E that maximizes gNB energy efficiency without compromising on the average long-run UE rate and the fairness achieved using fixed scheduling at S^*.

Remark 2.4. *In uniform UE distribution, difference in the values of K_s is minimal, i.e., its variance is nearly zero. Thus, the scheduled time of each sector is approximately the same and is equivalent to the fixed time scheduling scheme. In contrast, the variance of K_s is significant for non-uniformly distributed UEs within the cell.*

2.3.2 Optimal Sectorization Scheme with Estimated UE Position Information

In the above study, we assumed that gain of the beam within a sector is $N_t G_0$ and zero outside. In practice, the array factor vector of a broadside ULA with half wavelength spacing is [71]:

$$\mathbf{a}(\theta) = \frac{1}{\sqrt{N_t}}[1 \;\; e^{jk\bar{d}\sin(\theta)} \ldots e^{j(N_t-1)k\bar{d}\sin(\theta)}]^T, \;\; \text{s.t. } \|\mathbf{a}(\theta)\|_2 = 1 \tag{2.29}$$

where $\bar{d}$ is the spacing between antenna elements, θ is the angle deviation from the direction of maximum array gain, and $k\bar{d} = \pi$ is the uniform phase shift between two antenna elements. Thus, the resulting gain pattern of the ULA with the array factor given by (2.29) at an angle θ is:

$$G_t(\theta) = N_t \left| \left[\frac{1}{N_t} \frac{\sin(\frac{N_t \pi}{2} \sin(\theta))}{\sin(\frac{\pi}{2} \sin(\theta))} \right] \right|^2, \text{ for } -\pi \leq \theta \leq \pi \tag{2.30}$$

with first null beamwidth (FNBW) of the broadside ULA being $\Theta = 2\left[\frac{\pi}{2} - \cos^{-1}(2/N_t)\right]$. The derivation of ULA gain is provided in Appendix B.

The position estimation is assumed to be performed at UEs that are continuously listening to the channel for pilot symbols spread over the entire OFDM symbol bandwidth. This data is then reported back to the gNB. Also, we assume perfect time synchronization between the transmitter and receiver. We define effective AoA (EAoA), denoted by Ψ, as

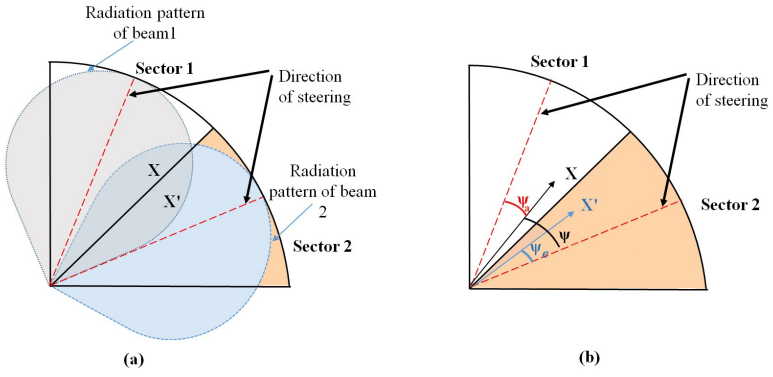

Figure 2.2: (a) Pictorial representation of true position **X** and estimated position **X′** of a UE along with the actual beam coverage region considering practical radiation pattern. (b) Demonstration of EAoA of the UE; Ψ is the true EAoA and Ψ_e is the estimated EAoA with respect to sector 2, whereas Ψ_a is the true EAoA of UE with respect to sector 1.

the effective angle of signal arrival at the UE with respect to the beam steering direction of the serving sector. As a result, $\gamma_{n,k}$ given by (2.5) is a function of EAoA as well, in addition to distance d from gNB, i.e.,

$$\gamma_{n,k}(\Psi) = \frac{G_t(\Psi)G_r|h_{n,k}|^2 PL_k}{N_0 B/N_c} \tag{2.31}$$

This parameter is used at gNB for resource allocation purpose as described in Section 2.3.1.1. Due to error in angle estimation, the estimated EAoA of UE at gNB is Ψ_e, with $|\Psi - \Psi_e| \geq 0$, as shown in Fig. 2. Therefore, $\gamma_{n,k}(\Psi_e)$ of kth UE over nth subcarrier is the effective channel and location parameter at gNB, while $\gamma_{n,k}(\Psi)$ being the original value.

The UE position information variables are d and Ψ. Let τ be the time-of-flight of signal from gNB to UE. In case of a noiseless ideal channel and $G_r = 1$, using ToA and AoA methods, (d, Ψ) are jointly estimated from the equations: $\tau = d/c$, and $P_r = P_t^{Pilot} G(\Psi)/(4\pi d/\lambda)^2$, where c is the speed of light, P_t^{Pilot} is the known transmitted pilot signal power, and P_r is the received power at distance d and angle Ψ. In case of a fading and noisy channel, there will be error in position estimation. At UE, we estimate the position-related parameters Ψ and τ from LoS received signal only, assuming no NLoS components are received. The channel gain β_m, for $m = 1, 2 \ldots, N$, for a UE with Ψ EAoA and corresponding $\mathbf{a}(\Psi)$ unit norm array response (given by (2.29)) is nearly same for all its elements, i.e., $\beta_m \approx \beta$. Then the channel vector is:

$$\mathbf{h} = \sqrt{N_t}\beta e^{-j2\pi f_c \tau}\mathbf{a}^H(\Psi). \tag{2.32}$$

At the gNB, OFDM signal x is multiplied by array factor precoding vector $\mathbf{a}(\phi)$, where ϕ is ULA steering direction relative to the direction of maximum antenna gain. Since the transmitted power of the OFDM symbol with N transmitting antennas is P_t, the received signal is:

$$y = \sqrt{N_t}\beta e^{-j2\pi f_c \tau}\mathbf{a}^H(\Psi)\mathbf{s} + \nu \tag{2.33}$$

where $\mathbf{s} = \mathbf{a}(\phi)x$ is the transmitted signal with $E[\mathbf{s}^H\mathbf{s}] = P_t$, $\beta = \mathbb{E}_h\left[h\sqrt{\frac{(d_0/d)^l}{(4\pi d_0/\lambda)^2}}\right]$, h is small scale fading parameter of each subcarrier of OFDM symbol, d_0 is the reference distance, l is the LoS path loss exponent, and ν is the noise with distribution $\mathcal{N}(0, \sigma^2)$.

Here, other than τ and Ψ all other parameters are known apriori. Let $\Gamma = [\tau \;\; \Psi]^T \in \mathcal{R}^{2\times 1}$ denote the vector of unknown channel parameters. We define $\hat{\Gamma} = [\tau_e \;\; \Psi_e]^T$ to be an unbiased estimator of Γ, where τ_e and Ψ_e are unbiased estimator of ToA and EAoA (Fig. 2). Also, let $\mathcal{G}$ denote the number of transmissions required for UE position estimation

using narrow beams. Then the lower bound on position error variance with unbiased estimator $\hat{\Gamma}$ is provided by the Cramér-Rao Lower Bound (CRLB) [72] as:

$$\text{var}(\hat{\Gamma} - \Gamma) \geq -\left[\mathbb{E}_{\mathbf{Y}|\Gamma}\left(\frac{\partial^2 \log f(\mathbf{Y}|\Gamma)}{\partial \Gamma \partial \Gamma^T}\right)\right]^{-1} \equiv (\mathbf{F}(\Gamma))^{-1} \tag{2.34}$$

where $\mathbf{Y} = [y^1, \ldots, y^{\mathcal{G}}]^T$, $\mathbb{E}_{\mathbf{Y}|\Gamma}[\cdot]$ denotes parametrized expectation function for Γ, $f(\mathbf{Y}|\Gamma)$ is the conditional likelihood of $\mathbf{Y}$ given Γ, and $\mathbf{F}(\Gamma)$ is the Fisher Information Matrix (FIM).

Lemma 2: The FIM for the received signal is given as:

$$\mathbf{F}(\Gamma) = \frac{1}{N_0 B}\sum_{g=1}^{\mathcal{G}} \text{Re}(\nabla y^g \nabla^H y^g). \tag{2.35}$$

Proof: Given in Appendix C.

Here $\text{Re}(\cdot)$ denotes real part operator, and ∇y^g is gradient of y^g with respect to Γ, given as:

$$\nabla y^g = \begin{bmatrix} -j2\pi f_c \sqrt{N_t}\beta \exp\left(-j2\pi f_c \tau\right)\mathbf{a}^H(\Psi)\mathbf{a}(\phi)x^g \\ \frac{-j2\pi \bar{d}}{\lambda} cos\Psi \sqrt{N_t}\beta \exp\left(-j2\pi f_c \tau\right)\mathbf{a}^H(\Psi)\mathbf{\Lambda}\mathbf{a}(\phi)x^g \end{bmatrix}. \tag{2.36}$$

$\mathbf{\Lambda} = \text{diag}[0\ 1 \ldots (N_t - 1)]$. We assume that the gNB has a separate ULA for each sector and the beam in each sector is steered in the direction of its maximum antenna gain, i.e., $\phi = 0^o$. Then, $\mathbf{F}(\Gamma)$ is given by (2.37).

The CRLBs $\kappa(\tau)$ and $\kappa(\Psi)$ for τ and Ψ respectively are the diagonal elements of the CRLB matrix $\kappa(\Gamma)$ where $\kappa(\Gamma) = (\mathbf{F}(\Gamma))^{-1}$. The position error bound (PEB) is expressed as the square root of the addition of diagonal elements of $\kappa(\Gamma)$ as [73]:

$$\text{PEB} = \sqrt{[(\mathbf{F}(\Gamma))^{-1}]_{1,1} + [(\mathbf{F}(\Gamma))^{-1}]_{2,2}} = \sqrt{\kappa(\Psi) + \kappa(\tau)} \tag{2.38}$$

where

$$\begin{aligned} \kappa(\Psi) &= \frac{N_0 B/(\mathcal{G}P_t)}{(\frac{2\pi\bar{d}}{\lambda})^2 cos^2(\Psi)\beta^2\left[\sum_{n_t=0}^{N_t-1} n_t^2 - \left(\sum_{n_t=0}^{N_t-1} n_t\right)^2/N_t\right]} \\ \kappa(\tau) &= \frac{N_0 B}{\mathcal{G}P_t}\frac{N_t\sum_{n_t=0}^{N_t-1} n_t^2}{(2\pi f_c)^2\beta^2\left[\sum_{n_t=0}^{N_t-1} n_t^2 - \left(\sum_{n_t=0}^{N_t-1} n_t\right)^2/N_t\right]}. \end{aligned} \tag{2.39}$$

$$\mathbf{F}(\Gamma) = \frac{\mathcal{G}P_t}{N_0 B}\begin{bmatrix} (2\pi f_c)^2\beta^2 N_t & (2\pi f_c)(\frac{2\pi\bar{d}}{\lambda})\beta^2 cos(\Psi)\sum_{n_t=0}^{N_t-1} n_t \\ (2\pi f_c)(\frac{2\pi\bar{d}}{\lambda})\beta^2 cos(\Psi)\sum_{n_t=0}^{N_t-1} n_t & (\frac{2\pi\bar{d}}{\lambda})^2 cos^2(\Psi)\beta^2\sum_{n_t=0}^{N_t-1} n_t^2 \end{bmatrix} \tag{2.37}$$

Since $1/f_c \ll 1$, CRLB $\kappa(\tau) \ll \kappa(\Psi)$. Hence, for $\bar{d} = \lambda/2$, we have

$$\begin{aligned} \text{PEB} &\approx \sqrt{\kappa(\Psi)} \\ &= \frac{\sqrt{N_0 B/(\mathcal{G} P_t)}}{\frac{h\lambda}{4d_0}(\frac{d_0}{d})^{l/2} cos(\Psi) \left[\sum_{n_t=0}^{N_t-1} n_t^2 - \left(\sum_{n_t=0}^{N_t-1} n_t\right)^2 / N_t\right]^{1/2}}. \end{aligned} \tag{2.40}$$

Let the error in EAoA is $\psi = (\Psi - \Psi_e)$ (Fig. 2). Upper bound on the variance of ψ is quite complex to derive. Nevertheless, we can find the distribution of ψ using PEB assuming very low SNR at cell edge in the worst case, as stated below.

Lemma 3: The distribution of localization error ψ of an UE having EAoA Ψ and HPBW Θ with respect to sth sector is given as:

$$\text{Prob}(|\psi| \leq \epsilon) = \left[1 - \frac{\kappa(\Psi)}{\epsilon^2}\right]. \tag{2.41}$$

Proof: Using Chebyshev's inequality we have

$$\text{Prob}(|\psi| \geq \epsilon) \leq \left[\frac{\text{variance}(\psi)}{\epsilon^2}\right] = \frac{\kappa(\Psi)}{\epsilon^2} \quad \text{as the CRLB.}$$

$$\Rightarrow \text{Prob}(|\psi| \leq \epsilon) = \left[1 - \frac{\kappa(\Psi)}{\epsilon^2}\right], \quad \text{for} \quad -\frac{\Theta}{2} \leq \Psi \leq \frac{\Theta}{2}.$$

□

2.3.3 Complexity analysis

2.3.3.1 Subcarrier and Power Allocation

The joint subcarrier–power allocation with minimum UE rate constraint problem $\mathcal{P}1$ is a mixed integer NP-hard problem. For a system with K_s UEs and N_c subcarriers, $\mathcal{P}1$ has $K_s N_c$ variables, atleast $K_s + N_c$ constraints, total UE–subcarrier $K_s^{N_c}$ combinations, and $K_s^{N_c}$ comparisons. For power allocation per UE–subcarrier combination, complexity is $\mathcal{O}(K_s N_c \log_2 N_c)$. Thus, the complexity of solving $\mathcal{P}1$ using exhaustive search is $\mathcal{O}(K_s^{N_c}(K_s N_c \log_2 N_c))$.

On the other hand, sub-optimum approach (Steps (i) through (iv)) is computationally less complex. It requires $K_s N_c$ comparisons in Step (ii), at most $(K_s - 1)N_c$ multiplications and $(K_s - 1)N_c$ summations in Step (iii) to compute cost functions, approximately $2N_c^2$ comparisons for subcarrier reallocation, and in the worst case $N_c \log_2 N_c$ power allocation computations in Step (iv). Hence, the overall complexity of sub-optimal approach is reduced to $\mathcal{O}(N_c^2)$.

2.3.3.2 Sectorization

To find the average long-run UE rate with total number of sectors S in the worst case scenario of all sectors being active, approximately $S(3K_sN_c + 2N_c^2 + N_c\log_2 N_c)$ computations are required. Therefore, to find S^* in fixed time scheduling scheme an exhaustive search over $\forall S \in \mathcal{S}$ is performed. As a result, the worst case complexity to estimate S^* is $\mathcal{O}(|\mathcal{S}|SN_c^2)$, where S can have the maximum value of 360 for $\Theta = 1^o$. In variable time scheduling, if η_{itr} iterations are required to find α, then the worst case complexity is $\mathcal{O}(\eta_{itr}|\mathcal{S}|SN_c^2)$.

2.3.3.3 Reduced-complexity Method

In reduced complexity method, subcarrier allocation is the same as in $\mathcal{P}1$, but it is computed for only one sector per sectorization scheme to form the dictionary at gNB, which is updated only when channel statistics change. Accordingly, the complexity reduces to $\mathcal{O}(|\mathcal{S}|N_c^2)$. Further, to find $\hat{S}^*$ for a given UE population, maximum $|\mathcal{S}|N_c$ comparisons are needed.

2.4 Simulation Results and Discussion

In this section, we present the numerical simulation results generated using MATLAB with varying system configurations. For the simulation set-up, we consider a system operating at 60 GHz carrier frequency with $B = 1$ GHz bandwidth, and $N_c = 30$ subcarriers. We vary the beamwidth in the range $1^o \leq \Theta \leq 30^o$ in steps of 1^o. Various other channel and system parameters considered are: Rician fading parameter $= 8$ dB [74], EIRP $= 52$ dBm, $G_0 = 5$ dBi, cell radius $= 200$ m, $R_0 = 10$ Mbps, noise spectral density $N_0 = -174$ dBm/Hz, $\zeta_{LoS} = 15, \zeta_{NLoS} = 45$, and outage SNR threshold $= -6$ dB. We execute the simulations broadly for two cases: firstly considering no localization error for the two scheduling schemes, namely, fixed time and variable time scheduling, and secondly considering localization error with fixed time scheduling.

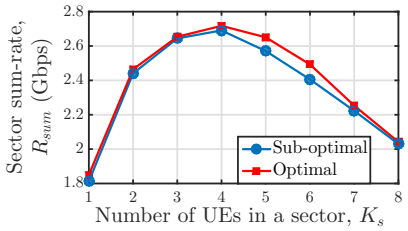

Figure 2.3: Sector sum rate versus number of UEs plot for optimal and sub-optimal resource allocation techniques.

2.4.1 Optimal sectorization scheme with perfect UE location information

2.4.1.1 Sub-optimum Resource Allocation per Sector

Due to the NP-hard nature of $\mathcal{P}1$, per-sector resource allocation is performed in a sub-optimal way that maximizes the sector's instantaneous sum rate while satisfying minimum rate constraints. Fig. 2.3 compares per-sector sum rate achieved using optimal resource allocation and using sub-optimal method for different values of K_s, using Monte-Carlo simulations. As the computation time for a single Monte-Carlo iteration in optimal resource allocation is of order $K_s^{N_c}$, to perform simulations in this case we took $N_c = 8$ and $B = 250$ MHz while keeping the other parameters same as described above. Form Fig. 2.3 we observe that both resource allocation schemes show a similar trend on varying K_s, where the optimal solution gives an upper bound.

2.4.1.2 Fixed Time Scheduling

With decreasing sector beamwidth, the same frequency band can be used in the cell more often, thereby increasing the spatial reuse factor. For a fixed UE population, although a narrower beam provides the benefit of increased cell spatial reuse factor, Fig. 2.4(a) shows that a narrow beam does not necessarily result in maximization of the average long-run UE rate $\bar{R}$. The decrease in $\bar{R}$ is due to two reasons: (i) with a beam serving very few UEs, the channel utilization is not efficient (*Remark* 2.2), and (ii) total delay between the next schedule of each sector increases with more cell partitions.

Suppose S_R^* is the optimal sectorization scheme which offers maximum $\bar{R}$ without gNB energy optimization constraint. Fig. 2.4(a) shows that there exists an S_R^* corresponding to $\Theta_{min} \leq \Theta^* \leq \Theta_{max}$, for which $\bar{R}$ is maximized. Moreover, the optimal

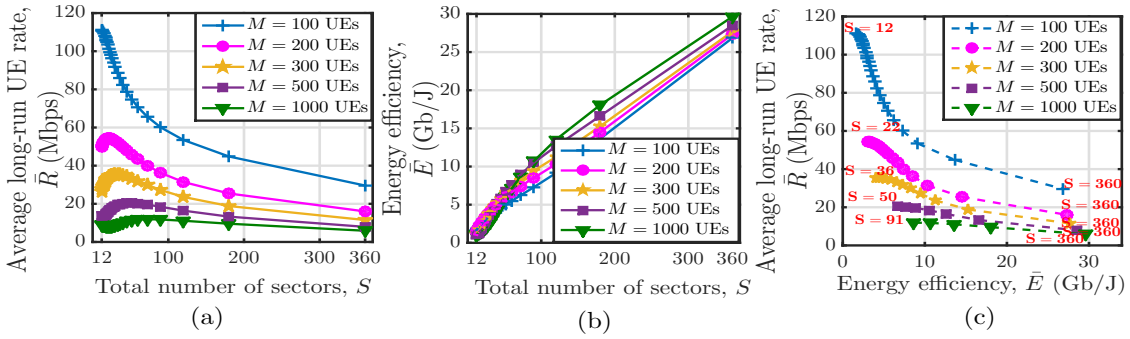

Figure 2.4: (a) Average long-run UE rate versus total number of sectors plot for uniformly distributed UE population; (b) gNB energy efficiency versus total number of sectors plot for uniformly distributed UE population. (c) Pareto front for average long-run UE rate and gNB energy efficiency optimization.

sector beamwidth gets narrower with increasing UE density. Fig. 2.4(b) demonstrates that $\bar{E}$ is nearly proportional to cell sectorization, which is because a higher spatial reuse factor increases the cell sum-throughput with minimal increase in transmit energy requirement for one complete cell sweep duration. From combined observations of Fig. 2.4(a) and 2.4(b), we conclude that for $S \geq S_R^*$ a Pareto front exists between $\bar{E}$ and $\bar{R}$ as captured in Fig. 2.4(c). For instance, for $M = 200$ with corresponding $S_R^* = 22$, a Pareto optimal condition between $\bar{R}$ and $\bar{E}$ is observed in Fig. 2.4(c) over the range of $S = [22, 360]$. Thus, the sectorization schemes $S < S_R^*$ are not optimal either from $\bar{R}$ or from $\bar{E}$ point of view.

Reduced complexity method: For $\bar{R}$ maximization, as discussed in Section 2.3.1.2, we estimate the sub-optimal sectorization scheme $\hat{S}^*$, at which maximum $\bar{R}$ is achieved, with a considerably reduced number of computations. For this, we generate the dictionary $\mathcal{R}_{sum}$ at the gNB using Monte-Carlo simulations. Fig. 2.5(a) shows the dependency of sector sum rate on K_s and S. Fig. 2.5(b) shows comparison of the sub-optimal $\hat{S}^*$ with the optimal S^*. We observe that with the reduced complexity method $\hat{S}^*$ is nearly affine with UE population (below $M = 50$, $S = 12$, since maximum beamwidth possible is 30^o) for $\Theta_{min} \leq \Theta^* \leq \Theta_{max}$. Moreover, $\hat{S}^*$ is quite close to S^*. There is an error in estimation $|S^* - \hat{S}^*|$ because we construct the dictionary R_{sum} by using statistical UE and channel distribution, and approximation in (2.26), whereas in estimation of S^* we use UE instantaneous channel state information. Thus, we can get quite close results with much reduced complexity as compared to exhaustive search method, and the update in

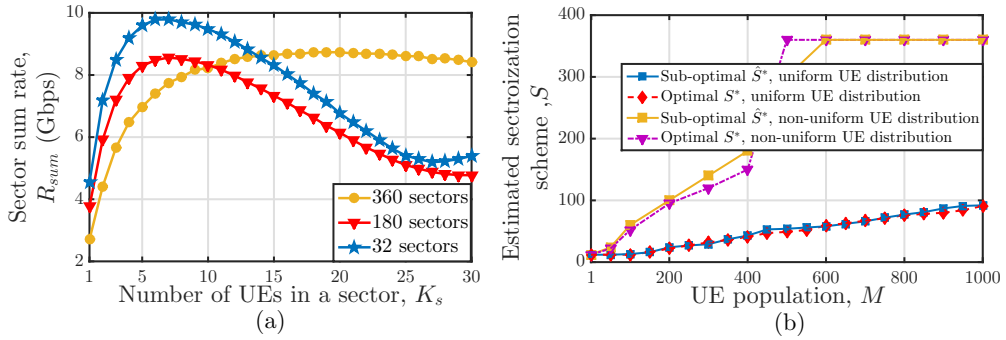

Figure 2.5: (a) Plot of sum rate per sector versus number of UEs in the sector for three different sectorization schemes. (b) Comparison of optimal S^* obtained through exhaustive search method and sub-optimal $\hat{S}^*$ obtained using reduced complexity search method for uniform and non-uniform UE distribution.

the dictionary is required only when statistical channel parameters change.

2.4.1.3 Variable Time Scheduling

We simulate non-uniform UE distribution by dividing the cell into 6 zones, i.e., $Z = 6$ with p_z vector for the zones being $[0.9, 0.05, 0.03, 0.01, 0.008, 0.002]$. As described in Section III-A3, we consider fixed time scheduling scheme as a benchmark for variable time scheduling scheme. Thereafter, we use Algorithm 1 and Algorithm 2 to find the optimal shaping parameter α_R and α_E, respectively, for improved performance over fixed scheduling. Fig. 2.6(a) illustrates that there exits a non-zero α_R that offers a higher value of average long-run UE rate $\bar{R}_{\alpha_R}(S'^*)$ compared to fixed scheduling scheme $\bar{R}_{\alpha_0}(S^*)$, such that $\bar{E}_{\alpha_R}(S'^*) \geq \bar{E}_{\alpha_0}(S^*)$ and $J_{\alpha_R}(S'^*) \geq J_{\alpha_0}(S^*)$ (as shown in Fig. 2.6(a)).

Similarly, a non-zero α_E exists that offers an increased energy efficiency attainable $\bar{E}_{\alpha_E}(S''^*)$ as compared to energy efficiency achieved using fixed scheduling scheme $\bar{E}_{\alpha_0}(S^*)$, such that $\bar{R}_{\alpha_E}(S''^*) \geq \bar{R}_{\alpha_0}(S^*)$ and $J_{\alpha_E}(S''^*) \geq J_{\alpha_0}(S^*)$ (as shown in Fig. 2.6(b)). We also note from the simulation results that $\alpha_E \geq \alpha_R$. For example, for $M = 200$ non-uniformly distributed UEs, the fixed scheduling scheme has $S^* = 95, \alpha = 0$, $\bar{R}_{\alpha_0}(S^*) = 12.58$ Mbps, and $\bar{E}_{\alpha_0}(S^*) = 2.13$ Gb/J. With variable time scheduling the performance is improved. At the value of α equal to $\alpha_R = 0.7$ a value of $\bar{R}_{\alpha_R}(S'^*) = 14.79$ Mbps is achieved at $S'^* = 120$. If the shaping parameter is set to $\alpha = \alpha_E = 1.4$ with $S''^* = 150$, we get gain in gNB energy efficiency, i.e, $\bar{E}_{\alpha_E}(S''^*) = 3.44$ Gb/J.

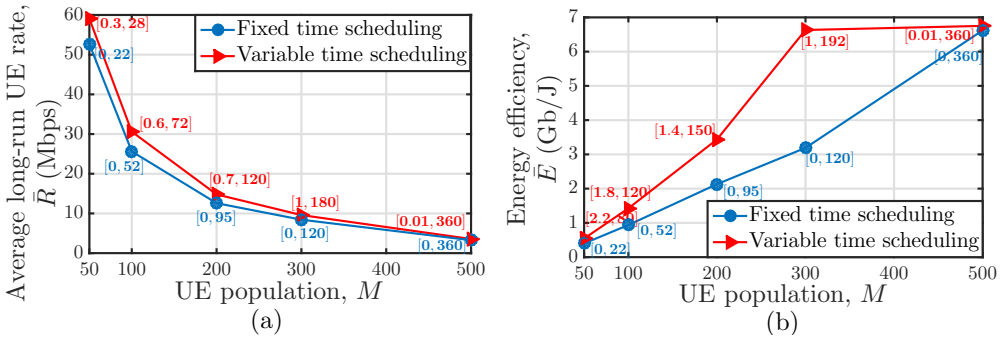

Figure 2.6: Improvement in of $\bar{R}$ and $\bar{E}$ using variable time scheduling scheme over fixed time scheduling scheme. (a) shows the improvement in maximum achievable average long-run UE rate for different UE population, using variable time scheduling scheme with $[\alpha = \alpha_R, S = S'^*]$ over fixed time scheduling scheme at $[\alpha = \alpha_0, S = S^*]$; and (b) shows the improvement in maximum achievable gNB energy efficiency using variable time scheduling scheme with $[\alpha = \alpha_E, S = S''^*]$ over fixed time scheduling scheme at $[\alpha = \alpha_0, S = S^*]$.

2.4.2 Optimal Sectorization Scheme with Estimated UE Position Information

Due to localization error some UEs that are wrongly detected to be in another sector will experience different EAoA (increased EAoA). Since in practical scenario beam gain has a fan shaped pattern given by (2.30), gain falls sharply outside HPBW and the UEs lying in this area will be the main attribute for the decrease in average long-run UE rate $\bar{R}$ (if any). Thus, the effect of localization error on the $\bar{R}$ is mainly attributed by the UEs that are wrongly detected to be in another sector.

In the simulations, we generate the localization error for each UE using the distribution given by (2.41) and the antenna gain at Ψ EAoA using (2.30). Since we have the knowledge of only lower bounds on variance of the estimator, to study worst-case scenario we carry out simulations assuming $\mathcal{G} = 2$ and minimum SNR requirement at cell edge to be -6 dB. The result in Fig. 2.7(a) illustrates a decrease in PEB with increasing sector partitions. The PEB obtained from our simulation is of increased magnitude as compared to the work in [62]. The reason being that the increase in SNR (due to enhanced beam directivity) is nullified by reduced transmit power, thereby keeping SNR invariant of beamwidth.

We compare the simulation results of three cases: (a) ideal case of resource allocation without localization error and constant beam gain within the sector ($G = NG_0$), (b)

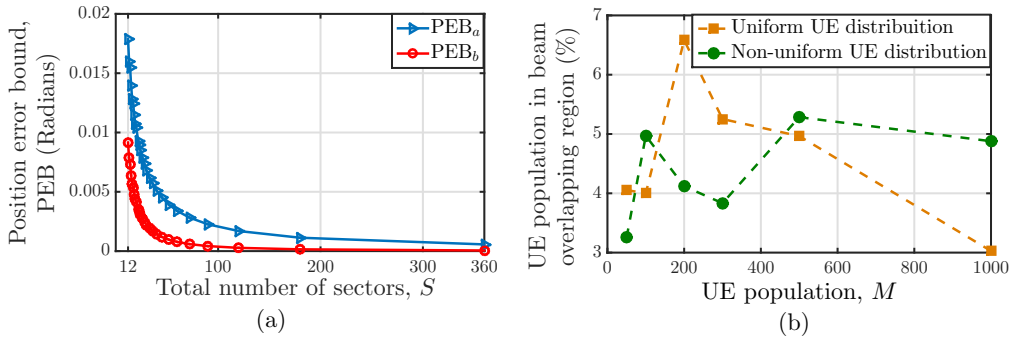

Figure 2.7: (a) Position error bound of Ψ_e versus number of sectors in worst-case scenario. PEB_a is the PEB obtained using (2.40); PEB_b is the PEB achieved in [62]. (b) Percentage of UEs lying in the beam overlapping region due to localization error.

resource allocation with no localization error but angle-dependent beam gain (given by (2.30)), and (c) resource allocation with localization error (given by (2.41)) along with angle-dependent beam gain (given by (2.30)). Fig. 2.8(a) and 2.8(b) show that, though $\bar{R}$ in case (b) is of reduced magnitude as compared to $\bar{R}$ in case (a), the nature of $\bar{R}$ as a function of S is same for both. Moreover, in case (c) $\bar{R}$ further degrades slightly with localization error. However, S^* remains invariant.

From the results in Fig. 2.4(a) we noted that, on increasing M, Θ^* shifts to a smaller value; thus K_s in a sector is such that it maximizes the sector sum rate. Moreover, our insight is that with reducing HPBW the beam overlapping region shrinks. We omit the

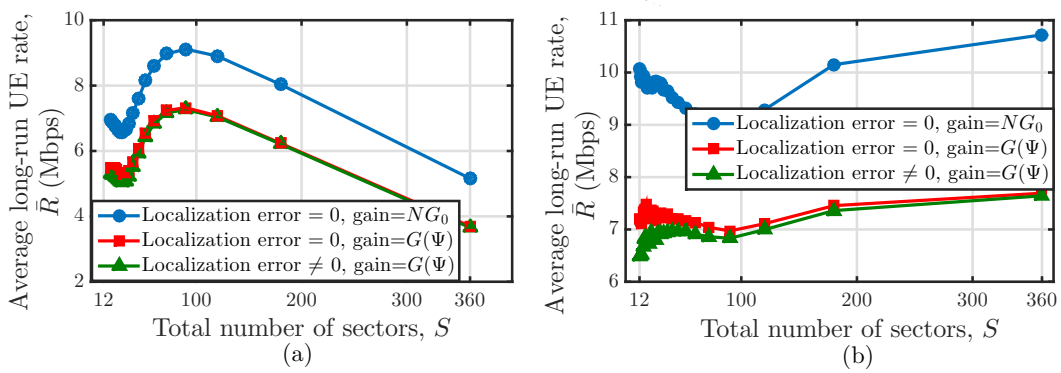

Figure 2.8: Average long-run UE rate versus total number of sectors plot for (a) 1000 UEs uniformly distributed in the cell, and (b) 500 UEs non-uniformly distributed in the cell with probability of distribution of UEs in a 6 non-overlapping zones of the being $[0.9, 0.05, 0.03, 0.01, 0.008, 0.002]$.

related mathematics for brevity. Consequently, the percentage of UEs falling in the overlapping region due to localization error is very small. To verify this claim in Fig. 2.7(b) we plotted the percentage of UEs falling in beam overlapping area for different sets of $(M, S^*(M))$. The figure verifies that the population in the overlapping region due to erroneous position estimation is less than 10% even for M as high as 1000. Therefore, the optimal number of sectors remains unchanged. Similar behaviour is observed with non-uniformly distributed UEs as well.

Further, from Fig. 2.8(a) and 2.8(b) we observe that the graphs have convex behaviour till some S, after which they show concavity. This is explained as follows: (i) When $\{S \in \mathcal{S} | K_s \gg N_c\}$, the subcarriers in a sector are assigned to only N_c out of K_s UEs that have best channel conditions, such that the minimum rate requirement is fulfilled for only N_c UEs. In addition to this, the cell sweep time is of very short duration for small S. (ii) When $\{S \in \mathcal{S} | K_s > N_c\}$, the subcarriers are still assigned to only N_c out of K_s UEs having best channel conditions. However, with decreasing domain size K_s, the chances of the majority of UEs having good channel conditions reduces. Further sweep time also increases with S. As a result, it decreases the average long-run UE rate. (iii) When $\{S \in \mathcal{S} | K_s \leq N_c\}$, all the UEs are allocated subcarrier such that the total sum rate is maximized with a minimum rate guarantee to all UEs. Although cell sweep time is still increasing, the gain in the instantaneous UEs rate outweighs the increased sweep duration effect. Therefore, the sector sum rate begins to improve, resulting in the concave nature of the average long-run UE rate curve.

2.5 Summary

In this chapter the performance of cellular communication at wideband mmWave frequencies serving UEs using a single analog beam from one RF chain in conjunction with scheduling operation such that radiation levels in the environment are maintained constant has been studied. The proposed sectored-cell system model employs a spatial multiplexing approach and aims to serve more than one UE during the beam sojourn time. It has been noted that, although a narrow beam provides increased channel spatial reuse, it does not necessarily result in an increased average long-run UE data rate. Therefore, to cater to a specific UE population, an optimal sector beamwidth is required that maximizes the average long-run UE rate and improves QoS such that the gNB transmit power requirement is also reduced. From the gNB perspective, it is always optimal to use the narrowest pos-

sible beamwidth. Hence, a Pareto front exists on average long-run UE rate maximization and gNB energy efficiency. Furthermore, the proposed reduced-complexity method has provided an insight that channel utilization is maximum when it has an optimum number of UEs to serve over the wideband channel. Therefore, with increasing UE population, if the number of sectors in a cell is maintained such that each sector operates at its optimum channel usage, then the highest average long-run UE rate can be achieved.

Further, it has been observed that, in the case of non-uniformly distributed UEs, the variable time scheduling scheme can further improve the average long-run UE rate and gNB energy efficiency as compared to fixed time scheduling. The results have shown that non-uniform UE distribution corresponds to shifting to a narrower beam with the increasing variance of UE distribution. Further, studies by accounting for the localization uncertainty have revealed that, in a static UE scenario, though localization error reduces average long-run UE data rate, optimal sector beamwidth selection remains unaffected, even for non-uniformly distributed UEs. The analysis of single analog beam with sectored-cell multiplexing has been extended to the case of multiple concurrent beams serving the cell in the Chapter 3.

Appendices for Chapter 2

A. Proof of Lemma 1

Lemma 1: For a fixed α and $K_s \leq N_c$, Jain's fairness index J is an increasing function of S, when resource allocation is performed using sum rate maximization approach.

Proof: Suppose there are $1 < m \leq N_c$ UEs in sth sector, such that the instantaneous rate of UEs is $r_1, r_2, \cdots, r_m$. Let $\alpha = 0$ and $t_s = 1$ unit. Then by (2.21), we have

$$J(S) = \frac{1}{m} \frac{\left(\frac{r_1}{S} + \cdots + \frac{r_m}{S}\right)^2}{\left(\left(\frac{r_1}{S}\right)^2 + \cdots + \left(\frac{r_m}{S}\right)^2\right)} = \frac{1}{m} \frac{(r_1 + \cdots + r_m)^2}{({r_1}^2 + \cdots + {r_m}^2)} = \frac{1}{m} \frac{x^2}{y} \text{ (say).}$$

Now suppose the sectorization scheme is changed to $\tilde{S} = S + 1$ with UEs position in the cell unchanged. This results in redistribution of UEs among the sectors. With increasing number of sectors the degree of spatial multiplexing increases, leading to increased instantaneous sum rate of the UEs. Let us consider that due to redistribution one of the UEs falls into another sector while other $m - 1$ UEs still remain together in one sector. Let the

increment in instantaneous rate of the mth UE falling into another sector be δ. Therefore,

$$\begin{aligned} J(\tilde{S}) &= \frac{1}{m}\frac{(r_1+\cdots+r_m+\delta)^2}{(r_1^2+\cdots+(r_m+\delta)^2)} = \frac{1}{m}\frac{(x+\delta)^2}{(y+\delta^2+2\delta r_m)} \\ &\geq \frac{1}{m}\frac{(x+\delta)^2-(\delta^2+2\delta r_m)}{(y+\delta^2+2\delta r_m)-(\delta^2+2\delta r_m)} \qquad \text{(since } 0 \leq J(S) \leq 1\text{)} \\ &= \frac{1}{m}\frac{(x^2+2\delta(r_1+\cdots+r_{m-1}))}{y} \geq \frac{1}{m}\frac{x^2}{y}. \end{aligned}$$

Hence, $J(\tilde{S}) \geq J(S)$, i.e, $J(S)$ is an increasing function of S. □

B. Derivation of Array Gain

$$G_t(\theta) = N_t \left| \left[\frac{1}{N_t} \frac{\sin(\frac{N_t\pi}{2}\sin(\theta))}{\sin(\frac{\pi}{2}\sin(\theta))} \right] \right|^2, \text{ for } -\pi \leq \theta \leq \pi \tag{B.1}$$

Proof: Gain of an broadside ULA, with 100% efficiency, with respect to angle of departure θ of a signal from direction of maximum array gain is given as [71]

$$G_t(\theta) = \frac{4\pi|AF(\theta)|^2}{\int_0^{2\pi}\int_0^{\pi}|AF(\theta)|^2\sin\theta \, \mathrm{d}\theta \, \mathrm{d}\hat{\phi}}$$

where $AF(\theta)$ is the normalized antenna array factor. For zero phase difference excitation and half wavelength antenna spacing, it is given as [71]

$$AF(\theta) = |\mathbf{a}(\theta)|^2 = \frac{1}{N_t}\left[\frac{\sin(\frac{N_t\pi}{2}\sin\theta)}{\sin(\frac{\pi}{2}\sin\theta)}\right].$$

$$\text{Let} \qquad \mathcal{V} = \int_0^{\pi}|AF(\theta)|^2\sin\theta \, \mathrm{d}\theta = \int_0^{\pi}\left|\frac{\sin(\frac{N_t\pi}{2}\sin\theta)}{N_t\sin(\frac{\pi}{2}\sin\theta)}\right|^2 \sin\theta \, \mathrm{d}\theta.$$

Suppose $\omega = 0.5\pi\cos\theta$, then we have

$$\mathcal{V} = \frac{2}{N_t^2\pi}\int_{-\pi/2}^{\pi/2}\left|\frac{\sin(N_t\omega)}{\sin(\omega)}\right|^2 \mathrm{d}\omega. \tag{B.2}$$

$$\text{Since, } \frac{\sin(N_t\omega)}{\sin(\omega)} = \frac{e^{jN_t\omega}-e^{-jN_t\omega}}{e^{j\omega}-e^{-j\omega}} = \frac{e^{j\omega}}{e^{jN_t\omega}}\frac{e^{2jN_t\omega}-1}{e^{2j\omega}-1} = e^{-j(N_t-1)\omega}\sum_{k=0}^{N_t-1}e^{2jk\omega}.$$

By Fourier series expansion,

$$\sum_{k=-\infty}^{+\infty}a_k e^{jk\omega} = \frac{\sin(N_t\omega)}{\sin(\omega)} = e^{-j(N_t-1)\omega}\sum_{k=0}^{N_t-1}e^{2jk}\omega$$

with only N_t non-zero coefficient of unity magnitude. Therefore, by Parseval's Identity we have

$$\frac{1}{2\pi}\int_{-\pi}^{\pi}|f(x)|^2\,\mathrm{d}x=\sum_{k=-\infty}^{\infty}|a_k|^2=N_t.$$

Hence, (B.2) can be solved as: $\mathcal{V}=(2/N_t^2\pi)(1/2)\int_{-\pi}^{\pi}\left|\frac{\sin N_t\omega}{\sin\hat{\phi}}\right|^2\,\mathrm{d}\omega=2/N_t$. Therefore, in general, the array gain at an angle θ from the direction of maximum gain is

$$\begin{aligned}G_t(\theta)&=\frac{4\pi|AF(\theta)|^2}{\frac{2}{N_t}\int_0^{2\pi}\mathrm{d}\hat{\phi}}=N_t\,|AF(\theta)|^2\\&=N_t\left|\left[\frac{1}{N_t}\frac{\sin(\frac{N_t\pi}{2}\sin(\theta))}{\sin(\frac{\pi}{2}\sin(\theta))}\right]\right|^2,\text{for }-\pi\le\theta\le\pi.\end{aligned}$$

□

C. Proof of Lemma 2

Lemma 2: The FIM for the received signal is given as:

$$\mathbf{F}(\Gamma)=\frac{1}{N_0B}\sum_{g=1}^{\mathcal{G}}\mathrm{Re}(\nabla y^g\nabla^H y^g). \tag{C.1}$$

Proof: From CRLB definition [72], we have

$$\mathrm{var}(\hat{\Gamma}-\Gamma)\ge-\left[\mathbb{E}_{\mathbf{Y}|\Gamma}\left(\frac{\partial^2\log f(\mathbf{Y}|\Gamma)}{\partial\Gamma\partial\Gamma^T}\right)\right]^{-1}\equiv(\mathbf{F}(\Gamma))^{-1}$$

where $\mathbf{Y}=[y^1,\ldots,y^{\mathcal{G}}]^T$. Let $w(\Gamma)=\sqrt{N}\beta e^{-j2\pi f_c\tau}\mathbf{a}^H(\Psi)\mathbf{s}$. Then, for gth transmission (2.33) can be written as $y^g=w^g(\Gamma)+\nu^g$. Hence, the log-likelihood function is

$$\begin{aligned}f(\mathbf{Y}|\Gamma)&=\frac{1}{\sqrt{2\pi\sigma^2}}\left[e^{-\frac{1}{2\sigma^2}(y^1-w^1(\Gamma))},\ldots,e^{-\frac{1}{2\sigma^2}(y^{\mathcal{G}}-w^{\mathcal{G}}(\Gamma))}\right]^T\\\Rightarrow\log f(\mathbf{Y}|\Gamma)&=\left[-\frac{1}{2}\log2\pi\sigma^2-\frac{1}{2\sigma^2}(y^1-w^1(\Gamma)),\ldots,-\frac{1}{2}\log2\pi\sigma^2-\frac{1}{2\sigma^2}(y^{\mathcal{G}}-w^{\mathcal{G}}(\Gamma))\right]^T.\end{aligned}$$

Taking the first derivative, we have:

$$\frac{\partial f(\mathbf{Y}|\Gamma)}{\partial\Gamma}=-\frac{1}{2\sigma^2}\left[\nabla y^1,\ldots,\nabla y^{\mathcal{G}}\right]^T.$$

Taking second derivative and negative expected value over Γ, we get

$$-\mathbb{E}_{\mathbf{Y}|\Gamma}\left(\frac{\partial^2 f(\mathbf{Y}|\Gamma)}{\partial\Gamma\partial\Gamma^T}\right) = \frac{1}{2\sigma^2}\sum_{g=1}^{\mathcal{G}}\text{Re}(\nabla y^g \nabla^H y^g)$$
$$\Rightarrow \mathbf{F}(\Gamma) = \frac{1}{N_0 B}\sum_{g=1}^{\mathcal{G}}\text{Re}(\nabla y^g \nabla^H y^g).$$

□

Acknowledgement

The content of this chapter has been based on the research publication:

(i) N. Varshney and S. De, "Optimum downlink beamwidth estimation in mmWave communications," *IEEE Trans. Commun.* , vol. 69, no. 1, pp. 544-557, Jan. 2021.

Chapter 3

Multi-RF Beamforming for Multi-user Wideband mmWave Communications

3.1 Introduction

The advancement of mmWave beamforming technologies and numerous outdoor channel measurement campaigns [75, 76] encourages to probe into mmWave outdoor commercial cellular systems, especially where user density per cell is sufficiently high. In the previous chapter we analyzed the sectored-cell framework with a single analog beam for serving a large user population. We now extend the proposed sectored-cell framework analysis to the case of multiple concurrently active beams generated by a sub-array hybrid precoder at the gNB to obtain spatial multiplexing gain. However, the power consumption and inter-beam interference of a hybrid precoder increase as the number of beams grows [77]. Therefore, optimizing the hardware and system complexity of a large mmWave system is critical. As a result, various hybrid precoding designs to maximize sum rate while achieving a reduction in the number of RF units have been investigated. However, this digital-analog beamforming requires two-step NP-hard precoding, namely baseband and RF precoding leading to high computational complexities. In addition, the complexity of scheduling a large UE population increases with increasing number of RF chains at the gNB N_{RF}.

The literature on hybrid beamforming for multi-user case with $M \leq N_{RF}$ have mainly focused on using SDMA for multiplexing UEs with with the assumption of one UE per data stream generated from an RF unit. Further, orthogonality on data streams to UEs is obtained via joint RF and baseband precoding schemes based on channel information

and correlation. It is notable that, if two UEs are co-located then even with baseband precoding, multiplexing UEs over dominant eigenmodes, perfect orthogonality might not always be possible, resulting in inter-user interference (IUI). However, if the UEs are multiplexed over orthogonal subcarriers, IUI does not arise. Further, to boost the system capacity when UE population $M \gg N_{RF}$, the wideband mmWave channel can be used to schedule multiple UEs over a beam using OFDMA. To serve multiple UEs in OFDMA, authors in [22] used sparsity-based digital precoding to jointly estimate subcarrier and hybrid precoder design for a fully-connected hybrid architecture. However, even with weighted minimum mean squared error digital (MMSE) precoder in [22], achieving perfect orthogonality among the spatial streams of co-located UEs is not possible. Besides, with increasing UE population and antenna array size, the complexity of zero-forcing and MMSE precoders grow non-linearly. Moreover, zero-forcing and MMSE precoders are both constrained by the weakest UE SNR.

Additionally, the directional mmWaves communication has implications over the MAC layer as well. The mmWave communication systems can be deployed in two modes, namely, non-standalone (NSA) mode – where control signaling is provided by existing 4G nets, and standalone (SA) mode – where control signaling is also carried out at mmWave frequencies. Though much research has been reported on the NSA domain, the SA mode has received relatively much less attention. SA mode will help mmWaves to realize its full potential in terms of ultra-low latency and huge bandwidth. On the other hand, the SA mode has its own set of difficulties. One such challenge is to identify a suitable narrow beam pair between gNB and UE during the IA phase. According to 3GPP NR guidelines, for SA mode the communication at mmWaves is divided into two phases - beam training phase and data transmission phase [78].

The limitations of two-phase mmWave communication model are as follows. First, the bandwidth at mmWaves is enormous, whereas the initial access and other control data are very small. Moreover, the 3GPP NR considers a minimum TTI of one slot duration, or 7 OFDM symbols, for the eMBB application [57]. Therefore, if a sector has no user in a particular direction during the beam training phase, 7 OFDM signals are wasted. Second, the beam training and data transmission phases use different precoders leading to increased computational complexity at the gNB. During the beam training phase, the sectorization method is employed, whereas during the data transmission phase, the baseband and RF precoders are redesigned to service some dedicated directions having scheduled users. Third, 3GPP NR has suggested contention-free initial access for

standalone mmWave communications, which necessitates a second round of scanning to inform users of the location of a physical random access channel (PRACH) corresponding to a synchronization signal (SS) burst in each direction. To this end, beam training and data transmission phases and the related precoding designs have been studied, but the number of users served in an epoch was constrained to be less than or equal to the number of RF chains at the gNB. Also, the effect of non-homogeneous user distribution has not been taken into account to optimize spectral efficiency.

To this end, in Chapter 2 we observed that dedicating an RF unit along with the entire spectrum to a single UE at a time in a UMi environment is not advantageous from the spectral and energy efficiency perspective. Further, Chapter 2 investigated the optimum transmit beamwidth in a sectored-cell framework required to maximize system performance when an gNB has a single RF chain. Therefore, the analysis was devoid of inter-beam interference. Moreover, the variable time scheme in Chapter 2 considered sector sojourn time to be a continuous variable. As an extension, in this chapter, we investigate the inter-beam interference for different UE distributions using a sectored-cell approach with multiple RF units. To improve the achievable rate and fairness among non-homogeneously distributed UEs, the sector sojourn time is solved by formulated as an integer optimization problem. Further, the existing MAC layer protocols at mmWaves are not spectrally efficient in the IA phase. To this end, we propose the related MAC layer specifications that provide simultaneous IA to all the UEs within a sector. To the best of our knowledge, the proposed system model has not been studied in the literature yet.

3.1.1 Contribution

In this chapter we study the performance of the sectored-cell system model with multi-RF beams while accounting for the inter-beam interference and UE distribution dependent variable sector sojourn time, to cater to a large UE population. The performance metrics of the proposed system depend on the optimal number of sectors as well as on selection of the optimal number of concurrently active beams. To the best of our knowledge, the proposed system model has not been studied in the literature yet. The key contributions are:

a) A novel sectored-cell system model is presented using a multi-RF beamforming structure to serve the UEs in the urban micro (UMi) scenario at mmWave frequency. Each RF unit is connected to a array of an optimal size capable of forming narrow

steerable beams over the sectors. Each beam supports multiple UEs per sector at a time. At the baseband level, algorithms are proposed to optimally allocate OFDM resources to the UEs to minimize inter-beam interference while maximizing throughput. Further, the two schemes namely, synchronous and asynchronous sweeping of cell by the beams are investigated.

b) A variable time frame structure is proposed for the sectored-cell model. It aims to reduce IA delay and achieves better spectral efficiency compared to exhaustive search IA procedure proposed by 3GPP NR for cellular mmWave communications.

c) For a given gNB power budget and a large number of homogeneously distributed UEs in the cell, a joint optimization problem is formulated to find the optimum sector beamwidth and an optimum number of concurrent beams that maximize the average long-run UE rate in presence of side-lobe interference using realistic ULA gain pattern. Also, the comparison of user scheduling complexity of the proposed system is provided over the existing competitive scheduling models in the literature.

d) For non-homogeneous UE distribution, sector sojourn time is optimized by availing the advantages of variable time frame structure using weighted round-robin (WRR) scheduling to improve the fairness of long-run UE rates.

3.1.2 Chapter Organization

The chapter organization is as follows. System model is presented in Section 3.2. The variable time frame structure is presented in Section 3.3. Resource allocation strategy, optimum sector beamwidth, number of RF units, and sector sojourn time are analyzed in Section 3.4. Complexity analysis is presented in Section 3.5, simulation results are discussed in Section 3.6, and chapter is summarized in Section 3.7.

3.2 System Model

In this section, we describe the cell architecture and the antenna configuration at the gNB to support the directional communication at the mmWave in the UMi environment, with the number of RF chains $N_{RF} \ll M$, where M is the number of UEs independently distributed in the cell. The cell is partitioned into S identical sectors. We also propose

an underlying variable time MAC layer protocol to support the proposed sectored-cell time-multiplexed model in section 3.3.

Let $\mathcal{S}$ be the set containing all possible values of S that a cell can be sectorized into, i.e., $\mathcal{S} = \{S|S = \lceil \frac{2\pi}{\Theta} \rceil, \Theta_{min} \leq \Theta \leq \Theta_{max}\}$, where $[\Theta_{min}$ and $\Theta_{max}]$ denotes the range of supportable sector width or equivalently half power beamwidth (HPBW) of the serving beam. For a particular sectorization scheme S, let s denote the index of a sector, $s = \{1, \cdots, S\}$. Also, let K_s be the number of UEs located in sth sector of a sectorization scheme S such that $\sum_{s \in S} K_s = M$.

3.2.1 UE Deployment

In this chapter we study the performance in context to both homogeneous and non-homogeneous UE deployment. We use the same model as given in Section 2.2 for homogeneous UE setup, i.e., the probability of a UE falling in a sector s is $\mathcal{Q}(s) = 1/S$. To generate a non-homogeneous UE distribution, we employ a more sophisticated technique, as discussed next. A cell is divided cell into Z zones. Each zone has a granularity of $\delta\phi$. The probability of a UE falling in the angular area $ar(\hat{\phi})$ varies with $\hat{\phi}$, where $\hat{\phi}$ is the angular distance. Then, $\mathcal{Q}(ar(\hat{\phi}))$ is calculated as

$$\mathcal{Q}(ar(\hat{\phi})) = \frac{\exp(\Upsilon \lfloor \text{mod}(\hat{\phi}, 360^o/Z)/\delta\phi \rfloor \delta\phi)}{Z \sum_{i=0}^{(360^o/Z\delta\phi)-1} \exp(\Upsilon i \delta\phi)} \tag{3.1}$$

where Υ decides the intensity of non-homogeneity. The proof of $\int_{\hat{\phi}} \mathcal{Q}(ar(\hat{\phi}))d\hat{\phi} = 1$ is given in Appendix A. The distribution given by (3.1) is used in Section 3.6.3 for simulation studies.

3.2.2 Spatial Multiplexing with $\mathbf{N_{RF}}$ Beams

Spatial multiplexing is accomplished at the gNB by scanning the 2π angular space with N_{RF} RF chains that concurrently serve UEs located in N_{RF} out of S sectors in an epoch (Fig. 3.1 (a) and (b)). We assume that S is a multiple of N_{RF}. Each RF unit is connected to a separate array of N_t antenna elements. Each beam serves all the UEs in a sector using OFDMA at a time. Thus, the N_{RF} beams serve the sectors in a fashion such that each beam steers over a set of S/N_{RF} consecutive sectors in a cell sweep. Let s_j denote sth sector served by jth beam in an epoch. Then, $\mathcal{S}_b = \{s_b|s$ sectors served by the bth beam$\}$, where $b = 1, \cdots, N_{RF}$. Further, we assume that each UE has a single RF unit

connected to array of N_r antenna elements. For analytical simplicity, we consider fixed beamforming gain $G_r = N_r$ at the receiver irrespective of the steering directions, and let number of steerable directions at UE be S_r, as shown in Fig. 3.1 (c).

3.2.3 Wideband mmWave Channel Model

At mmWave frequencies there exists either a line-of-sight (LOS) link or non-line-of-sight (NLOS) link between UE and gNB due to large difference in attenuation of first order and higher order signals. The probability of a link being in LOS for kth UE at distance d_k from gNB is expressed as $\Pr(d_k) = \min(d_1/d_k, 1)(1 - e^{-d_k/d_2}) + e^{-d_k/d_2}$, where $d_1 = 18$ and $d_2 = 36$ [79]. Additionally, the path loss for LOS and NLOS link are obtained as [65]

$$\begin{aligned} \text{PL}_{LOS}(d_k) &= 61.4 + 20\log_{10}(d_k) + \mathcal{N}(0, 33.64) \text{ [dB]} \\ \text{PL}_{NLOS}(d_k) &= 72.0 + 29.2\log_{10}(d_k) + \mathcal{N}(0, 75.69) \text{ [dB]}. \end{aligned} \tag{3.2}$$

Therefore, for the kth UE, at a distance d_k from gNB the pathloss PL_k is expressed as

$$\text{PL}_k = \begin{cases} \Pr(d_k) 10^{\text{PL}_{LOS}(d_k)/10}, & \text{LOS} \\ (1 - \Pr(d_k)) 10^{\text{PL}_{NLOS}(d_k)/10}, & \text{NLOS}. \end{cases} \tag{3.3}$$

The channel between gNB and kth UE exhibit frequency-selective fading; the total available bandwidth B is divided into N_c subcarriers, with f_c being the carrier frequency.

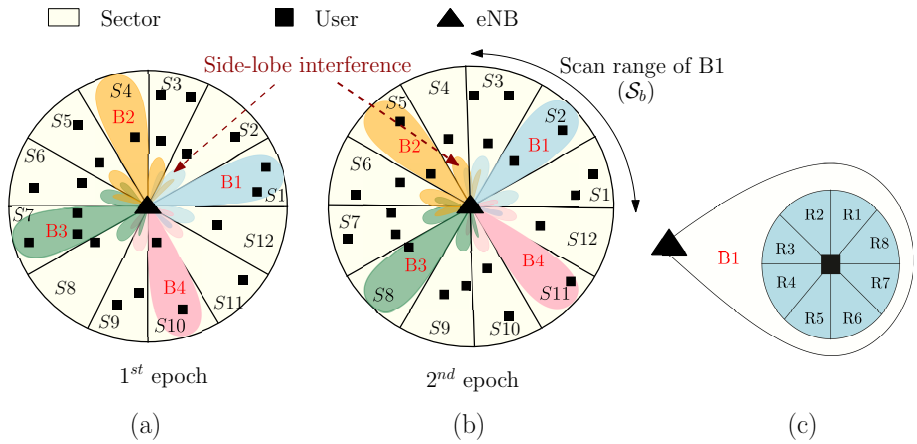

Figure 3.1: (a) and (b) depicts round-robin scheduling of sectors over two consecutive epochs with $S = 12$ sectors and $N_{RF} = 4$ beams, represented as $\{S1, \cdots, S12\}$ and $\{B1, \cdots, B4\}$, respectively. Here, $\mathcal{S}_{b=B1} = \{S1, S2, S3\}$; and (c) shows steering directions $\{R1, \cdots, R8\}$ of a UE within beam B1, i.e., $S_r = 8$.

Further, the channel consists of $L_k \ll N_t$ multipath components (MPCs) [14]. Thus, the channel between gNB and kth UE over nth subcarrier (frequency f_n) as seen by a single RF unit connected to N_t active antenna elements is expressed as

$$\mathbf{h}_{k,n} = \sqrt{\frac{N_t}{L_k \mathrm{PL}_k}} \sum_{l=1}^{L_k} \alpha_{k,n,l} \mathbf{a}_{\mathbf{T}}(\Omega(f_n), \phi_{k,l})^H \in \mathbb{C}^{1 \times N_t} \tag{3.4}$$

where $\alpha_{k,n,l}$ is small scale fading of lth MPC over nth subcarrier, and $\phi_{k,l}$ is the AoD of lth MPC assumed uniformly distributed with angular spread of σ_T^{AS}. Then, the gNB array response vector $\mathbf{a}_{\mathbf{T}}(\Omega(f_n), \phi_{k,l})$ at an offset angle $\phi_{k,l}$ is

$$\mathbf{a}_{\mathbf{T}}(\Omega(f), \phi_{k,l}) = \frac{1}{\sqrt{N_t}} \left[1, e^{-j\frac{2\pi}{\lambda_c} d' \Omega(f) \sin\phi_{k,l}} \ldots, e^{-j\frac{2\pi}{\lambda_c} d' \Omega(f)(N_t-1)\sin\phi_{k,l}}\right]^T \tag{3.5}$$

Here, $\Omega(f) = (1 + f/f_c)$ is the beam squint parameter at frequency f [42], d' is the inter element ULA spacing, and λ_c is the carrier wavelength. The information of channel paramters $(L_k, \alpha_{k,l}, \phi_{k,l}, d_k)\ \forall k$ is available at the gNB from the IA phase assuming zero estimation error.

Furthermore, the transmit power per RF chain P_t with the constraint on maximum EIRP value is given by (2.1).

3.2.4 Effective Rate in Presence of Side-lobe Interference

In an epoch out of total S sectors only N_{RF} sectors will be served simultaneously. So, with the consideration of practical beam radiation pattern with side-lobes at gNB, the UEs in s_bth sector served by bth beam in an epoch, where $b = \{1, 2, \cdots, N_{RF}\}$, will experience side-lobe interference from the rest of the beams $\hat{b} \neq b$. Also, at gNB let $\mathbf{A}$ be the wideband analog beamforming vector of a beam b, steered at offset angle Φ_b to serve sth sector, given as

$$\mathbf{A}(\Phi_b) = \frac{1}{\sqrt{N_t}} \left[1, e^{-j\frac{2\pi}{\lambda_c} d' \sin\Phi_b} \cdots, e^{-j\frac{2\pi}{\lambda_c} d'(N_t-1)\sin\Phi_b}\right]^T. \tag{3.6}$$

In a sectorized cell with total S number of sectors, the possible steering directions are fixed at $\Phi_b = (t + b - 2)(360^o/S)$, where $t = 1, \cdots, \lceil S/N_{RF} \rceil$ denotes the epoch index during a cell sweep. Consequently, the signal-to-interference-plus-noise ratio $\Gamma_{k,n}^{s_b}$ of kth UE at distance d_k from gNB, over the nth subcarrier in sector s_b served by beam b is

$$\Gamma_{k,n}^{s_b} = \frac{P_{k,n}^{s_b} |\mathbf{h}_{k,n}^{s_b} \mathbf{A}(\Phi_b)|^2 G_r}{\frac{N_0 B}{N_c} + \sum_{j=1, j\neq b}^{N_{RF}} P_{k,n}^{s_j} G_r |\mathbf{h}_{k,n}^{s_b}{}^H \mathbf{A}(\Phi_j)^H \mathbf{A}(\Phi_j) \mathbf{h}_{k,n}^{s_b}|} = P_{k,n}^{s_b} \gamma_{k,n}^{s_b} \tag{3.7}$$

Table 3.1: Power consumption of components in a RF chain

Component	Notation	Power consumption
DAC	P_{DAC}	Given by (3.8)
Low-pass filter	P_{LPF}	14 mW
Mixer	P_M	0.3 mW
Phase-shifter	P_{PS}	$\approx$ 0 mW
Local oscillator	P_{LO}	22.5 mW
Power amplifiers	P_{PA}	$P_t/\eta_{PA}, \eta_{PA} = 27\%$

where N_0 is the noise spectral density, and $P_{k,n}^{s_j}$ and $\mathbf{h}_{k,n}^{s_j}$ are the power allocation and channel vector of kth UE over nth subcarrier, respectively, in s_jth sector served by jth beam. Thus, data rate of kth UE over the nth subcarrier in s_bth sector in an epoch is $r_{k,n}^{s_b} = (B/N_c)\log_2(1 + \Gamma_{k,n}^{s_b})$.

3.2.5 RF Chain Power Consumption

At mmWaves, the power dissipation in RF circuitry is also a significant part of the total gNB power budget. The power consumption values and quantities of all the components in an RF front-end are listed in Table 3.1 [80]. Since the power consumption of passive phase-shifter is negligible, the total power consumption per RF chain, having a separate I/Q module, is $P_{rf}(P_t) = 2P_{DAC} + 2P_M + 2P_{LPF} + P_{LO} + P_{PA}$. Here, P_{PA} depends on transmit power P_t and power amplifier's efficiency η_{PA}. P_{DAC} depends on the sampling frequency F_s and number of bits b_t as

$$P_{DAC} = 1.5 \times 10^{-5} \cdot 2^{b_t} + 9 \times 10^{-12} \cdot b_t \cdot F_s. \tag{3.8}$$

An gNB employing N_{RF} number of RF chains will have a single local oscillator shared among all the chains. Therefore, total power consumption of RF front-end at gNB is

$$P_{nrf}(N_{RF}, P_t) = N_{RF}(2P_{DAC} + 2P_M + 2P_{LPF} + (1 - \eta_{PA})P_t/\eta_{PA}) + P_{LO}. \tag{3.9}$$

Remark 3.1. *The primary power-hungry component in an RF chain is the power amplifier. The energy consumption of a power amplifier depends on the transmitted power P_t as well (as listed in Table 3.1). Therefore, for a given value of N_{RF}, decreasing beamwidth will decrease the transmit power requirement, and hence it will reduce the resulting power waste in power amplifiers.*

3.3 Proposed Variable Time Frame Structure

In this section, we propose a variable time frame structure that offers greater flexibility for control signaling and sector scheduling by a beam. The proposed frame structure has smaller IA delay and control overhead compared to the IA procedure proposed in 3GPP NR [81].

Consider two states of UE operation: idle state and connected state. In an idle state, a UE does not communicate with gNB and only passively monitor gNB's paging and broadcast information to maintain connectivity with the network. The UE transits from idle to connected state after the initial handshake procedure. The proposed sectored-cell system model uses N_{RF} concurrent beams for spatial multiplexing and each spatially distributed beam serves only a subset of $\mathcal{S}_b$ sectors, as shown in Fig. 3.1(a). Therefore, in the following section, we consider the case of a single analog beam covering $\mathcal{S}_b$ sectors in a round-robin fashion in a single cell sweep. Furthermore, each UE has a single RF chain connected to a ULA capable of forming narrow beam steerable in S_r directions, as stated in section model Section II. The same procedure occurs independently with the rest of the concurrently active analog beams, achieving full spatial multiplexing.

3.3.1 3GPP NR IA Procedure

The smallest 3GPP 5G NR frame is equal to one slot duration which is also equal to its TTI. A TTI is a set of OFDM symbols that constitutes the smallest decodable transmission unit. Each slot can carry a maximum of 2 synchronization signal (SS) blocks that are used for beam training and control information broadcast. Each SS block comprises of 4 consecutive OFDM symbols over a set of 240 subcarriers [82]. The IA steps of a new UE during the beam management as in 3GPP NR Release 15 are shown in Fig. 3.2(a).

The IA procedure of 3GPP NR is as follows [52]. First, the beam sequentially scans all of the $\mathcal{S}_b$ sectors and transmits SS blocks corresponding to each gNB-UE beam pair directions, i.e., totaling $|\mathcal{S}_b|S_r$ directions. Based on maximum SNR, the new UE selects the best beam and decodes the corresponding SS block while the connected UEs perform beam tracking and paging in the rest of the control portion. The UE obtains essential system information by decoding primary synchronization signals, secondary synchronization signals, and physical broadcast control channel after acquiring SS blocks. The UE then connects to the network using a physical random access channel (PRACH) to send random access (RACH) preambles in the UL slot [81]. RACH preamble from a UE informs

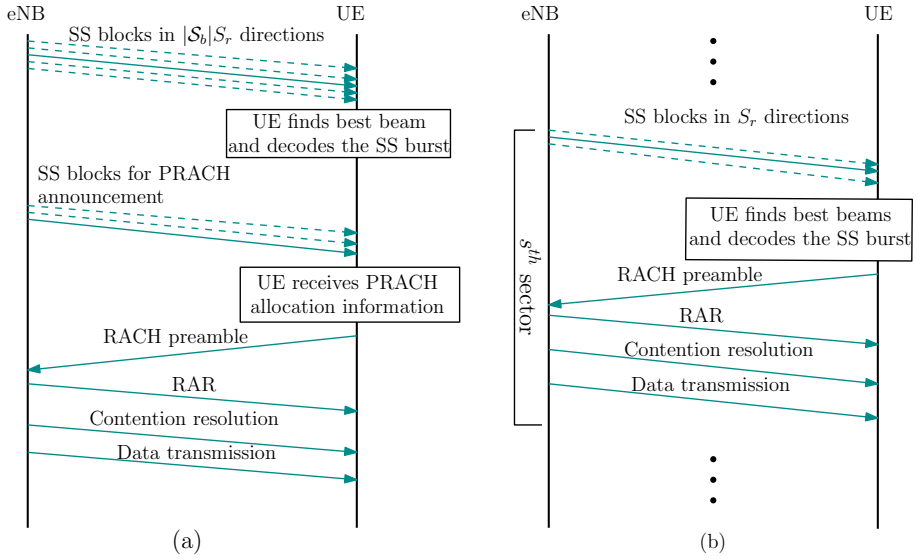

Figure 3.2: (a) Steps in IA for new UEs using 3GPP NR guidelines (b) Steps in IA for news UEs according to proposed frame structure for directional cellular communication.

the gNB about its channel and beam conditions. In standalone mmWave, an extra round of sequential scan over $\mathcal{S}_b$ is performed to notify UEs about the unique time-frequency offset of PRACH corresponding to each SS block transmitted in all gNB-UE pair directions for best beam estimation. It allows UEs to know when and where to transmit their RACH preamble for contention-free access, thus extending the IA.

3.3.2 Proposed IA procedure

We perform beam training and data transmission simultaneously within a frame using the proposed frame structure, leveraging the sectored-cell model. Some resources in the frame are set aside for IA of new UEs, while the remaining ones are used for data transmission with connected UEs. Therefore, jointly with variable time structure of the frame and combined beam training and data transmission phase, the mmWave bandwidth is efficiently utilized.

In the proposed variable time frame structure we assume a superframe of duration T_{tot}. The superframe is composed of frames transmitted by the beam in all the sectors $s \in \mathcal{S}_b$ in a single cell sweep. There are no fixed frame boundaries, i.e., each frame in a sector can have a different number of OFDM symbols instead of a fixed duration of 14 OFDM symbols as in 3GPP NR. Further, as explained above, the beam management of new UEs and exchange of data with multiple connected UEs occur simultaneously using

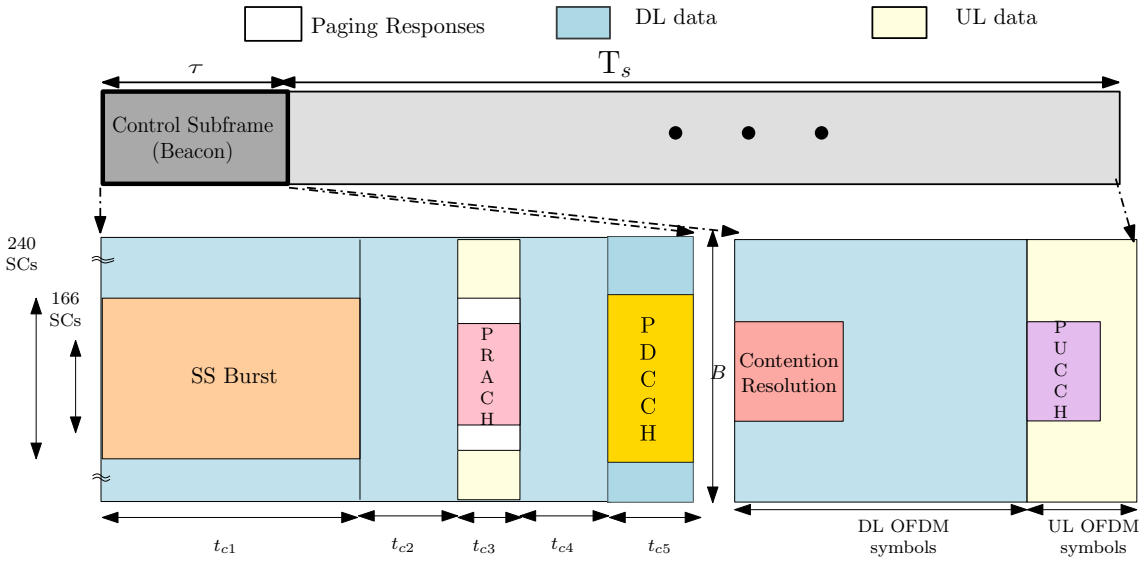

Figure 3.3: Schematic diagram of the proposed frame structure, transmitted in sth sector, depicting the position of control channels required for IA in τ duration, and control channels required for contention resolution and UE beam refinement in T duration.

OFDMA in the control portion of the frame. Subsequently, we consider that the frame in a sector $s \in \mathcal{S}_b$ consists of a control subframe (beacon) of duration τ plus a subframe of variable duration T_s, as shown in Fig. 3.3, such that $\sum_{s\in\mathcal{S}_b}(\tau + T_s) = T_{tot}$. The beacon duration τ is the same for all sectors. The paging queries for the connected UEs are included in the SS burst while the paging responses by the UEs are transmitted over separate UL channels. Fig. 3.2(b) depicts the steps required in IA procedure. For brevity, we describe only the modified channels, while keeping the functionality of other channels same. Furthermore, different TTI duration can be defined using the different number of OFDM symbols. In the proposed frame structure we set the minimum TTI possible equal to one OFDM symbol. Hence, the UEs can capture and decode the information of one TTI without waiting for the entire frame to end.

The IA using the proposed variable time frame structure is explained as follows. As the beam b enters a sector s_b, it broadcasts SS blocks in the first $4S_r$ OFDM symbols for the duration t_{c1} of the control subframe, allowing new UEs to search for the SS block in each of its S_r directions and decode the one with the strongest signal. Moreover, with the proposed system the likelihood of RACH collision from multiple new UEs in a sector is negligible.

Lemma 1: When N_{RF} is sufficiently high, the probability of two or more UEs trans-

mitting the same RACH preamble over PRACH in a single frame is very small.

Proof: See Appendix B.

Consequently, multiple time-frequency resources corresponding to different S_r directions are not set aside in PRACH, thereby saving bandwidth. Then the new UEs transmit orthogonal RACH preambles over a single set of reserved time-frequency resources assigned for PRACH in the next TTI of 1 OFDM symbol duration (t_{c3} duration) in UL after waiting for t_{c2} duration. The RACH also contains the information of the UEs' best link and channel information. If there is contention because of two or more UEs using the same preamble over the same time-frequency grid, gNB is still able to detect the presence of contending UEs. The gNB decodes RACH preambles to access UEs beam conditions, namely, gain, steering direction, etc., and accordingly finds the optimum resource allocation strategy. After waiting for t_{c4} duration, gNB grants UEs the random access response (RAR) over the next TTI consisting of 2 OFDM symbols (t_{c5} duration) in the common physical DL control channel (PDCCH). The transmission of RAR to a UE indicates that the gNB has correctly obtained and decoded the RACH preamble, allowing the UE to access the channel. The UE can now access the channel immediately after τ duration. As a result, the complete IA of all the UEs located in a sector can be carried out within the sector sojourn time. Here, t_{c2} and t_{c4} are the time offset to allow for transmission and processing delay. The remaining resources in τ duration are used for data transmission to connected UEs in DL/UL. If in sth sector $K_s = 0$ then gNB does not detect any paging responses and RACH preambles, the frame is of duration τ only. The duration T_s is dedicated for data portion, which can be optimized to the granularity of OFDM symbol to improve UEs' fairness, as discussed later in Section 3.4.3. In addition, as shown in Fig. 3.3, DL and UL assignment in a frame is flexible, and some subcarriers are reserved for contention resolution in PDCCH and physical UL control channel DL (PUCCH) in T_s duration.

3.3.3 Performance Metrics

3.3.3.1 IA Delay

In directional communication, IA delay (IAD) is defined as the time required by a new UE to transit into the connected state after it first listens to the synchronization signals. According to the methodology defined by 3GPP NR, the IA procedure takes place by scanning all the $\mathcal{S}_b$ sectors sequentially for SS burst and then reception of RACH in $\mathcal{S}_b$

sequentially before sending RAR to all the new UEs. Also, 3GPP NR defines TTI size equal to one slot and supports a maximum of two SS blocks per slot [81]. Thus, the total time required is summation of $(|\mathcal{S}_b|S_r)/2 \times 14T_{OFDM}$ for SS block transmission, $|\mathcal{S}_b| \times 14T_{OFDM}$ for PRACH announcement, $|\mathcal{S}_b| \times 14T_{OFDM}$ for RACH transmission, and $|\mathcal{S}_b| \times 14T_{OFDM}$ for RAR. Therefore, minimum IAD of IA procedure defined in 3GPP NR is, $\text{IAD}^{3GPP} = |\mathcal{S}_b| \cdot 14 \cdot (S_r/2+3)T_{OFDM}$. On contrary, the proposed variable time frame structure allows for the IA to be carried out sector by sector. Therefore, compared to the 3GPP NR, minimum IAD of the proposed scheme is equal to the beacon subframe time, i.e., $\text{IAD}^{Prop} = (4 \cdot S_r + 3)T_{OFDM} + t_{c2} + t_{c4} = \tau$. Thus, the percentage improvement in IAD with the proposed variable time frame structure is

$$\Delta \text{ IAD} = \left(1 - \frac{\tau}{|\mathcal{S}_b| \cdot 14 \cdot (S_r/2+3)T_{OFDM}}\right) \times 100. \tag{3.10}$$

3.3.3.2 Bandwidth Savings

From Lemma 1 we know that, unlike the IA methodology in 3GPP NR, in proposed IA procedure there is no need to reserve different resource elements for different UEs over the bandwidth for RACH reception, thereby saving bandwidth. Consequently, the proposed IA method does not need an additional round of SS blocks transmission for RACH resource announcement in $\mathcal{S}_b$ directions. SS block uses 240 subcarriers over 4 OFDM symbols, RACH preamble occupies 166 subcarriers, and RAR transmitted on PDCCH consumes a maximum of 240 subcarriers [57]. Hence, the total bandwidth consumed in overhead for the IA procedure using 3GPP NR specifications (assuming no contention) is

$$\begin{aligned}\text{BW}^{3GPP} =& \Delta f \cdot \text{REs in (SS blocks + RACH resources announcement} \\ &+ \text{RACH preambles + RAR)} \\ =& \Delta f \cdot (240 \cdot 4 \cdot |\mathcal{S}_b| \cdot S_r \cdot N_{rep} + 240 \cdot 4 \cdot |\mathcal{S}_b| + 166 \cdot |\mathcal{S}_b| + 240 \cdot 2 \cdot |\mathcal{S}_b|)\end{aligned} \tag{3.11}$$

where RE is the resource element (smallest time-frequency element), Δf is the subcarrier spacing and N_{rep} is total number of SS blocks transmitted over bandwidth B per gNB-UE beam pair. The total bandwidth required in IA procedure using proposed frame structure is

$$\begin{aligned}\text{BW}^{Prop} =& \Delta f \cdot \text{REs in (SS blocks + RACH preambles + RAR)} \\ =& \Delta f \cdot (240 \cdot 4 \cdot |\mathcal{S}_b| \cdot S_r + 166 \cdot |\mathcal{S}_b| + 240 \cdot 2 \cdot |\mathcal{S}_b|).\end{aligned} \tag{3.12}$$

Thus, percentage bandwidth savings with proposed frame is

$$\Delta \text{ BW} = \frac{480 \cdot (S_r \cdot N_{rep} - S_r + 1)}{480 \cdot S_r \cdot N_{rep} + 803} \times 100. \tag{3.13}$$

3.4 Problem Formulation and Performance Evaluation

In this section, we evaluate the performance of the proposed system with the underlying protocol as presented in Section 3.3 in terms of average long-run UE rate, power budget, and fairness for homogeneously distributed UEs. The analysis is further extended to find the optimal sector sojourn time in case of non-homogeneous UE distribution for a given S^* and N^*_{RF} that optimizes system performance.

For simplicity, we assume the same DL and UL data capacities and calculate the total data rate supported over the bandwidth. We also assume quasi-static channel during a cell sweep. Let N_{c1} and N_{c2} be the number of effective subcarriers available for data transmission during τ and T_s interval, respectively. We define the long-run UE rate as the total data received by a UE over one cell sweep duration T_{tot}. Therefore, the long-run rate of kth UE located in sth sector is

$$R^s_k = \frac{\tau_s \sum_{n=1}^{N_{c1}} \pi^{s,\tau_s}_{k,n} r^{s,\tau_s}_{k,n} + T_s \sum_{n=1}^{N_{c2}} \pi^{s,T_s}_{k,n} r^{s,T_s}_{k,n}}{T_{tot}} \tag{3.14}$$

where τ_s and T_s are the control subframe and variable subframe duration of sth sector. Also, $\tau_s = \tau \; \forall s$. The variables $\pi^{s,\tau}_{k,n}$ and $\pi^{s,T_s}_{k,n}$ denote the subcarrier assignment in OFDM symbols during τ and T_s, respectively. The value of $\pi^{s,\tau/T_s}_{k,n} = 1$ denotes the assignment of nth subcarrier to kth UE is sth sector during τ or T_s. Similarly, we define the average long-run UE rate $\bar{R}$ as the average of long-run rate of all UEs and it is equivalent to

$$\bar{R} = \frac{\sum_{s=1}^{S} \sum_{k=1}^{K_s} R^s_k}{M} = \frac{1}{MT_{tot}} \sum_{s=1}^{S} \left(\tau \sum_{k=1}^{K_s} \sum_{n=1}^{N_{c1}} \pi^{s,\tau}_{k,n} r^{s,\tau}_{k,n} + T_s \sum_{k=1}^{K_s} \sum_{n=1}^{N_{c2}} \pi^{s,T_s}_{k,n} r^{s,T_s}_{k,n} \right). \tag{3.15}$$

In hybrid beamforming, the system hardware power consumption at gNB is also a significant parameter. Total power consumption at gNB includes total power dissipated predominantly in RF hardware circuitry and total power consumed in the transmission of bits. However, the system performances are constrained by the peak power expressed as

$$P_{peak}(S, N_{RF}) = \sum_{s \in \mathcal{S}_i} \sum_{k=1}^{K_s} \sum_{n=1}^{N_c} P^s_{k,n} + P_{nrf}(N_{RF}, P_t) \tag{3.16}$$

where $P_{nrf}(\cdot)$ is the power consumed at transmitter and $\mathcal{S}_i = \{s|\text{sectors concurrently served by } N_{RF} \text{ beams during the } i\text{th epoch}\}$. Another important parameter is the system fairness. In this chapter, we use the geometric mean of long-run UE rate to to characterize fairness of long-run UE rates given as

$$\bar{G} = \sqrt[M]{\Pi_{s=1}^{S} \Pi_{k=1}^{K_s} R_k^s}. \tag{3.17}$$

3.4.1 Resource Allocation and Cell Sweeping Schemes

We first discuss the problem of resource allocation in a sector, at a given time, implemented at baseband level of each RF unit. Here we have dropped the superscript τ/T_s for notation simplicity. To achieve a trade-off between system throughput and UE fairness within a sector at a time, we use proportional fairness (PF) subcarrier allocation scheme. Accordingly, the optimization problem for resource allocation in sth active sector in an epoch is formulated as

$$\begin{aligned} (\mathcal{P}0): \quad & \max_{\pi_{k,n}^s, P_{k,n}^s} \sum_{k=1}^{K_s} \ln\left(\sum_{n=1}^{N_c} \pi_{k,n}^s r_{k,n}^s\right) \\ \text{s.t.} \quad & C01: \sum_{k=1}^{K_s} \pi_{k,n}^s \leq 1,\ \forall n;\ C02: \pi_{k,n}^s \in \{0,1\} \\ & C03: P_{k,n}^s \geq 0,\ \forall k,n,s;\ C04: \sum_{k}\sum_{n} P_{k,n}^s \leq P_t,\ \forall s. \end{aligned} \tag{3.18}$$

Here, $\pi_{k,n}^s$ and $P_{k,n}^s$ are obtained by joint iteration and the complexity of such iterative method is very high to adopt in practical applications [83]. Therefore, we use a heuristic subcarrier and power allocation approach as discussed next.

3.4.1.1 Subcarrier and Power Optimization

In this approach we find the optimal ${\pi_{k,n}^s}^*$ and ${P_{k,n}^s}^*$ using the fact that system performance evaluation in our work is a relative analysis of rates over all the sectors. To ensure proportional fairness condition the optimization problem for subcarrier allocation in sth sector served during an epoch is formulated as

$$\begin{aligned} (\mathcal{P}1): \quad & \max_{\pi_{k,n}^s} \sum_{k=1}^{K_s} \ln\left(\sum_{n=1}^{N_c} \pi_{k,n}^s r_{k,n}^s\right) \\ \text{s.t.} \quad & C11: \sum_{k=1}^{K_s} \pi_{k,n}^s \leq 1,\ \forall n;\ C12: \pi_{k,n}^s \in \{0,1\},\ \forall k,n \end{aligned} \tag{3.19}$$

We relax $\pi_{k,n}^s$ to a real number in the interval $[0,1]$. Thus, Lagrangian formulation of $\mathcal{P}2$ is

$$\mathcal{L}(\pi_{k,n}^s, P_{k,n}^s, \boldsymbol{\lambda}) = \sum_{k=1}^{K_s} \ln\left(\sum_{n=1}^{N_c} \pi_{k,n}^s r_{k,n}^s\right) - \sum_{n=1}^{N_c} \lambda_n \left(\sum_{k=1}^{K_s} \pi_{k,n}^s - 1\right) \tag{3.20}$$

where $\boldsymbol{\lambda} = [\lambda_1, \cdots, \lambda_n]$ is the non-negative Lagrangian multiplier for constraint $C11$. By KKT condition we have

$$\frac{\partial \mathcal{L}(\pi_{k,n}^s, \boldsymbol{\lambda}, \eta)}{\partial \pi_{k,n}^s} = \frac{r_{k,n}^s}{\sum_{n=1}^{N_c} \pi_{k,n}^s r_{k,n}^s} - \lambda_n \leq 0 \tag{3.21}$$

Denote $R_k^s = \sum_{n=1}^{N_c} \pi_{k,n}^s r_{k,n}^s$. In (3.21), if the nth subcarrier is not allocated to kth UE then $\pi_{k,n}^s = 0, r_{k,n}^s = 0$ and $r_{k,n}^s/R_k^s - \lambda_n \leq 0$. On the other hand, if the nth subcarrier is allocated to kth UE then $\pi_{k,n}^s = 1, r_{k,n}^s \neq 0$, and $r_{k,n}^s/R_k^s - \lambda_n > 0$. This implies that nth subcarrier is allocated to kth user by the following rule

$$k^* = \arg\max_k \frac{r_{k,n}^s}{R_k^s}. \tag{3.22}$$

To satisfy the constraint $C12$, λ_n is set between $r_{k,n}^s/R_k^s$ and one. Next, each UE is given a share of power equal to the number of subcarriers allocated to it. Thus, the optimization problem for power allocation for kth UE is formulated as

$$\begin{aligned} (\mathcal{P}2): \quad & \max_{P_{k,n}^s} \sum_{n\in\omega_k} r_{k,n}^s \\ \text{s.t.} \quad & C21: P_{k,n}^s \geq 0,\ \forall k,n;\ C22: \sum_{n\in\omega_k} P_{k,n}^s \leq P_t|\omega_k|/N_c,\ \forall k \end{aligned} \tag{3.23}$$

where ω_k is the set of subcarriers allocated to kth UE. The Lagrangian of $\mathcal{P}3$ is formulated as

$$\mathcal{L}(P_{k,n}^s, \eta_k) = \sum_{n\in\omega_k} r_{k,n}^s - \eta_k \sum_{n\in\omega_k} \left(P_{k,n}^s - P_t|\omega_k|/N_c\right) \tag{3.24}$$

where η_k is the Lagrangian multiplier corresponding to $C22$. (3.24) is concave in $P_{k,n}^s$. Hence, from KKT conditions we have

$$\begin{aligned} {P_{k,n}^s}^* &= \left[\frac{(B/N_c)\pi_{k,n}^{s\,*}}{\ln 2 \eta_k^*} - \frac{1}{\gamma_{k,n}^s}\right]^+ \\ \eta_k^{(j+1)} &= \left[\eta_k^{(j)} - \hat{\epsilon}^{(j)}\left(\frac{P_t|\omega_k|}{N_c} - \sum_{n\in\omega_k} {P_{k,n}^s}^*\right)\right]^+. \end{aligned} \tag{3.25}$$

Algorithm 3.1 Proportional subcarrier and power allocation per sector

Input: $\gamma_{k,n}^s, K_s$
Output: $\{\pi_{k,n}^s{}^*\}, \{P_{k,n}^s{}^*\}$
Initialize $\omega_k = 0$ and $R_k^s = 0\ \forall k$
for subcarriers $n = 1$ to N_c **do**
    for users $k = 1$ to K_s **do**
        Set $\pi_{k,n}^s = 1$ and $\pi_{l,n}^s = 0$ for $l \neq k$
        Update ω_k and find $\{P_{k,n}^s{}^*\}$ using (3.25)
        Update $\{r_{k,n}^s\}$ and $R_k^{s\prime} = R_k^s + r_{k,n}^s$
    end for
    Find k^* with $R_k^s \leftarrow R_k^{s\prime}$ in (3.22)
    Update $\pi_{k,n}^s{}^*$, $P_{k,n}^s{}^*$ and R_k^s
end for

Here, η_k^* is the optimal dual variable for power constraint, which is updated using sub-gradient method with step size $\hat{\epsilon}$. The steps to solve for $\{\pi_{k,n}^s{}^*\}$ and $\{P_{k,n}^s{}^*\}$ are presented in Algorithm 3.1. For nth subcarrier allocation, $\omega_k\ \forall k$ is calculated by assuming $\pi_{k,n}^s = 1\ \forall k$. Then $P_{k,n}^s$ and $r_{k,n}^s\ \forall k, n$ are found, and $R_k^s \leftarrow \sum_{n\in\omega_k} r_{k,n}^s$. Accordingly, optimal k^* is evaluated using (3.22). Thereafter $P_{k,n}^s$ and R_k^s are updated.

3.4.1.2 Cell sweeping schemes

In the proposed variable frame structure, if sth sector served by bth beam during ith epoch has $K_s = 0$ then the frame duration is τ, and if $K_s \neq 0$ then the frame duration is $\tau + T_s$. Further, since zero-forcing or MMSE precoder is not used at the baseband, another way to reduce inter-beam interference while increasing net throughput is to optimally allocate the subcarrier and power to the UEs in the concurrently active beams. Also, the inter-beam interference reduction is possible only when the beams move in synchronized manner. Hence, with N_{RF} concurrent beams, two cell sweeping schemes, namely, synchronous and asynchronous cell sweeping are possible.

During the ith epoch of synchronous cell sweep, the sojourn time of sectors served by the concurrent beams is the same, i.e., $t_s^i = \tau + T_s \triangleq \tau + T\ \forall s \in \mathcal{S}_i$, where $\mathcal{S}_i = \{s|\text{sectors concurrently served by } N_{RF} \text{ beams during the } i\text{th epoch}\}$. If the sth sector served by bth beam has $K_s = 0$, the beam b remains silent during t_s^i (that is, it does not transmit, saving power) while the other concurrently active beams service their respective sectors. Note

Algorithm 3.2 Resource allocation in synchronous cell sweep scheme

1: Input: S, N_{RF}, and total number of epochs I
2: Output: $\{\pi_{k,n}^{s}{}^{*}\}, \{P_{k,n}^{s}{}^{*}\}\ \forall k, n, s$
3: **for** epoch $= 1$ to I **do**
4: Find the set of active sectors $\mathcal{S}_i = \{\forall s_b | \text{sectors being served at } i\text{th epoch with } K_{s_b} > 0\}$
5: Initially assume zero inter-beam interference
6: **for** $s \in \mathcal{S}_i$ **do**
7: Find $\{\pi_{k,n}^{s}\}, \{P_{k,n}^{s}\}\ \forall n, k$ using Algorithm 3.1
8: **end for**
9: Update $\gamma_{k,n}^{s}\ \forall s \in \mathcal{S}_i$ according to (3.7) and $R_k^s\ \forall k$
10: Go to step 6 till $\sum_{s\in\mathcal{S}_i}\sum_{k=1}^{K_s} R_k^s$ converges
11: **end for**

that, sector sojourn time is not necessarily equal to frame duration. Using synchronous cell sweep, it is possible to achieve inter-beam interference reduction. On the other hand, in asynchronous cell sweep, each beam has the freedom to move independently over its set of sectors $\mathcal{S}_b$ without wasting time, i.e., beam $b' \neq b$ can move to another sector $s \in \mathcal{S}_{b'}$ while the beam b continues to serve its currently scheduled sector. Although by using asynchronous cell sweeping coordinated resource allocation over the concurrently active sectors is not possible, resources can be optimized per beam at a time to improve the beam throughput. This results in increased inter-beam interference compared to the synchronous cell sweeping scheme. Nevertheless, it facilitates in improving the fairness of long-run UE rates by optimizing the sector sojourn times. The steps for resource allocation in synchronous and asynchronous cell sweep schemes are presented in Algorithm 3.2 and 3.3, respectively. When even one of the N_{RF} beams steers, it is counted as a new epoch in the algorithms. Also, OFDM resource allocation is performed separately for τ and T duration of the frame consisting of N_{c1} and N_{c2} subcarriers, respectively.

Remark 3.2. *The optimal value of sector sojourn time t_s^i of sth sector served by bth beam during ith epoch, given total cell sweep time T_{tot}, for the two cell sweeping schemes are*

$$\begin{aligned} \textit{Synchronous: } t_s^i &= \tau + \left\lfloor \frac{T_{tot} - |\mathcal{S}_b|\tau}{T_{OFDM}|\mathcal{S}_b|} \right\rfloor T_{OFDM} \\ &= \tau + T\ \forall i, s, b \\ \textit{Asynchronous: } t_s^i &= \begin{cases} \tau, & K_s = 0, \\ \tau + T_s, & K_s \neq 0 \end{cases} \end{aligned} \tag{3.26}$$

Algorithm 3.3 Resource allocation in asynchronous cell sweep scheme

Input: S, N_{RF}, and total number of epochs I'
Output: $\{\pi^s_{k,n}{}^*\}, \{P^s_{k,n}{}^*\}\ \forall k, n, s$
Initialize the set of active sectors $\mathcal{S}_0 = \{\forall s_b | \text{sectors steered at } i\text{th epoch with } K_{s_b} > 0\} = \emptyset$
for $i = 1$ to I' **do**
    Initially assume zero inter-beam interference,
    Find $\mathcal{S}_i$ and the set of sectors steered $\mathcal{S}_i^{steer} = \{s \in \mathcal{S}_i | s \in \mathcal{S}_i / \mathcal{S}_{i-1}\}$
    for $s \in \mathcal{S}_i^{steer}$ **do**
        Find $\{\pi^s_{k,n}\}, \{P^s_{k,n}\}\ \forall n, k$ using Algorithm 3.1
        Update $\gamma^s_{k,n}\ \forall s \in \mathcal{S}_i^{steer}$ according to (3.7)
    end for
end for

where T_s is found to optimize system performance.

3.4.2 Joint Estimation of Number of Sectors and Concurrent Beams

This section specifies the problem formulation for joint estimation of the optimal number of concurrent beams N^*_{RF} and optimal number of sectors S^* (or sector beamwidth Θ^*) required for average long-run UE rate maximization for a given gNB power budget.

From (3.7) we observe that, on one hand increasing N_{RF} will increase side-lobes interference, thereby decreasing cell peak data rate of UE in an epoch, while on the other hand it increases sector sojourn time. Thus, we need to choose a suitable value of N_{RF} that maximizes the average long-run UE rate $\bar{R}$. Moreover, S also influences the amount of inter-beam interference and sector sojourn time. Further, (3.16) indicates that peak power is also a function of N_{RF} and S (since P_t is a function of S). Therefore, the optimization problem to estimate S^* and N^*_{RF} that achieves highest $\bar{R}$ for a given gNB power budget P_{budget} is formulated as

$$
\begin{aligned}
(\mathcal{P}3): \quad & \max_{\pi^s_{k,n}, P^s_{k,n}, S, N_{RF}} \bar{R}(\pi^s_{k,n}, P^s_{k,n}, S, N_{RF}) \\
\text{s.t.} \quad & C31: \sum_{k=1}^{K_s} \pi^s_{k,n} \leq 1,\ \forall n, s;\ C32: \pi^s_{k,n} \in \{0,1\},\ \forall k, n, s \\
& C33: \sum_{n=1}^{N_c} \sum_{k=1}^{K_s} P^s_{k,n} \leq P_t,\ \forall s;\ C34: P^s_{k,n} \geq 0,\ \forall k, n, s \\
& C35: S \in \mathcal{S};\ C36: S \geq N_{RF};\ C37: 0 \leq P_{peak} \leq P_{budget}.
\end{aligned}
\tag{3.27}
$$

However, $\mathcal{P}3$ is jointly non-convex in $(\pi^s_{k,n}, P^s_{k,n}, S, N_{RF})$ and is a NP-hard problem. Therefore, we decompose $\mathcal{P}3$ and decouple the optimal resource allocation of UEs in all the sectors and optimal (S^*, N^*_{RF}) search. Constraint $C36$ has a straightforward implication that the total number of beams cannot exceed the total number of sectors in the cell. It is notable that water filling allocates power over subcarriers so as to maximize sum rate. Consequently, the difference between the total available power P_t and total allocated power $\sum_{k=1}^{K_s}\sum_{n=1}^{N_c} P^s_{k,n}$ is nearly zero. As a result, from (3.16) we have $P_{peak} = N_{RF}P_t + P_{nrf}(N_{RF}, P_t)$ i.e., $C37$ is relaxed to $0 \leq N_{RF}P_t + P_{nrf}(N_{RF}, P_t) \leq P_{budget}$. Therefore, the feasible value of N_{RF} is limited by the available power budget P_{budget}, as shown in Fig. 3.4. Accordingly, we fix the value of N_{RF} and set S, and find the corresponding transmit power P_t given by (2.1). Thereafter, we use Algorithm 3.2 or 3.3 for resource allocation in all the epochs. $\bar{R}$ is computed by substituting value of t^i_s in (3.15) as specified in Remark 3.2. The steps of the algorithm are repeated by incrementing N_{RF} to search for S^* while satisfying $C35$ and $C36$.

3.4.3 Optimal Sector Sojourn Time Estimation for Non-homogeneous UE Distribution

In this section, we consider M non-homogeneously distributed UEs in the cell while the rest of the system parameters remain unchanged. Let $t_s = \tau + T_s$ be the sector sojourn time of a sector s. It is notable that, in case of homogeneous UE distribution, $T_s = T$ given by (3.26) was optimal. However, when the variance of UEs distribution among the sectors is high, the round-robin scheduling of sectors results in UE starvation on long-run basis in densely populated sectors. Finding the best sectorization schemes for each beam individually is one way to increase the fairness of long-run UE rates for a given value of N^*_{RF}. This method requires a search of $|\mathcal{S}|^{N^*_{RF}}$ combinations. Another way to

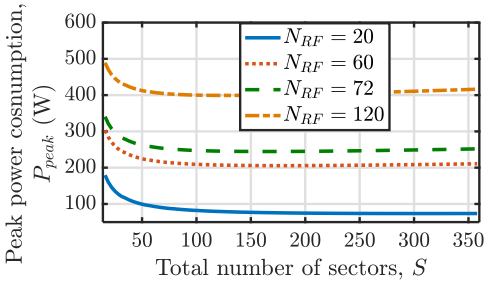

Figure 3.4: P_{peak} versus sectorization scheme for different N_{RF}.

improve fairness is to optimize t_s. Therefore, we propose WRR scheduling in which t_s is calculated to maximize the fairness of long-run UE rates.

Here, we present the analysis for a single beam b out of parallel N_{RF} beams, serving $\mathcal{S}_b$ sectors in a cell sweep duration T_{tot}. The same analysis is applicable for the rest of the beams. The fairness index $\bar{G}$ is the highest when all the UEs have the same $R_k^s\ \forall k, s \in \mathcal{S}_b$. In a sectored-cell system model, however, optimizing the scheduling time for each UE is not feasible. Nevertheless, we characterize the fairness in terms of expected long-run UE rate within a sector, $\bar{R}_s = \sum_{k=1}^{K_s} R_k^s/K_s$. Hence, as K_s increases the fraction of resources per UE in a sector decreases. Therefore, different sectors will experience different mean UE rate. For equal fairness guarantee, let $\bar{R}_s t_s = C$ (constant) $\forall s \in \mathcal{S}_b$ such that $\sum_{s\in\mathcal{S}_b} t_s \leq T_{tot}$, assuming $t_s \in \mathbb{R}^+$. Thus,

$$\sum_s t_s = \sum_s \frac{C}{1/\bar{R}_s} \Rightarrow C = \frac{T_{tot}}{\sum_s 1/\bar{R}_s} \Rightarrow t_s = \frac{T_{tot}/\bar{R}_s}{\sum_{s'} 1/\bar{R}_{s'}}. \tag{3.28}$$

Accordingly, the weights for determining t_s in WRR are $w_s = 1/\bar{R}_s$. However, t_s should be integer multiple of T_{OFDM}. Therefore, the problem to find sector sojourn time (excluding beacon subframe in each sector) is to determine

$$T_s = \frac{w_s}{\sum_{s'\in\mathcal{S}_b} w_{s'}}(T_{tot} - |\mathcal{S}_b|\tau) \triangleq n_s T_{OFDM},\ \forall s \tag{3.29}$$

such that $n_s \in \mathbb{Z}^+,\ \forall s$ and $\sum_{s\in\mathcal{S}_b} n_s T_{OFDM} \leq T_{tot} - |\mathcal{S}_b|\tau$.

Remark 3.3. *Let $f(\mathbf{t}) = \sum_{s\in\mathcal{S}_b} \bar{R}_s n_s T_{OFDM}$ be the total cell throughput, where $\mathbf{t} = \{n_s\}_{s\in\mathcal{S}_b}$. The solution $\mathbf{t} = \mathbf{t}^0 \in \mathbb{R}^+$ obtained from* (3.28) *gives an upper bound $f_{max} = f(\mathbf{t}^0)$. Let $\mathcal{T}$ be the feasible search region of $\mathbf{t}$ satisfying $C41$ and $C42$. For some $\mathbf{t}' \in \mathcal{T}$, the condition $f(\mathbf{t}') > f(\mathbf{t}^0)$ is possible only if sectors with higher $\bar{R}_s$ (equivalently smaller K_s) are allocated more time, hence contradicting the required objective of WRR. Therefore f_{max} acts as the upper bound on the throughput maximization while solving for $\mathcal{P}4$.*

Consequently, the LP reduces to the form

$$\begin{aligned} &(\mathcal{P}4): \underset{\{n_s\}\in\mathbb{Z}^+}{\text{argmax}}\ f(\mathbf{t}) = \sum_{s\in\mathcal{S}_b} \bar{R}_s n_s T_{OFDM} \\ \text{s.t.}\ \ &C41: \lfloor \mathbf{t}^0(s) \rfloor \leq n_s \leq \lceil \mathbf{t}^0(s) \rceil,\ \forall s;\ C42: \sum_{s\in\mathcal{S}_b} n_s T_{OFDM} \leq T_{tot} - |\mathcal{S}_b|\tau \\ &C43: f(\mathbf{t}) \leq f(\mathbf{t}^0). \end{aligned} \tag{3.30}$$

Algorithm 3.4 Integer LP to find optimal sector sojourn time

Input: $\bar{R}_s \; \forall s \in \mathcal{S}_b, T_{tot}, T_{OFDM}$
Output: $\mathbf{t}^* = \{n_s^*\} \; \forall s \in \mathcal{S}_b$
Solve for $\mathbf{t}^0 = \{n_s\}$ using LP in (3.28) with integer restriction relaxed
Initialize: $j = 0; f_{max} = f(\mathbf{t}^0); \mathbf{t} = \emptyset$
while $\mathcal{S}_b \neq \emptyset$ **do**
    $s_j = \mathcal{S}_b\{1\}, j = j + 1$
    $\mathcal{S}_b = \mathcal{S}_b \backslash \{s_j\}$
    Set $n_j^+ = \lceil \mathbf{t}^0(j) \rceil$ and $n_j^- = \lfloor \mathbf{t}^0(j) \rfloor$
    Find $\hat{\mathbf{t}}^+ = \{n_s \forall s \in \mathcal{S}_b | n_1, \cdots, n_{j-1}, n_j^+\}$; $\hat{\mathbf{t}}^- = \{n_s \forall s \in \mathcal{S}_b | n_1, \cdots, n_{j-1}, n_j^-\}$ from (3.28)
    substituting $T_{tot} = T_{tot} - |\mathcal{S}_b|\tau - \sum_{i=1}^{j} n_s T_{OFDM}$
    if $f(\hat{\mathbf{t}}^+) \leq f_{max}$ and $f(\hat{\mathbf{t}}^+) \geq f(\hat{\mathbf{t}}^-)$ **then**
        $\mathbf{t}^*(j) = n_j^+$
    else
        $\mathbf{t}^*(j) = n_j^-$
    end if
end

The steps to find optimal $\mathbf{t}^* = \{n_s^*\}_{s \in \mathcal{S}_b}$ are presented in Algorithm 3.4. The search for $\mathbf{t}^0 \in \mathbb{R}^+$ begins by finding w_s from (3.28). Subsequently, the objective is to maximize $f(\mathbf{t})$ while searching for $t \in \mathbb{Z}^+$. The constraint $C41$ reduces the search space considerably by bounding each n_s to two nearest integer values of $\mathbf{t}^0(s)$ only. The explanation of upper bound on n_s is given in Remark 3.3, and the lower bound on n_s is justified by the fact that setting $n_s < \lfloor \mathbf{t}^0(s) \rfloor$ will lower the throughput. In Algorithm 3.4, at jth iteration the jth sector $s_j = \mathcal{S}_b\{1\}$ is selected to find the corresponding optimal n_j^*, and $\mathcal{S}_b$ is updated by excluding s_j. The two possible integer values of n_j are found as $n_j^+ = \lceil \mathbf{t}^0(j) \rceil$ and $n_j^- = \lfloor \mathbf{t}^0(j) \rfloor$. Thereafter, $\hat{\mathbf{t}}^+(\hat{\mathbf{t}}^-) \in \mathbb{R}^+$ for all the remaining sectors $s \in \mathcal{S}_b$ is found from (3.28) given $\{n_1^*, \cdots, n_{j-1}^*\}$ and $n_j^+(n_j^-)$. If the solution is feasible and $f(\hat{\mathbf{t}}^+) \geq f(\hat{\mathbf{t}}^-)$, then $\mathbf{t}^*(j) = n_j^+$; otherwise $\mathbf{t}^*(j) = n_j^-$.

3.5 Complexity Analysis

Below, we present the computational complexity of different modules.

3.5.1 Subcarrier and Power Allocation per Sector

For a system with K_s UEs and N_c subcarriers in a sector, $\mathcal{P}1$ has a complexity of $\mathcal{O}(\zeta_R(K_sN_c + \zeta_\eta(N_c^2 \log N_c)))$ [83], where ζ_R and ζ_η denote the number of iterations required for convergence of rate and power allocation, respectively. Using the proposed subcarrier and power optimization, total complexity of resource allocation of $\mathcal{P}2$ and $\mathcal{P}3$ is reduced to $\mathcal{O}(N_c \sum_{k=1}^{K_s} \eta_P |\omega_k| \log(|\omega_k|)) = \mathcal{O}_1$. Here, η_P is the number of iterations required for convergence of power allocation.

3.5.2 Cell Wweeping Schemes

Let ζ_R' be the number of iterations required for convergence of cell peak sum rate for coordinated interference reduction in Algorithm 3.2. Thus, Algorithm 3.2 has a complexity of $I\zeta_R' N_{RF} \mathcal{O}_1$ per epoch, where I is the number of epochs in synchronous cell sweeping. On contrary, in Algorithm 3.3, due to non-coordinated resource allocation, the resource optimization step in sectors is performed only once per epoch. Thus, the complexity of Algorithm 3.3 is reduced to $I' N_{RF} \mathcal{O}_1$, where I' is total number of epochs in asynchronous cell sweeping. The complexity of Algorithm 3.2 is smaller as $I' \leq I\zeta_R'$. A worst-case comparison is performed over all the combinations of S and N_{RF} to jointly estimate S^* and N_{RF}^*.

3.5.3 Estimation of Sector Sojourn Time

In Algorithm 3.4, after solving for $\mathbf{t} \in \mathbb{R}^+$ using (3.28), the integer optimal $\mathbf{t}^*$ is found sequentially for all the sectors covered by a beam, i.e., the sector sojourn time estimation loop is executed $|\mathcal{S}_b|$ per beam having a total complexity of $\mathcal{O}(N_{RF}|\mathcal{S}_b|)$.

3.6 Results and Discussions

In this section, we present the numerical simulation results generated using MATLAB. The simulation set-up configurations are given in Table 3.2. First, we present the simulations illustrating the advantages of the proposed variable time frame structure and then proceed using this MAC protocol as an underlying access mechanism for studying optimum system performance with homogeneous and non-homogeneous UE distribution scenarios.

The numerical results are compared with the 3GPP NR scheme as a baseline. For beam management and data transmission, the total time in 3GPP NR scheme is divided into control and data parts [52]. The IA technique is explained in Section III-A and is performed during beam management phase. The UEs are grouped into N_{RF} sets based on AoD similarities in 3GPP NR scheme [84]. Further, at most N_{RF} UEs are scheduled in time domain for data transmission with a dedicated RF unit per UE employing baseband precoding to reduce IUI. Note that, as per the 3GPP NR specifications, a slot is of 14 OFDM symbols and a beam stays in a specific direction for an integer multiple of a slot duration.

Table 3.2: Simulation parameters and values

Parameter	**Description**	**Value**
D	Cell Diameter	400 m
f_c	Carrier frequency	28 GHz
B	Bandwidth	1 GHz
θ	HPBW	1^o to 25^o
U	Number of UEs	$100, 600$
N_c	Number of subcarriers	32
d'	Inter-element ULA spacing	$\lambda_c/2$
S	Number of sectors	14 to 360
N_{RF}	Number of concurrent beams	$\leq S$
N_0	Noise spectral density	-174 dBm/Hz
K_R	Rician fading parameter	8 dB
T_{tot}	SS block periodicity	20 ms
$\delta\phi$	zone angular granularity	1^o
T_{tot}	SS burst periodicity	20 ms
EIRP	Effective isotropic radiated power	52 dBm
N_t	Number of antenna elements per RF unit at gNB	5 to 115
L_k	Number of MPCs	1 (LOS), 4 (NLOS)
$\alpha_{k,l}$	lth MPC fading parameter	Rician (LOS), Rayleigh (NLOS)
N_r	Number of antenna elements at UE	4
S_r	Number of UE steerable directions	12

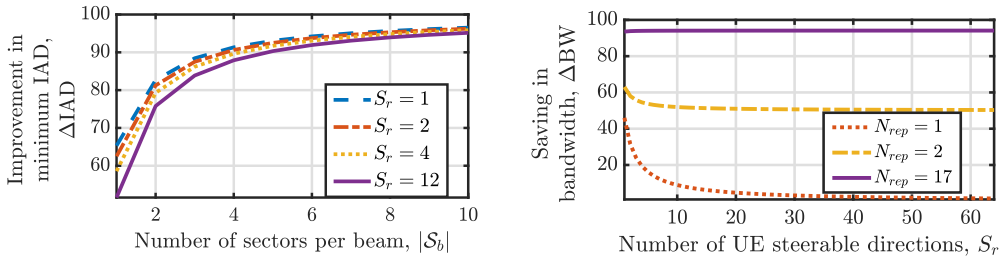

(a) IAD (b) ΔBW

Figure 3.5: (a) Improvement in IAD with $N_{rep} = 17$ using proposed IA procedure over the 3GPP NR. $N_{rep} = 17$ is equivalent to using full 1 GHz bandwidth for SS blocks. (b) Saving in bandwidth using proposed IA procedure over the 3GPP NR.

3.6.1 Performance Evaluation of the Proposed Frame Structure

3.6.1.1 IAD

With the proposed frame structure, considering no contention, IA of a UE can be performed within a beacon duration, whereas 3GPP NR uses exhaustive beam search over the entire region before final RAR transmission to the UE. Here, we consider $t_{c2} = 5T_{OFDM}$ and $t_{c4} = 4T_{OFDM}$ (explanation given in Appendix C.) Fig. 3.5(a) shows the percentage IAD improvement with the proposed IA procedure over 3GPP NR. Further, using the proposed IA procedure a considerable amount of BW (given by (3.13)) is saved, as shown in Fig. 3.5(b).

3.6.1.2 Multiple UEs per Beam

Figs. 3.6(a) and 3.6(b) illustrate the benefit of serving multiple UEs at a time located in a sector by a beam using wideband mmWave channel. In 3.6(a) the decline in $\bar{R}$ with

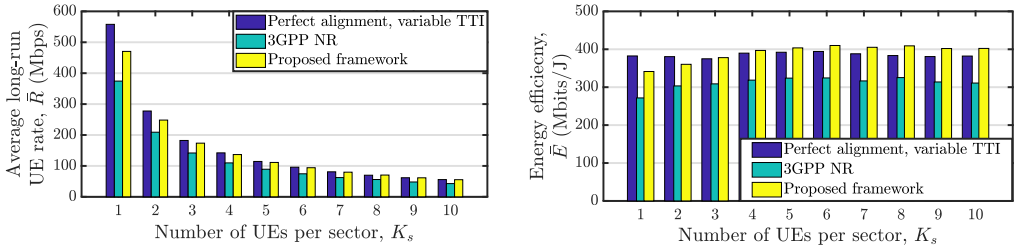

(a) Average long-run UE rate (b) gNB energy efficiency

Figure 3.6: Comparison of (a) average long-run UE rate and (b) gNB energy efficiency with the existing protocols and proposed protocol. Here, $|\mathcal{S}_b| = 5$ and $S_r = 12$.

K_s is non-linear. Thus, it is suitable to serve multiple UEs at a time over wideband mmWave channel. We compare the performances of the proposed frame structure with two other competitive standalone mmWave communication schemes: 3GPP NR scheme and perfect gNB-UE beam alignment with variable TTI frame structure scheme [53]. Figs. 3.6(a) and 3.6(b) show that the $\bar{R}$ of UEs and the energy efficiency of the gNB (ratio of total bits transmitted to total energy consumed) outperform the 3GPP NR model and are comparable to variable TTI with perfect beam alignment scheme. Nonetheless, it is not possible to achieve perfect beam alignment practically.

3.6.2 Optimum $\mathbf{S}^*$ and $\mathbf{N_{RF}}^*$ for Homogeneous UE Distribution

Fig. 3.7(a) shows the EIRP level in main-lobe and side-lobes for beams of different width attained from analog beamforming vector given by (3.6). Even though narrow beams have a high gain, modulating P_t for maintaining constant EIRP results in a reduced effective radiated power from the interfering side-lobes. Moreover, the cell coverage range is maintained constant, and the peak EIRP is the same irrespective of the beamwidth. Fig. 3.7(b) shows that the normalized interference power P_I, from side-lobes of interfering beams, experienced by a UE in a sector increases with increased Θ (equivalent to reduced S). It is notable, that power allocation using Algorithm 3.1 has $\eta_p < 100$ when $\eta_k^{(0)} = 1\ \forall k$, $\hat{\epsilon} = 0.05$ and convergence tolerance $= 10^{-4}$. We also observe that P_I increases with a higher value of N_{RF}. From Fig. 3.7(c) it is verified that solving for subcarrier and power resource allocation in Algorithm 3.2, the peak sector sum rate in an epoch converges in less than 20 iterations; in 1^{st} iteration peak sum rate is maximum and invariant of N_{RF} due to the initial assumption of zero interference per subcarrier. Further, from Fig. 3.7(c) we study that, for fixed S, increasing N_{RF} degrades the peak sector throughput, which is because of the increase in P_I. Note at $N_{RF} = 3$, the beams are 120^o apart from each other

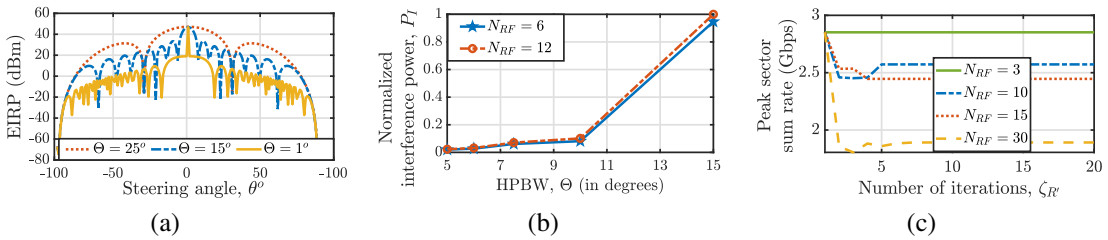

(a) (b) (c)

Figure 3.7: (a) EIRP level in main-lobe and side-lobes in a beam at different beamwidth. (b) Normalized interference experienced by a UE with respect to variable HPBW. (c) Convergence of peak sector sum rate in an epoch using Algorithm 3.2 for $S = 30$ and $M = 100$.

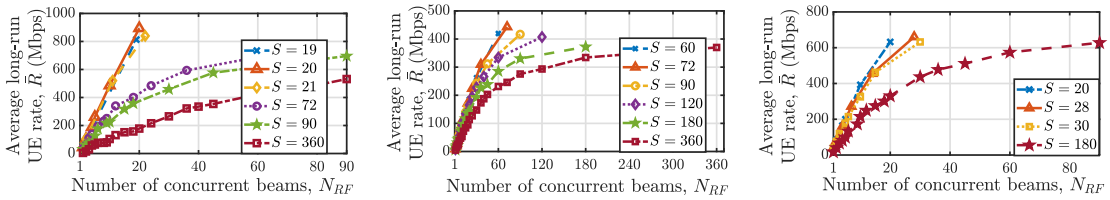

(a) Synchronous, $M = 100$ (b) Synchronous, $M = 400$ (c) Asynchronous $M = 100$

Figure 3.8: Illustration of $\bar{R}$ as a function of S and N_{RF}.

and have negligible inter-beam interference, thus the peak sum rate remains constant.

Remark 3.4. *Despite a decrease in peak throughput per sector, the average long-run UE rate $\bar{R}$ improves with increased N_{RF} for a fixed S. The improvement in $\bar{R}$ with N_{RF} is because of the fact that the increase in sector sojourn time from using a large number of concurrent beams overcomes the rate loss due to increased interference level. Therefore, for a given S, the maximum $\bar{R}$ is achieved at $N_{RF} = S$.*

From Fig. 3.8(a) and 3.8(b), we observe that even with $N_{RF} = S$, the highest value of $\bar{R}$ is achieved at $S^* = 20$ and $S^* = 72$, respectively, for $M = 100$ and $M = 400$ homogeneously distributed UEs. This is so because, for $S < S^*$ (or equivalently $\Theta > \Theta^*$) the interference from sidelobes of concurrent beams is high, as noted from Fig. 3.7(a). For $S > S^*$ even though effective interference from sidelobes of a single concurrent beam is small, because of a large value of N_{RF} the cumulative interference is increased which degrades $\bar{R}$. Hence, using the narrowest possible beam is not beneficial. Results in Figs. 3.8(a) and 3.8(b) are generated using synchronous cell sweeping. From Fig. 3.8(c) we observe that for asynchronous cell sweeping at $M = 100$ the value of $S^* = 28$ which is slightly higher as compared to synchronous cell sweeping ($S^* = 20$) although maximum attainable $\bar{R}$ is a little reduced. Furthermore, P_{budget} limits the number of beams N_{RF} that can be activated at gNB, which influences S^* selection. For example, the optimal parameters are $(S^*, N^*_{RF}) = (30, 15)$, with $\bar{R} = 210.58$ Mbps and $P_{peak} = 49.07$ W, when $M = 400$ and the $P_{budget} = 50$ W (Fig. 3.4). If gNB has no peak power constraint, the best answer is $(S^*, N^*_{RF}) = (72, 72)$, with maximum $\bar{R} = 458.72$ Mbps and $P_{peak} = 271.63$ W.

Table 3.3 compares the scheduling complexity of the proposed model over the existing competitive UE scheduling schemes, using fully and partially connected hybrid beamforming structure, as a function of M, N_{RF}, and N_t at the gNB. The work in [19, 84, 85] dedicate one RF chain per UE at a time using 3GPP NR MAC as underlying protocol. In our proposed model all the UEs that are located within the beam coverage area are served

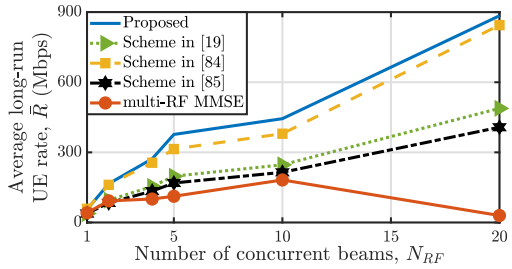

Figure 3.9: Comparison of achievable $\bar{R}$ of the proposed system model with the schemes in [19,84,85] and multi-RF MMSE method for $M = 100$.

simultaneously. Hence, scheduling is independent of M and depends only on the N_{RF}. Further, Fig. 3.9 shows that the proposed sectored-cell model using multi-analog beams with optimum beamwidth for serving multiple UEs per beam achieves better $\bar{R}$ and also with reduced scheduling complexity compared to the models in [19, 84, 85]. For the sake of fair comparison, we fix the total number of antenna elements at gNB equal to 256 and maintain $N_t \leq 256/N_{RF}$ in the proposed model.

We also analyze a scenario in which multi-RF beams in a sectored-cell model serve multiple UEs per beam over OFDMA, where, instead of the proposed power allocation in Algorithm 3.2, the baseband utilizes an MMSE precoder per subcarrier to minimize inter-beam interference. We denote this as multi-RF MMSE method. Besides high computation complexity, the multi-RF MMSE approach has smaller $\bar{R}$, as shown in Fig. 3.9, because the worst UE channel condition acts as a bottleneck to its performance. In contrast, the approaches in [19, 84, 85] only distribute subcarriers to UEs having orthogonal channel conditions and thus have better performance compared to the multi-RF MMSE approach. Though in multi-RF MMSE approach the spatial multiplexing gain is large at higher value of N_{RF}, $\bar{R}$ degrades after certain high value of N_{RF}. This is because in sectored-cell model, the RF beams are not perfectly orthogonal, and hence dominant eigenmodes are close to zero in some beam directions, thus limiting the throughput.

Table 3.3: UE scheduling complexity

User scheduling Method	**Hybrid structure**	**Complexity**
Channel correlation [19]	Fully-connected	$\mathcal{O}(M)$
AoD's similarities [84]	Fully-connected	$\mathcal{O}(MN_{RF}\eta_I)$
Virtual beamforming [85]	Partially-connected	$\mathcal{O}(N_{RF}^2)$
Proposed method	Partially-connected	$\mathcal{O}(N_{RF})$

η_I: number of iterations for algorithm convergence

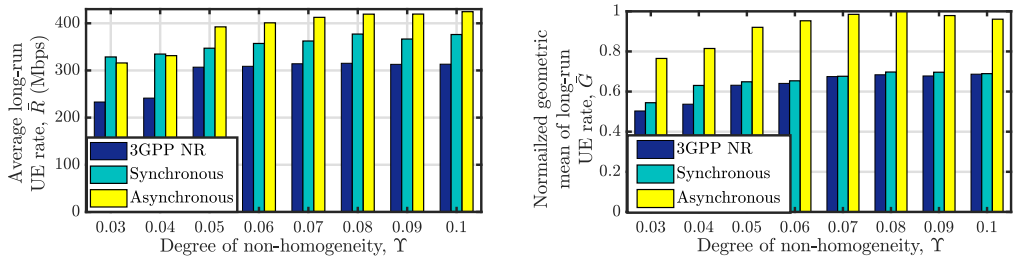

(a) $\bar{R}$ (b) Normalized $\bar{G}$

Figure 3.10: Comparison of (a) $\bar{R}$ and (b) normalized $\bar{G}$ for $M = 100$ non-homogeneously distributed UE achieved with 3GPP NR, synchronous and asynchronous schemes.

3.6.3 Optimal Sector Sojourn Time Estimation for Non-homogeneous UE Distribution using WRR

We set $Z = N_{RF}$ in (3.1) for non-homogeneous UE set-up such that $|\mathcal{S}_b| = 4$ for $S^* = 28$ at $M = 100$. Fig. 3.10(a) shows that with increasing Υ asynchronous scheme offers improved $\bar{R}$ as opposed to allocating equivalent sector sojourn time to all sectors in the synchronous scheme. Also, compared to the 3GPP NR scheme a notable gain in $\bar{R}$ with the asynchronous scheme is achieved because bandwidth consumed in control overhead is less using variable time frame at MAC layer (shown in Fig. 3.5(a) and the wideband channel is efficiently utilized by serving multiple UEs at a time. Moreover, significant improvement in fairness $\bar{G}$ of long-run UE rates with asynchronous over synchronous and 3GPP NR scheme is achieved, as shown in Fig. 3.10(b). This is so because sectors with higher K_s (hence, smaller $\bar{R}_s$) are allocated more time.

3.7 Summary

In this chapter, the sectored-cell framework to serve a large UE population with multiple RF chains while taking into account the inter-beam interference and beam squint effect in wideband mmWave channel has been studied. In the proposed multi-RF sectored-cell system model, multiple UEs are scheduled over the wideband channel using OFDMA at any given time. Moreover, in an epoch, each RF unit serves a single sector. In comparison to other competing user grouping hybrid beamforming designs, the proposed model does not require zero-forcing precoding. The RF beamformer has been designed depending on the steering angle required to serve a sector. Thereafter, subcarrier allocation and power allocation have been jointly optimized. From rate support findings, it has been

observed that for a given cell sectorization, while interference from the side-lobes of concurrent beams decreases UE's peak data rate, the time-averaged data rate increases with the higher number of RF chains. Also, it has been shown that using the narrowest beamwidth is not optimal. Besides, it has been observed that raising the number of concurrent beams in a cell causes not only increased side-lobe interference but also increases the gNB power budget. Hence, the power budget plays a crucial role in deciding the optimum number of beams and the sector beamwidth. A variable time frame structure has also been proposed that requires less IAD and has high bandwidth utilization. Further, it has been demonstrated that by using the variable frame structure, non-homogeneously distributed UEs can be scheduled efficiently, thus improving UE fairness index as well as the average long-run UE rate.

Despite the benefits of a variable frame time structure in mmWave communication systems, it is crucial to ensure timing synchronization between the UE and the gNB in order to accurately detect beacon signals within a sweep duration in practical implementations. This issue also impacts the sleep cycle of the UE, which requires further study. Additionally, there is a need to investigate the extension of the sectored-cell framework to the case of 3-D terrestrial mmWave communication. The other possible future works include comparison of efficiency of variable time frame structure for different 3GPP NR frame methodology and extending the proposed sectored-cell system to the case of uniform and non-uniform amplitude planar arrays that would require optimizing antenna amplitude, gNB height, elevation HPBW, and sector scheduling with UE fairness.

Appendices for Chapter 3

A. Proof of $\int_{\hat{\phi}} \mathcal{Q}(ar(\hat{\phi}))d\hat{\phi} = 1$

$$\begin{aligned}\int_{\hat{\phi}=0^o}^{360^o} \mathcal{Q}(ar(\hat{\phi}))d\hat{\phi} &= \int_{\hat{\phi}=0^o}^{360^o} \frac{\exp(\Upsilon \lfloor \frac{\text{mod}(\hat{\phi},360^o/Z)}{\delta\phi} \rfloor \delta\phi)}{Z\sum_{i=0}^{(360^o/Z\delta\phi)-1}\exp(\Upsilon i\delta\phi)} d\hat{\phi} \\ &= \int_{\hat{\phi}=0^o}^{\frac{360^o}{Z}} I(\hat{\phi})d\hat{\phi} + \cdots + \int_{\hat{\phi}=\frac{(z-1)360^o}{Z}}^{\frac{z360^o}{Z}} I(\hat{\phi})d\hat{\phi} + \cdots + \int_{\hat{\phi}=\frac{(Z-1)360^o}{Z}}^{360^o} I(\hat{\phi})d\hat{\phi}\end{aligned} \tag{A.1}$$

where $I(\hat{\phi}) = \frac{\exp(\Upsilon \lfloor \frac{\text{mod}(\hat{\phi},360^o/Z)}{\delta\phi} \rfloor \delta\phi)}{\left(Z\sum_{i=0}^{(360^o/Z\delta\phi)-1}\exp(\Upsilon i\delta\phi)\right)}$ and $z = \{1, \cdots, Z\}$.

Let $\tilde{\phi} = \text{mod}(\hat{\phi}, 360^o/Z)$. Then (A.1) can be written as

$$\begin{aligned}\int_{\hat{\phi}=0^o}^{360^o} \mathcal{Q}(ar(\hat{\phi})) &= Z \int_{\tilde{\phi}=0^o}^{360^o/Z} I(\tilde{\phi}) d\tilde{\phi} \\ &= Z \int_{\tilde{\phi}=0^o}^{360^o/Z} \frac{\exp(\Upsilon \lfloor \tilde{\phi}/\delta\phi \rfloor \delta\phi)}{Z \sum_{i=0}^{(360^o/Z\delta\phi)-1} \exp(\Upsilon i \delta\phi)} d\tilde{\phi}.\end{aligned} \tag{A.2}$$

As per the definition, $\mathcal{Q}(ar(\hat{\phi}))$ is constant within the angular granularity of $\delta\phi$. Therefore, integration is replaced by summation and $\lfloor \tilde{\phi}/\delta\phi \rfloor \triangleq \tilde{\phi}/\delta\phi = j$, and hence

$$\int_{\hat{\phi}=0^o}^{360^o} \mathcal{Q}(ar(\hat{\phi})) = Z \sum_{j=0}^{(\frac{360^o}{Z})/\delta\phi} \frac{\exp(\Upsilon j \delta\phi)}{Z \sum_{i=0}^{(360^o/Z\delta\phi)-1} \exp(\Upsilon i \delta\phi)} = 1. \tag{A.3}$$

B. Proof of Lemma 1

Lemma 1: When N_{RF} is sufficiently high, the probability of two or more UEs transmitting the same RACH preamble over PRACH in a single frame is very small.

Proof: Suppose the new UEs arrive according to Poisson distribution with mean arrival rate μ UEs/s/km^2 during a cell sweep duration, T_{tot}. With N_{RF} beams serving the cell, coverage area per beam is $Ar(N_{RF}) = \pi(D/2)^2/N_{RF}$. Then the probability of arrival of m new UEs during T_{tot} time interval is $\text{Pr}_a(m) = (\mu T_{tot} Ar(N_{RF}))^m e^{-\mu T_{tot} Ar(N_{RF})}/m!$. Consider that each new UE chooses a RACH preamble randomly from a set of $M_R = 64$ orthogonal preambles with equal probability. Then the probability that $k \geq 2$ out of m UEs chooses same RACH preamble is

$$\text{Pr}_r(k \geq 2|m) = 1 - \binom{m}{0} \left(\frac{1}{M_R}\right)^0 \left(1 - \frac{1}{M_R}\right)^m - \binom{m}{1} \left(\frac{1}{M_R}\right) \left(1 - \frac{1}{M_R}\right)^{m-1}. \tag{B.1}$$

Thus, the probability of collision, Pr_c is obtained as

$$\begin{aligned}\text{Pr}_c &= \text{Pr}_a(m) \times \text{Pr}_r(k \geq 2|m) \\ \mathbb{E}[\text{Pr}_c] &= \sum_{m=2}^{\infty} \frac{(\mu T_{tot} Ar(N_{RF}))^m e^{-\mu\delta Ar(N_{RF})}}{m!} \left[1 - \frac{m}{M_R}\left(1 - \frac{1}{M_R}\right)^{m-1} - \left(1 - \frac{1}{M_R}\right)^m\right] \\ &= \sum_{m=0}^{\infty} \frac{(\mu T_{tot} Ar(N_{RF}))^m e^{-\mu\delta Ar(N_{RF})}}{m!} \left[1 - \left(1 - \frac{1}{M_R}\right)^m \left(\frac{m}{M_R - 1} + 1\right)\right].\end{aligned} \tag{B.2}$$

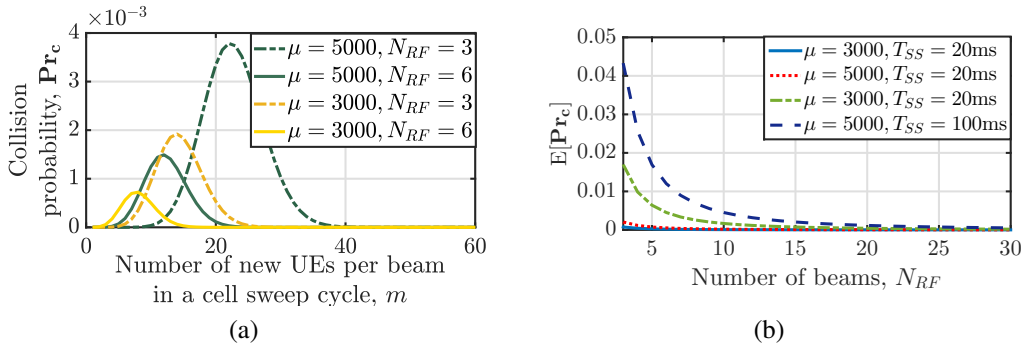

Figure B3.1: (a) Pr_c and (b) $\mathbb{E}[\text{Pr}_c]$ of new UEs arriving during $T_{tot} = 100$ ms.

Here, we consider 3-sector LTE model as a reference. Fig. B3.1(a) shows that maximum Pr_c is very small even for worst case scenario of $T_{tot} = 100$ ms, $N_{RF} = 3$, and μ as high as 5000 UEs/Km^2/s. Fig. B3.1(b) shows that the expected collision probability decreases sharply on increasing N_{RF}, and in this set-up, $N_{RF} \geq 6$ can be considered a sufficiently high value.

□

C. Calculation of Processing Time

The processing time is given as

$$t_{process} = 0.5 N_I (2048 + 144) \kappa 2^{-\hat{\mu}} T_C, \tag{C.1}$$

where κ is a constant set to value 64, $\hat{\mu}$ corresponds to subcarrier spacing, i.e., $\Delta f = 240$ kHz $= 2^{\hat{\mu}} \times 15$ kHz, N_I is subcarrier-spacing dependent timing advance parameter, and $T_C = 1/(f_{max} N_f)$ [56]. The values $f_{max} = 480$ kHz and $N_f = 4096$ are fixed in 5G. Therefore, at $\Delta f = 240$ kHz,

$$t_{process} = N_I \times 2.23 \times 10^{-6} \text{s}. \tag{C.2}$$

N_I is obtained from trip time, i.e., $2 \times$ propagation delay$/T_{OFDM}$, which is equivalent to 1 OFDM symbol, resulting in $t_{process} = 2.23 \mu$s. Thus, the total time between the last SS block transmission and the start of PRACH is sum of the transmission delay and processing time, i.e. $t_{c2} = 4T_{OFDM} + t_{process} \geq 5$ OFDM symbols. The same processing delay is applicable after PRACH transmission. Hence, $t_{c4} \geq T_{OFDM} + t_{process} = 2$ OFDM symbols.

Acknowledgement

The content of this chapter has been based on the research publications:

(i) N. Varshney and S. De, "Joint Beamwidth and Number of Concurrent Beams Estimation in Downlink mmWave Communications," in *Proc. Nat. Conf. Commun. (NCC)*, Kanpur, India, pp. 1-6, 2021.

(ii) N. Varshney and S. De, "Multi-RF Beamforming-Based Cellular Communication Over Wideband mmWaves," *IEEE Trans. Commun.* , vol. 70, no. 4, pp. 2772-2787, April 2022.

Chapter 4

Joint Beamforming and Subcarrier Allocation with Beam Squint in Wideband mmWave Communication Systems

4.1 Introduction

Beam squint is a critical and essential aspect of wideband mmWaves communication systems. We now study beam squint effect in detail for a multi-user wideband mmWave communication scenario, in addition to the incorporation of beam squint effect in design of mmWave channel matrix as in the previous chapter. Numerous studies have been done on the joint RF and BB precoder design optimization for a hybrid precoder in a wideband mmWave channel. However, majority of existing literature on wideband mmWave channel did not take the beam squint effect into account such as [15, 17–22]. A few studies that addressed the beam squint effect at mmWave regarded it as interference such as in [41, 45, 86, 87]. These works designed hybrid precoders in which the BB precoder was designed to minimize the effect of beam squint and the RF precoder was either designed using instantaneous CSI or channel's second-order characteristics [86, 87]. Very little consideration has been given to selecting an RF precoder that accounts for beam squint. It is notable that in a sub-array connected hybrid beamformer, it is not possible to design different steering weight vector of a RF precoder of a sub-array for each subcarrier. It is

so because the signal fed to the antenna sub-array connected to a RF unit is a time domain signal that is sum of signals over all subcarriers [43]. However, mmWave communication relies heavily on exact beam alignment and beam squint causes significant performance loss.

In [86] the authors designed dynamic hybrid beamformers for wideband mmWave channel with beam squint, assuming a priori knowledge of SC allocation to the users, whereas RF precoder was designed using instantaneous channel information. Similarly, in [44, 88], hybrid precoder designs for a multi-user system were proposed in which RF precoder was designed based on the channel covariance matrix, assuming prior SC allocation. We denote this as the SC-RF-BB approach. This approach assumes that the users' CSI is estimated in the beam training phase, and based on this CSI, the gNB performs SC allocation. Consequently, using this effective CSI over all SCs, the RF and BB precoders are designed for the data transmission phase.

However, the SC-RF-BB approach is not optimal because of the following reasons. Suppose one sub-array of a hybrid precoder generates a beam of width φ steered at angle θ covering multiple users. Due to beam squint, the maximum array gain at different SCs occurs at different angles. For instance, at center frequency maximum gain is at θ while at nth SC it occurs at $\theta + \Delta\theta_n$, as shown in Fig. 4.1. In this case, allocating the SC to a user with AoA closer to $\theta + \Delta\theta_n$ is more justified as it will deliver a higher gain. Thus, if the steering angle changes, then the SC allocation scheme will also vary. Accordingly, the selection of RF weight vector will affect SC allocation. Additionally, the beamwidths during beam training and data transmission phases are not the same. As evident from Fig.1, the beam squint effect varies with beamwidth. In the beam training phase, a beam of width φ^t estimates the users' CSI over different SCs. When $\varphi^t \neq \varphi$ estimating a prior SC allocation policy before designing the RF precoder for data transmission phase will vary the effective channel at each SC, affecting performance. Further, to achieve some threshold QoS and fairness in multi-user scenarios, especially when the number of users is higher than the number of RF chains, the SC-RF-BB approach cannot take advantage of channel variations over SCs to meet the desired QoS level. Again, this is because the RF precoder is designed based on second-order channel statistics, AoA, and channel correlation.

To this end, in this chapter we propose a novel approach wherein we jointly estimate the RF precoder and SC allocation policy leveraging beam squinting effect to maximize the net throughout. After that, the BB precoder is designed for minimizing inter-beam

interference. We denote this approach as the RF-SC-BB approach. To cater to multiple users, the majority of the research works to date considered serving single user over the wideband mmWave channel per RF unit while time multiplexing the co-located users in the group [86, 88, 89]. Therefore, the problem of SC allocation does not arise. However, when the user population is higher than the total number of RF chains, in Chapter 2 and 3 we have shown that it is optimal to group and serve multiple users over OFDM per beam. In such a scenario, as we will demonstrate in this chapter, our proposed RF-SC-BB approach outperforms the existing SC-RF-BB approach.

4.1.1 Chapter Organization

The remaining chapter is organized as follows. System model is presented in Section 4.2. The RF-SS-BB design is presented in Section 4.3. Simulation results are presented in Section 4.5, and the chapter is summarized in Section 4.6.

4.2 System Model

We consider a multi-user scenario of M users distributed in a 2-dimensional space using Cox process with angular spread σ_{spread}. The gNB is equipped with sub-array hybrid precoder having N_{RF} RF chains connected to a uniform linear array consisting of N_t antenna elements. Each sub-array is connected to a non-overlapping set of N_t/N_{RF} antenna elements generating one independent beam of width φ. The users are grouped into N_{RF} groups by k-means clustering. Users in a group are served using OFDMA by a single RF chain connected to a sub-array. We assume that each user has a single antenna. Let $\mathcal{K}_j$ denote the set of users located in coverage area of beam $j = \{1, \ldots, N_{RF}\}$. The mmWave channel is divided into N_c SCs.

4.2.1 Channel Model

The UE-gNB channel has $L \ll N_t$ MPCs. Therefore, the channel between the kth UE and the gNB over the nth SC at frequency f_n is represented as

$$\mathbf{h}_{k,n} = \sqrt{\frac{\mathrm{PL}_k}{L}} \sum_{l=1}^{L} \alpha_{k,l} e^{-j2\pi\tau_{k,l} f_n} \mathbf{a}_T(f_n, \phi_{k,l})^H \in \mathbb{C}^{1\times N_t} \tag{4.1}$$

where $\alpha_{k,l}$, $\tau_{k,l}$, and $\phi_{k,l}$ are respectively the small scale channel fading, delay, and AoA of lth MPC of kth UE and PL_k is the path loss of kth UE given by (2.4). The gNB array response vector $\mathbf{a}_T(f_n, \phi_{k,l})$ at an offset angle $\phi_{k,l}$ is expressed as

$$\mathbf{a}_T(f_n, \phi_{k,l}) = \frac{1}{\sqrt{N_t}} \left[1, e^{\frac{-j2\pi f_n d' \sin\phi_{k,l}}{\lambda_c f_c}}, \ldots, e^{\frac{-j2\pi f_n d'(N_t-1)\sin\phi_{k,l}}{\lambda_c f_c}}\right]^T \tag{4.2}$$

where f_n/f_c is the beam squint factor at frequency f_n, d' is the inter element ULA spacing, and λ_c is the carrier wavelength. For simplicity, we assume perfect channel knowledge.

4.2.2 Precoder

The sub-array hybrid precoder in the data transmission phase is composed of RF and BB precoder. In each sub-array, the same RF beamforming weight vector is applied at all the SCs. The analog precoding matrix $\mathbf{A}_{RF}$ of the sub-array hybrid structure is of the form

$$\mathbf{A}_{RF} = \{\mathbf{a}_1, \ldots, \mathbf{a}_{N_{RF}}\} \in \mathbb{C}^{N_t \times N_{RF}}. \tag{4.3}$$

Here $\mathbf{a}_j \in \mathbb{C}^{N_t \times 1}$ is the RF weight vector of jth sub-array. In general the beam's half power beamwidth is $\varphi \approx 360/(\pi N_t/N_{RF})$ (degrees). The phase shifters have discrete phases that are controlled by b bits and decide the steering direction. Therefore, the possible steering directions (θ) are uniform over the 2π range from the set $\Theta = \{2\pi i/2^b | i = 0, \ldots, 2^b - 1\}$. The resulting RF weight vector of the jth sub-array steered at angle $\theta_j \in \Theta$ for all frequencies is

$$\mathbf{a}^j = \begin{cases} e^{-j\frac{2\pi}{\lambda_c} d'(m-1)\sin\theta_j} & \forall m \in [(j-1)\frac{N_t}{N_{RF}} + 1 : j\frac{N_t}{N_{RF}}], \\ 0 & \text{otherwise.} \end{cases} \tag{4.4}$$

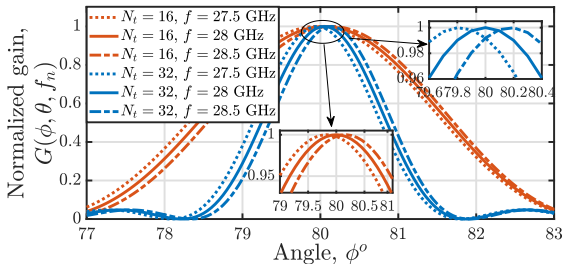

Figure 4.1: Illustration of beam squinting effect at 28 GHz with $N_{RF} = 1$ connected to N_t antennas and steered at 80^o.

Due to beam squint, each SC experiences different gains for the same RF precoder. Therefore, the effective gain experienced by a UE at frequency f_n situated at an offset angle ϕ from a beam steered at an angle θ is [90]

$$\begin{aligned} G(\phi,\theta,f_n) &= \left|\mathbf{a}_T(f_n,\phi)^H\mathbf{a}^j(\theta)\right|^2 \\ &= \left|\frac{1}{\sqrt{N_t}}\sum_{m=1}^{N_t} e^{-j\frac{2\pi}{\lambda_c}d'(m-1)(\frac{f_n}{f_c}\sin\phi-\sin\theta)}\right|^2. \end{aligned} \tag{4.5}$$

As shown in Fig. 4.1, the beam gains fall off more sharply in narrower beams (higher N_t) and hence, are more affected by the beam squinting effect.

In a sub-array hybrid precoder each RF unit transmits one data stream. Thus, over nth SC the jth RF unit transmits signal x_n^j only. At baseband, x_n^j is multiplied by BB beamforming weight d_n^j to reduce inter-beam interference resulting from the sidelobes of the other $N_{RF}-1$ concurrent beams over the nth SC. Let $\mathbf{D}[n]$ denote the BB precoder at nth SC, which is of the form

$$\mathbf{D}_n = \text{diag}\{d_n^1,\ldots,d_n^{N_{RF}}\} \tag{4.6}$$

such that $\sum_{n=1}^{N_c}\text{Tr}\{\mathbf{D}_n\mathbf{D}_n^H\}\leq P_t$, where P_t is the maximum transmit power.

4.2.3 Achievable Rate

On nth SC, the baseband of jth RF unit transmits unit energy signal x_n^j to UE $k\in\mathcal{K}_j$ where $j\in\{1,2,\ldots,N_{RF}\}$. Therefore, let $\mathbf{x}[n]=\left[x_n^1,\ldots x_n^{N_{RF}}\right]^T$ be the input signal to the BB precoder. Then, assuming kth UE is allocated on nth SC, the received signal is $y_{k,n}=\mathbf{h}_{k,n}\mathbf{A}_{RF}\mathbf{D}_n x_n+m_n$, where m_n is noise variable with distribution $\mathcal{N}(0,\sigma^2)$. Therefore, achievable data rate of jth beam on nth SC is

$$R_{k,n}^j=\log_2\left(1+\frac{\pi_{k,n}^j\left|\mathbf{h}_{k,n}\mathbf{a}^j d_n^j\right|^2}{\sigma_n^2+\sum_{i\neq j}\pi_{k,n}^i\left|\mathbf{h}_{k,n}\mathbf{a}^i d_n^i\right|^2}\right) \tag{4.7}$$

where $\pi_{k,n}^i\in 0,1$ is the SC allocation variable. $\pi_{k,n}^i=1$ if UE k allocated to SC n by ith RF unit and 0, otherwise.

4.3 RF-SC-BB Design

4.3.1 Problem Formulation

We first jointly design the SC allocation and RF precoder, and then design the BB precoder. To ensure fairness to LoS and NLoS UEs, we proportionally allocate the SCs to all the UEs in each beam using OFDMA, which is equivalent to maximizing sum log-rate. Thus, the optimization problem is

$$\begin{aligned} \mathcal{P}1: \max_{\boldsymbol{\pi},\mathbf{D},\mathbf{A}_{RF}} & \sum_{j=1}^{N_{RF}} \sum_{k\in\mathcal{K}_j} \ln\left(\sum_{n=1}^{N_c} \pi_{k,n}^{j} R_{k,n}^{j}\right) \\ \text{s.t.} \quad & \text{C1:} \sum_{k\in\mathcal{K}_j} \pi_{k,n}^{j} \leq 1, \forall j,n; \ \text{C2:} \ \pi_{k,n}^{j} \in \{0,1\}, \ \forall j,n,k \\ & \text{C3:} \sum_{n=1}^{N_c} \text{Tr}\{\mathbf{D}_n \mathbf{D}_n^H\} \leq P_t; \ \text{C4:} \ \mathbf{a}^j \in \Theta. \end{aligned} \tag{4.8}$$

Constraints C1 and C2 ensure binary SC allocation with no sharing within a beam. Constraint C3 limits maximum power and constraint C4 limits the possible beam steering directions. $\boldsymbol{\pi}$ and $\mathbf{D}$ are set of all $\pi_{k,n}^{j}$ and $\mathbf{D}_n$, respectively. $\mathcal{P}1$ is a mixed integer non-convex optimization problem. Therefore, we decompose it to solve for $(\boldsymbol{\pi}, \mathbf{D}, \mathbf{A}_{RF})$. We first fix $\mathbf{D}$ and optimize for $\boldsymbol{\pi}$ and $\mathbf{A}_{RF}$ in the following section.

4.3.2 RF Precoder Design and SC Allocation

Initially assuming $d_n^j = P_t/(N_c N_{RF})\ \forall n, j$ and zero inter-beam interference, we optimize for $\boldsymbol{\pi}$ and $\mathbf{A}_{RF}$. Thus, $\mathcal{P}1$ reduces to

$$\begin{aligned} \mathcal{P}2: \quad & \max_{\boldsymbol{\pi},\mathbf{A}_{RF}} \sum_{j=1}^{N_{RF}} \sum_{k\in\mathcal{K}_j} \ln\left(\sum_{n=1}^{N_c} \pi_{k,n}^{j} R_{k,n}^{j}\right) \\ \text{s.t.} \quad & \text{C1}, \ \text{C2}, \ \text{C4}. \end{aligned} \tag{4.9}$$

We find the RF precoder independently for each sub-array, given $\mathbf{h}_{k,n}\ \forall k,n$. Let for jth RF unit $\Phi_j = \{\phi_{k,l} | k \in \mathcal{K}_j\}$ be the set of all possible AoAs from all the UEs in $k \in \mathcal{K}_j$. Thus, the set of possible steering direction of jth beam is

$$\Theta_j = \{\theta_j\} = \{\underset{\theta\in\Theta}{\text{argmin}}|\theta - \min(\Phi_j)|, \underset{\theta\in\Theta}{\text{argmin}}|\theta - \max(\Phi_j)|\}. \tag{4.10}$$

Next, for a $\theta_j \in \Theta_j$ we find $\mathbf{s}^*$ by relaxing $\pi_{k,n}^j$ to be in interval $[0,1]$. Then the optimization problem reduces to

$$\mathcal{P}3: \max_{\boldsymbol{\pi}} \sum_{k\in\mathcal{K}_j} \ln\left(\sum_{n=1}^{N_c} \pi_{k,n}^j R_{k,n}^j\right); \text{ s.t. } \text{C1}. \tag{4.11}$$

Therefore, the Lagrangian of $\mathcal{P}3$ is

$$\mathcal{L}(\boldsymbol{\pi},\boldsymbol{\lambda}) = \sum_{k=1}^{K} \ln\left(\sum_{n=1}^{N_c} \pi_{k,n}^j R_{k,n}^j\right) - \sum_{n=1}^{N_c} \lambda_n \left(\sum_{k=1}^{K} \pi_{k,n}^j - 1\right) \tag{4.12}$$

where $\boldsymbol{\lambda} = [\lambda_1, \ldots, \lambda_{N_c}]$ are non-negative Lagrangian multipliers corresponding to C1. Applying KKT condition we have

$$\frac{\partial \mathcal{L}(\boldsymbol{\pi},\boldsymbol{\lambda})}{\partial \pi_{k,n}^j} = \frac{R_{k,n}^j}{\sum_{n=1}^{N_c} \pi_{k,n}^j R_{k,n}^j} - \lambda_n \leq 0. \tag{4.13}$$

Subsequently, in (4.13) $\pi_{k,n}^j = 1$ if the SC n is allocated to UE $k \in \mathcal{K}_j$ then, $R_{k,n}^j \neq 0$ and $R_{k,n}^j / \sum_{n=1}^{N_c} \pi_{k,n}^j R_{k,n}^j - \lambda_n > 0$. Otherwise, we have $R_{k,n}^j = 0$ and $R_{k,n}^j / \sum_{n=1}^{N_c} \pi_{k,n}^j R_{k,n}^j - \lambda_n \leq 0$. This implies that SC n is allocated to UE k by the following rule

$$k = \arg\max_{k\in\mathcal{K}_j} \frac{R_{k,n}^j}{\sum_{n=1}^{N_c} \pi_{k,n}^j R_{k,n}^j}. \tag{4.14}$$

To satisfy the constraint C1, λ_n is set between $R_{k,n}^j / \sum_{n=1}^{N_c} \pi_{k,n}^j R_{k,n}^j$ and one. Therefore, the optimal precoder design of jth sub-array is obtained as

$$\theta_j = \arg\max_{\theta_j\in\Theta_j} \sum_{k\in\mathcal{K}_j} \ln\left(\sum_{n=1}^{N_c} \pi_{k,n}^j R_{k,n}^j\right). \tag{4.15}$$

Therefore, the optimal steering vector of jth beam is

$$\mathbf{a}^{j^*} = \mathbf{a}(\theta_j). \tag{4.16}$$

Remark 1: While designing RF precoder, we aim to maximize throughput by using optimal RF precoder and thereafter select the corresponding optimal SC allocation policy. Further rate improvement is performed by optimizing BB precoder to reduce inter-user interference over each SC in the later stage.

4.3.3 BB Precoder Design

Let $u_{k,n}^{j}$ be the receive BB beamforming weight of the optimal UE k allocated over SC n on beam j. With the knowledge of $(\mathbf{A}_{RF}^{*}, \boldsymbol{\pi}^{*})$, in this section we design the optimal BB precoders $\mathbf{D}^{*}$ at gNB and $\mathbf{u} = \{u_{k,n}^{j}\}\ \forall k, j, n$ at UE that maximizes total rate, i.e.,

$$\mathcal{P}4: \max_{\mathbf{u},\mathbf{D}} \sum_{j=1}^{N_{RF}} \sum_{n=1}^{N_c} R_{k,n}^{j}, \quad \text{s.t. C3.} \tag{4.17}$$

We solve $\mathcal{P}4$ by transforming weighted sum-rate maximization into weighted sum-rate mean square error (WMMSE) minimization problem using block coordinate descent optimization. Let $w_{k,n}^{j}$ and $e_{k,n}^{j}$, respectively, be the weight and mean-square estimation error of UE k on nth SC in jth RF unit. Then, using WMMSE $\mathcal{P}4$ transforms to [91]

$$\mathcal{P}5: \min_{\mathbf{w},\mathbf{u},\mathbf{D}} \sum_{j=1}^{N_{RF}} \sum_{n=1}^{N_c} \left(w_{k,n}^{j} e_{k,n}^{j} - \log w_{k,n}^{j}\right); \text{ s.t. C3.} \tag{4.18}$$

Fixing $\mathbf{D}$ and minimizing weights $w_{k,n}^{j}$ leads to general MMSE receiver $u_{k,n}^{j}$, which is given by (4.19) [91]

$$u_{k,n}^{j} = \frac{\mathbf{h}_{k,n}\mathbf{a}^{j^*} d_n^j}{\sigma^2 + \sum_{i \neq j} |\mathbf{h}_{k,n}\mathbf{a}_{i^*} d_n^i|^2}. \tag{4.19}$$

Using this receiver, the corresponding mean square error is expressed as

$$e_{k,n}^{j} = \left|(u_{k,n}^{j})^H \mathbf{h}_{k,n}\mathbf{a}^{j^*} d_n^j - 1\right|^2 + \sum_{i \neq j} \left|(u_{k,n}^{j})^H \mathbf{h}_{k,n}\mathbf{a}^{i^*} d_n^i\right|^2 + \sigma_{k,n}^2 \left|u_{k,n}^{j}\right|^2. \tag{4.20}$$

Hence, the weight $w_{k,n}^{j}$ is found as

$$w_{k,n}^{j} = \left(e_{k,n}^{j}\right)^{-1}. \tag{4.21}$$

Substituting these values in (4.17) we have the equivalence, as

$$\mathcal{P}6: \max_{\mathbf{D}} \sum_{j=1}^{N_{RF}} \sum_{n=1}^{N_c} \log_2\left(1 + \frac{\left|\mathbf{h}_{k,n}\mathbf{a}^{j^*} d_n^j\right|^2}{\sigma_n^2 + \sum_{i \neq j} \left|\mathbf{h}_{k,n}\mathbf{a}^{i^*} d_n^i\right|^2}\right); \text{s.t. C3} \tag{4.22}$$

where $\mathcal{P}6$ is convex in $d_n^j\ \forall j, n$. Consequently, we solve it using KKT to obtain

$$d_n^{j\,*} = \frac{w_{k,n}^{j} {u_{k,n}^{j}}^H \mathbf{h}_{k,n}\mathbf{a}^{j^*}}{\mu + \sum_i w_{k,n}^{i} |{u_{k,n}^{i}}^H \mathbf{h}_{k,n}\mathbf{a}^{j^*}|^2} \tag{4.23}$$

where μ is the Lagrangian multiplier corresponding to C3. Substituting value of $d_j[n]$ in C3, we have

$$\sum_{n=1}^{N_c}\sum_{j=1}^{N_{RF}} \frac{\left|w_{k,n}^{j}{u_{k,n}^{j}}^{H}\mathbf{h}_{k,n}\mathbf{a}^{j^*}\right|^2}{\left(\mu+\sum_i w_{k,n}^{i}|{u_{k,n}^{i}}^{H}\mathbf{h}_{k,n}\mathbf{a}^{j^*}|^2\right)^2} \leq P_t. \tag{4.24}$$

Here, (4.24) is solved by numerical methods. Further, (4.24) is a decreasing function of μ, Therefore, if $\sum_{n=1}^{N_c}\text{Tr}\{\mathbf{D}_n(\mu=0)\mathbf{D}_n(\mu=0)\}^H \leq P_t$, then $\mathbf{D}_n^* = \mathbf{D}_n(\mu=0)$; otherwise μ^* is found using bisection search. Algorithm 4.1 lists the steps to find BB precoder and Algorithm 4.2 describes the steps for complete joint SC allocation and hybrid precoder estimation.

Algorithm 4.1 Baseband beamforming

1: Input: $N_{RF}, \boldsymbol{\pi}^*, \mathbf{A}_{RF}^*, \mathbf{h}_{k,n}\ \forall k,j,n$
2: Output: $\mathbf{D}$ and $\mathbf{u}$
3: Initialize $\mathbf{D}[n] = \mathbf{I}_{N_{RF}}P_t/(N_cN_{RF})$
4: **do**
5: Find $u_{k,n}^{j}$ using (4.19) $\forall j,n$
6: Find $w_{k,n}^{\prime j} \leftarrow w_{k,n}^{j}$ using (4.21) $\forall j,n$
7: Find μ using (4.24)
8: Find d_n^j using (4.23) $\forall j,n$
9: Update $w_{k,n}^{j}$ (4.21) $\forall j,n$
10: **while** $\left|\sum_j \log\det(\sum_n w_{k,n}^{\prime j}) - \log\det(\sum_n w_{k,n}^{j})\right| \leq \epsilon$

4.4 Complexity Analysis

In the proposed RF-SC-BB scheme, we use the same BB precoder as in SC-RF-BB approach. Therefore, for brevity, we do not compare the complexity of BB precoder for the two approaches. For fair comparison both the approaches are considered to allocate SCs to maximize the sum log-rate using (4.14) that requires $N_{RF}MN_c$ computations to determine $R_{k,n}^{j}\ \forall k,j,n$, and $|\mathcal{K}_j|$ comparisons to find k. In SC-RF-BB approach, SC allocation per beam is performed only once. Next, to find the covariance matrix of $\sum_{n=1}^{N_c}\mathbf{h}_{k,n}^{j}/N_c$ in beam j, N_t^2 multiplications are required. Further, eigenvalue decomposition of covariance matrix to find RF precoder has worst-case complexity of $\mathcal{O}(N_t^3)$. Thus, the overall complexity of SC-RF-BB approach is $\mathcal{O}1 = \mathcal{O}(2N_{RF}|\Theta| + N_{RF}MN_c +$

Algorithm 4.2 Joint SC allocation and hybrid beamforming

Input: $N_{RF}, M, \mathbf{h}_{k,n}\ \forall k, j, n$ and UE positions
Output: $\boldsymbol{\pi}^*, \mathbf{A}^*_{RF}, \mathbf{D}^*$, and $\mathbf{u}^*$
Group UEs into N_{RF} groups such that $\bigcup_{j=1}^{N_{RF}} \mathcal{K}_j = M$
for $j = 1$ to N_{RF} **do**
    Initialize $\mathbf{D}[n] = \mathbf{I}_{N_{RF}} P_t/(N_c N_{RF})$
    Assume zero inter-beam interference $\Rightarrow \mathbf{u} = \{1\}$
    Find Θ_j using (4.10)
    for $\theta_j \in \Theta_j$ **do**
        Find ${\pi^j_{k,n}}^*$ and k using (4.14) $\forall n, j$
        Calculate $\sum_{k\in\mathcal{K}_j} \ln\left(\sum_{n=1}^{N_c} \pi^j_{k,n} R^j_{k,n}\right)$
    end for
    Find θ_j using (4.15)
end for
Find $\mathbf{D}^*$ and $\mathbf{u}^*$ using steps in Algorithm 4.1

$N_c|\mathcal{K}_j| + N_t^2 + N_t^3$). In contrast, in our proposed RF-SC-BB approach, for jth beam the SC allocation is performed $|\Theta_j|$ times. Also, to compute Θ_j in (4.10) a maximum of $2|\Theta|$ searches are required. Therefore, the total computational complexity RF-SC-BB approach is $N_{RF}MN_c + \sum_{j=1}^{N_{RF}} |\Theta_j|(N_c|\mathcal{K}_j|)$. In the worst case this can be approximated as $\mathcal{O}(2N_{RF}|\Theta| + N_{RF}MN_c + N_{RF}|\Theta_j||\mathcal{K}_j|N_c) \ll \mathcal{O}1$.

4.5 Simulation and Results

In chapter chapter we consider 3 set of UE clusters are generated over a 60^0 angular area of radius 200 m using Cox process with $\sigma_{spread} = 4^o$ [92]. The mmWave system parameters are $f_c = 28$ GHz, rician channel with parameter 8 dB, $N_{RF} = 3$, $N_t = 96$ (32 per sub-array corresponding to beamwidth $\varphi \approx 3.58^o$), $N_c = 64$, $P_t = 1$, $b = 5$, $d' = \lambda/2$, $m_1 = 2, m_2 = 2.92, m_{5GHz} = 2, a_1 = 61.4, a_2 = 72, \sigma_1^2 = 33.64$, and $\sigma_2^2 = 75.69$ [65]. We also study the effect of beam squint at $f_c = 5$ GHz, with parameters $N_t^{5GHz} = 2$, Rayleigh channel, path loss exponent $= 2$, and shadowing variance $= 44.36$.

Further, we compare the performance of the proposed RF-SC-BB approach with that of the SC-RF-BF approach. In SC-RF-BB approach, SC allocation in jth beam is performed to maximize sum log-rate based on the effective CSI obtained from the beam

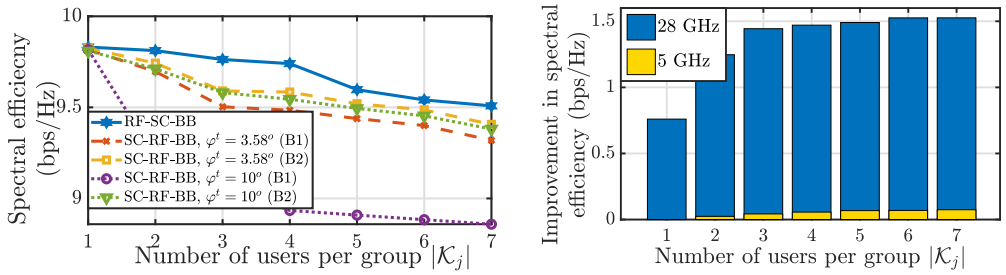

(a) (b)

Figure 4.2: (a) Spectral efficiency comparison of RF-SC-BB and benchmark SC-RF-BB approaches at 28 GHz. (b) Gain in spectral efficiency using RF-SC-BB over RF-SC-BB with approach at 28 GHz and 5 GHz.

training phase, i.e., $\mathbf{h}_{k,n}\tilde{\mathbf{a}}^j$, where $\tilde{\mathbf{a}}^j$ is the RF precoder used during beam training phase by the jth RF unit having beamwidth φ^t. It is notable that the beam training uses beam sweeping by partitioning the area into sectors equal to HPBW of the beam φ^t. Also, the beamwidth during the data transmission and the beam training is not necessarily the same, i.e, $\varphi \neq \varphi^t$. Therefore, for performance comparison, we consider two scenarios of training beamwidth $\varphi^t = \{3.58^o, 10^o\}$. Further, for sub-array hybrid precoder architecture we use two benchmarks for joint RF and BB precoding in SC-RF-BB approach. The two benchmarks are briefly described below.

- Benchmark 1 (B1) [88]: RF precoder is designed using choosing closest coodebook entry to the dominant eigenvector of the average of CSI $\{\mathbf{h}_{k,n}\}$ over all the SCs. Thereafter, a ZF based BB precoder is designed to eliminate inter-user interference.

- Benchmark 2 (B2) [44]: RF precoder common to all SCs is designed by projecting wideband channel to the central frequency and then BB precoder is designed to compensate for beam squint.

Fig. 4.2(a) verifies that the RF-SC-BB approach achieves higher spectral efficiency over both the benchmark SC-RF-BB approaches. Further, it can be observed that in SC-RF-BB approach, spectral efficiency degrades at $\varphi^t = 10^o (\neq \varphi)$ because the SC allocation used in the training phase to design RF precoder leads to degraded output during data transmission phase that has $\varphi = 3.58^o$ leading to different array response and thus, different beam squint effect. The RF-SC-BB approach achieves improved spectral efficiency with sum throughput maximization as well. For brevity, we omit the analysis here.

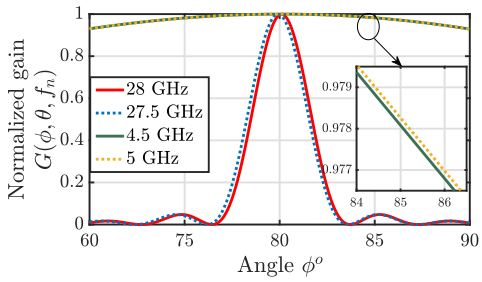

Figure 4.3: Illustration of beam squinting effects at 5GHz and 28GHz with $N_t^{5GHz} = 2$, $N_t^{28GHz} = 32$, and steering angle $= 80^o$.

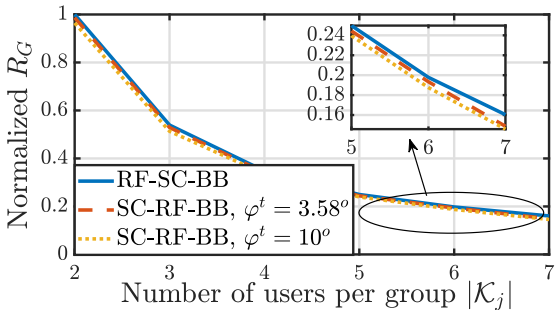

Figure 4.4: Comparison of normalized geometric mean rate of RF-SC-BB and SC-RF-BB (B1) approaches at 28 GHz.

Fig. 4.2(b) illustrates that the difference of spectral efficiency performance of the two schemes is more prominent at higher frequency, thus showing importance of the proposed scheme at mmWaves. Here, $N_{RF} = 1$, $\varphi^{28GHz} = 3.58^o$, and $\varphi^{5GHz} = 60^o$. The attenuation increases with frequency. Therefore, to maintain same power density at cell edge, the antenna array size required at 5 GHz is much smaller than the antenna array at 28 GHz frequency, resulting in broader beams and hence smaller beam squint, as shown in Fig. 4.3.

Further, we measure the UE fairness by geometric mean rate given as

$$R_G = \sqrt[M]{\prod_{k=1}^{M} R_k}. \tag{4.25}$$

where R_k is the rate of kth UE. As shown in Fig. 4.4 the RF-SC-BB offers improved fairness over SC-RF-BB approach. This is again because the SCs are allocated proportionally depending on the effective channel gain $\mathbf{h}_{k,n}\mathbf{a}^{j^*}$ after optimal RF precoder is estimated.

4.6 Summary

In this chapter, a joint subcarrier allocation and hybrid beamforming design has been proposed for a sub-array hybrid beamformer in a multi-user wideband mmWave channel. We emphasized the interlink of RF and SC allocation policy. Furthermore, it was demonstrated that, compared to the SC-RF-BB strategy, the RF-SC-BB technique increases spectral efficiency and UE fairness. It has also been showed that the performance difference is more prominent at mmWave than at sub-6 GHz.

Acknowledgement

The content of this chapter has been based on the research publication:

(i) N. Varshney and S. De, "RF Beamforming and Subcarrier Allocation Using Beam Squint in mmWave Systems," *IEEE Wireless Commun. Lett.* , vol. 11, no. 4, pp. 678-682, April 2022.

Chapter 5

Sustainable UAV-assisted Multi-user Wideband mmWave Communications

5.1 Introduction

Beyond the studies of multi-user access communication in 2-dimensional terrestrial deployment scenario in Chapters 2 through 4, we now investigate the 3-dimensional network scenario for multi-user access at mmWaves. The investigation of the feasibility of UAV operation at mmWaves is still in its infancy and little consideration has been given to UAVs acting as base stations to serve group of obstructed UEs at mmWave frequency. In this chapter we consider solar-powered UAV deployed at fixed height that act as aerial base station to provide ad hoc connectivity at mmWaves with minimum QoS guarantee to a non-homogeneously distributed terrestrial UE population. The clustered UE population considered is much larger than the number of RF chains available at the UAV. We investigate the system performance by considering practical antenna radiation pattern and the resulting sidelobe interference, wherein we exploit the fact that at mmWaves, large number of antenna elements can be placed on the UAV to provide narrow steerable beams to serve the terrestrial population.

The prior works jointly designed the RF precoder and the baseband precoders using zero-forcing (ZF) precoder or minimum mean square error (MMSE) precoders to minimize inter-user interference with a prior subcarrier allocation in a multi-user scenario [19–22]. The limitation of ZF and MMSE precoders is that the objective of these precoders is to achieve maximum sum rate, and hence do not guarantee minimum QoS to all the UEs in the system. To meet the QoS requirement while using ZF precoding, the

work in [29] optimized the power over different data streams for fully-connected hybrid architecture. Besides the complexity of joint RF precoder, baseband precoder, and greedy UE grouping algorithm in [29], the convergence rate of the proposed power allocation algorithm to satisfy QoS of all the UEs is very slow. In Chapter 4, we have shown that at mmWaves it is beneficial to first group UEs and then perform subcarrier allocation and baseband precoding leveraging beam squint. Moreover, with an aerial base station capable of generating narrow steerable beams, it is beneficial to group the UEs based on their positions rather than dividing the area into sectors as in [31]. For concurrent transmission over directional beams, authors in [93] presented a new multiple access technique to allows concurrent interbeam and intra-beam user transmissions for both the mmWave UAV uplink and downlink via flexible constellation.

Additionally, energy efficiency is an important factor to consider for long-term UAV-assisted communications [94]. The rotary-wing UAVs can perform static hovering and hence overcome the problem of beam misalignment to a large extent, which makes them perfect for use as low-altitude aerial base stations at mmWaves [95]. The works in [96,97] studied different energy efficient schemes for communication with rotary-wing UAVs. Besides, the current battery technology allows for a maximum of 1 to 2 hours of UAV operation. This duration can be extended by powering the UAV with renewable energies. Solar energy is one such readily available energy at UAV. Recently, sustainable solar-powered UAVs communication designs are being investigated in the literature. The authors in [98] proposed optimal resource allocation design and 3D trajectory route design for an energy-constrained solar-powered UAV. The studies in [99, 100] also presented energy efficient algorithms for a solar-powered UAV. However, the limitations of these studies are that they focused on the sub-6 GHz band and attempted to enhance energy efficiency using solar power harvested in real time. These studies did not look at the solar panel size optimization for providing an energy efficient system for serving UEs on a long-term basis.

From an energy efficiency standpoint, the closest work that considers the effect of the UAV power limits on the aerial communication system performance is presented in [100]. However, it considered the sub-6 GHz operation with a single RF chain generating a fixed beam of null-to-null beamwidth of 120^o. The majority of research work on UAV-assisted communication with energy limitations considered UAV trajectory optimization, placement, coverage adjustment, and optimal radio resource allocation subject to minimum rate constraint and transmit power constraint [101–104]. At mmWaves, the hardware

power consumption caused by a large number of RF chains is significant. Therefore, in this chapter we estimate the optimal number of narrow beams for energy efficient UAV operation for a given power budget. Further, we find that, in addition to the power consumed by transmission and RF hardware units, the power consumed in UAV hovering has an effect on system energy efficiency and hardware design parameters, such as solar panel sizing. When using a solar-powered UAV, the solar panel should support UAV hovering as well as communication and battery charging. The solar panel, on the other hand, adds weight, which increases hovering power and thus affects the UAV performance. To this end, solar panel design optimization is investigated in this study for a comprehensive analysis of sustainable UAV operation.

5.1.1 Contributions

The novel contributions and scope of our work are summarized below.

a) A multi-user UAV-assisted communication system at mmWaves with minimum QoS requirements is presented for UEs distributed non-homogeneously over a small region. At UAV, UE grouping is carried out and the UEs in one group are served by a single RF chain employing OFDMA.

b) UE grouping using k-means clustering is proposed with adjustable beamwidth in azimuth and elevation plane. Using Monte Carlo simulation results, it is demonstrated that UE grouping using the k-means clustering approach outperforms UE grouping using the sectoring approach.

c) Subsequently, a low-complexity joint subcarrier allocation and baseband precoder optimization is devised that assures QoS to all UEs at a faster convergence rate. It consists of an iterative algorithmic solution in which the subcarrier allocation and baseband precoder are adjusted iteratively to preserve the required QoS while minimizing inter-beam interference.

d) Additionally, the estimation of the optimal number of beams for long-term UAV-assisted communications is presented. The effect of solar panel size on the energy efficiency of UAV-assisted mmWaves communication is also investigated.

e) Finally, the performance of the UAV-assisted communication system at mmWaves is compared to that operating at sub-6 GHz, highlighting the limitation of backhaul power on fronthaul communication at sub-6 GHz versus that at mmWaves.

It is notable that, optimum UAV hovering system design for solar powered communication to the ground UEs at mmWaves, considered in the study, is the first basic design optimization. Accordingly, the aspects of UAV mobility and multi-UAV cooperation at mmWaves are not in the scope of current study.

5.1.2 Chapter Organization

The chapter organization is as follows. The system model is presented in Section 5.2. UE grouping and RF precoder design optimization problems are presented in Section 5.3. Subcarrier and baseband precoder optimization with QoS constraint are presented in Section 5.4. UAV battery design and solar panel design are discussed in Section 5.5. The simulation results are presented in Section 5.6, and the summary is presented in Section 5.7.

5.2 System Model

The UAV communication system model and the UAV power consumption model at mmWaves are presented in this section.

5.2.1 mmWave UAV Communication System Model

We consider a multi-user UMI scenario, where a UAV serves a total of K UEs. The UAV has a backhaul connectivity with a gNB situated at a 2D distance of $d_{UAV-gNB}$ m. The height of gNB is h_{gNB}. The UEs are single antenna devices with antenna gain G_r. The UEs on the ground are distributed in a circular area $\mathcal{A} \in \mathbb{R}^2$ with a radius $\mathcal{R}$ following the Cox point process. We assume the UAV hovers at a fixed position throughout the transmission duration for an energy-efficient mmWaves system. Besides, in order to boost fronthaul rates, UAV-to-UE path loss should be minimized. Therefore, UAVs are deployed close to UEs, i.e., above the center of $\mathcal{A}$ at h_U height, to lower the average UAV-to-UE distance during the entire communication period.

The UAV consists of N_B RF units for fronthaul communication and one RF unit for backhaul connection. Also, on the UAV we consider two set of uniform planar arrays (UPA), one for fronthaul transmission and one for backhaul transmission. One UPA of dimensions $\sqrt{N_t} \times \sqrt{N_t}$ is connected to N_B RF units in fronthaul to serve the UEs and the other UPA with dimensions $\sqrt{N_b} \times \sqrt{N_b}$ is connected to backhaul unit to generate pointed

backhaul link to the gNB. At gNB, $\sqrt{N_g} \times \sqrt{N_g}$ array panel is used for establishing backhaul link to the UAV. The response vector of an UPA at an azimuth angle ϕ and elevation angle θ is given as

$$\begin{aligned}\mathbf{a}_T(f,\phi,\theta) = \frac{1}{\sqrt{N_t}}\Bigg[1,\ldots,e^{\frac{-j2\pi d'}{\lambda_c}\frac{f}{f_c}\sin\theta[(m-1)\cos\phi+(n-1)\sin\phi]} \\ ,\ldots,e^{\frac{-j2\pi}{\lambda_c}\frac{f}{f_c}d'\sin\theta\left[(\sqrt{N_t}-1)\cos\phi+(\sqrt{N_t}-1)\sin\phi\right]}\Bigg]^T \in \mathbb{C}^{1\times N_t}\end{aligned} \tag{5.1}$$

where f/f_c is the beam squint factor at frequency f, d' is the inter element ULA spacing, λ_c is the carrier wavelength, and m and n indices represent the mth and nth antenna element, respectively, along the x-axis and y-axis of the UPA.

Due to shadowing from buildings, the air-to-ground links between the UE and the UAV are either LoS or NLoS links. In this work, we follow the 3GPP UMi street canyon LoS probability model given as [105]

$$\mathbb{P} = \prod_{a=0}^{b}\left[1-\exp\left(\frac{-h_U-\frac{(a+0.5)h_U}{b+1}}{2\omega^2}\right)\right] \tag{5.2}$$

where $b = \lfloor d_k\sqrt{\xi\varsigma}-1\rfloor$, d_k is the 2D distance between the UAV and the UE k, and description of ς, ξ, and ω are given in Table 5.1. Additionally, the path loss for LoS and NLoS link for the kth UE, at a 2D distance d_k from the UAV are obtained as [5]

$$\begin{aligned}PL_{los}(d_k) &= a_L + n_L 10\log_{10}(\sqrt{d_k^2+h_U^2}) + \mathcal{N}(0,\sigma_L^2)\ \text{[dB]} \\ PL_{nlos}(d_k) &= a_N + n_N 10\log_{10}(\sqrt{d_k^2+h_U^2}) + \mathcal{N}(0,\sigma_N^2)\ \text{[dB]}.\end{aligned} \tag{5.3}$$

Here, a_L and a_N are frequency dependent constants, n_L and n_N are path loss exponents, and σ_L^2 and σ_N^2 are shadowing variances respectively for LoS and NLoS links. Therefore, the linear path loss for kth UE is

$$\text{PL}_k = 10^{[\mathbb{P}PL_{los}(d_k)+(1-\mathbb{P})PL_{nlos}(d_k)]/10}. \tag{5.4}$$

The mmWave wideband channel exhibits frequency selective fading. Therefore, the total bandwidth B is divided into N_c narrowband channels. Further, the channel consists of $L_k \ll N_t$ multipath components (MPCs). Thus, the channel between the UAV and the kth UE over the nth subcarrier at frequency f_n is expressed as

$$\mathbf{h}_{k,n} = \sqrt{\frac{N_t}{L_k\text{PL}_k}}\sum_{l=1}^{L_k}\alpha_{k,n,l}\mathbf{a}_\mathbf{T}(f_n,\phi_{k,l},\theta_{k,l})^H \in \mathbb{C}^{1\times N_t} \tag{5.5}$$

where $\alpha_{k,n,l}$ is complex fading gain of lth multi-path component (MPC) over subcarrier n and $\phi_{k,l}$ and $\theta_{k,l}$ are angle-of-arrival (AoA) of lth MPC in azimuth and elevation plane, respectively, assumed to be uniformly distributed with angular spread of σ_T^{AS}. We assume that UAV has perfect knowledge of all UEs' CSI and positions.

5.2.2 Power Consumption Model

UAV power consumption comprises three main components: in transmission, in communication circuit board, and in UAV motion.

5.2.2.1 Power Consumed in Transmission

The transmission power in UAV is the total power required for data transmission, composed of the power consumed in fronthaul transmission P_T and the power consumed in backhaul communication P_B.

5.2.2.2 Power Consumption in RF Module

The RF transmitting module power consists of the power consumed in RF front end components like ADC/DAC, RF mixer, and local oscillator. We denote the collection of all these components as an RF transceiver having power consumption P_{RF}. Phase shifters connected to antenna elements are passive, and hence they have zero power consumption. In addition, the power amplifiers (PAs) in RF circuit boards are energy-hungry devices with efficiency η_{PA}. The power consumption values and quantities of all the components in an RF front end are listed in Table 5.2 [80]. Therefore, the total power consumption in a communication module is given as

$$P_C = \underbrace{P_T + P_B}_{\text{Transmission power}} + \underbrace{(N_B + 1)P_{RF} + \eta_{PA}(P_T + P_B).}_{\text{Power consumed in mmWave transmission module}} \tag{5.6}$$

Here the term $(N_B + 1)$ represents the total number of RF chains at the UAV (N_B for fronthaul and 1 for backhaul).

5.2.2.3 Power Consumption in UAV Motion

In this work we assume static UAV position hovering at height h_U. Air speed is zero during hovering and thrust balances the UAV weight force. Therefore, the total thrust is

$$T = g(m_1 + m_2 + m_3 + m_4) \tag{5.7}$$

Table 5.1: Some important variable description

Acronym	Description
$\mathbf{a_T}$	UPA response vector
B	Bandwidth
d_k	2D distance of UE k from the UAV
$d_{UAV-gNB}$	UAV to gNB 2D distance
f_c	Carrier frequency
f_n	Carrier frequency of nth subcarrier
G_r	Single antenna element gain of UE
G_0	Single antenna element gain of UPA
h_U	UAV height in meters
h_{gNB}	gNB height in meters
$\mathbf{h}_k$	UE to UAV channel of UE k
K	UE population
L_k	Total number of MPCs of kth UE
N_0	Noise one-sided power spectral density
N_c	Number of subcarriers
N_B	Number of RF chains/beams at UAV
N_b	Total number of antenna elements at UAV for backhaul
N_g	Total number of antenna elements at gNB for backhaul
N_t	Total number of antenna elements at UAV for fronthaul
PL_k	Linear path loss of UE k
R_0	Minimum UE rate (or QoS rate) requirements
$\alpha_{k,l}$	Small scale fading gain of lth MPC of kth UE
$\phi_{k,l}$	Azimuth AoA of lth MPC of kth UE
$\theta_{k,l}$	Elevation AoA of lth MPC of kth UE
Φ_j	Azimuth HPBW of jth beam
Θ_j	Elevation HPBW of jth beam
$\bar{\phi}_j$	Azimuth steering angle of jth beam
$\bar{\theta}_j$	Elevation steering angle of jth beam
$\mathbb{P}$	LoS probability of a link
κ	Ricean parameter
ξ	Ratio of area occupied by buildings to total area
ς	Mean number of building per unit area
ω	Building height distribution parameter
α'	Number of rotors in rotary winged UAV
β	Area of a spinning blade of UAV
ρ	Air density

Table 5.2: Power consumption of components in a RF chain.

Component	Notation	Power consumption
RF transceiver	P_{RF}	293 mW per RF chain [80]
Phase-shifter	P_{PS}	0 mW per antenna [106]
Power amplifiers	P_{PA}	P_T/η_{PA}
Power amplifier efficiency	η_{PA}	47% [107]

where m_1, m_2, m_3 and m_4, respectively, represent the masses of UAV body, battery, and solar panel, and payload, and g is the gravity. Therefore, the hovering power required for the rotary-wing UAV is [108]

$$P_{hover} = \frac{T^{3/2}}{\sqrt{2\alpha\rho\beta}} = \frac{g(\sum_{i=1}^{4} m_i)^{3/2}}{\sqrt{2\alpha'\rho\beta}} \tag{5.8}$$

where α is the number of of rotors, ρ is air density, β is the area of spinning blade.

5.3 UE Grouping and RF Precoder Design

We consider a two-stage hybrid precoder design. First, the RF precoder is designed based on UEs' geometric information, and then the rate performance of the system is optimized at the baseband level. This section focuses on the RF precoder design by grouping UEs. For this, we consider a sub-array hybrid precoder architecture in which each RF unit is connected to a set of non-overlapping antenna elements that generates a single steerable beam. UEs in each group are served over the wideband mmWave channel by employing OFDMA. Let $\mathcal{K}_j$ denote the set of UEs in group j, where $j = \{1, \ldots, N_B\}$.

Remark 5.1. *We demonstrated in Fig. 2.4(b) (Chapter 2) that the system energy is maximized when the beam is narrowest. This is due to the fact that highly directed beams require less power to maintain the same SNR. To that end, we adjust the beamwidth in this chapter to maximize the UAV's energy efficiency.*

Remark 5.2. *Furthermore, we observed in Fig. 3.8 (Chapter 3) that, even in the presence of inter-beam interference, the average long-run UE rate is maximum when the number of RF chains (equivalent to number of beams) equals the number of sectors. As a result, we divide UE into groups equal to the number of RF chains or beams N_B in this chapter.*

The UAV divides the UEs into $N_B = N_B^{k\text{-means}}$ groups using k-means clustering, and each group is served by one RF beam, (Fig. 5.1(a)). By activating the needed number

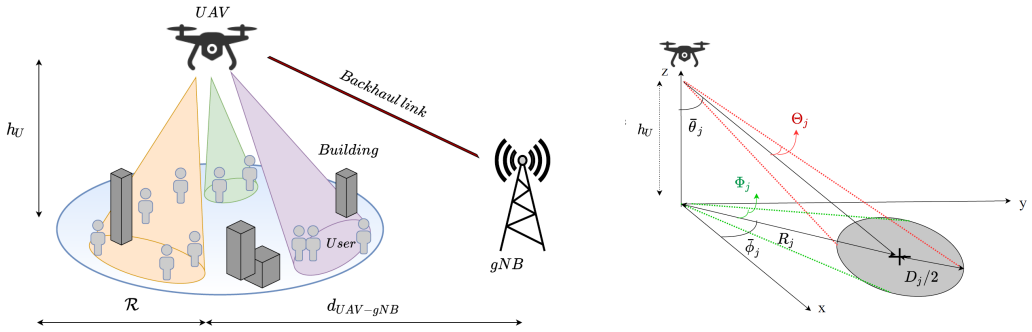

(a) (b)

Figure 5.1: (a) Illustration of UE grouping to partition UEs into $N_B^{k\text{-means}} = 3$ groups using k-means clustering. (b) Geometric illustration of steering angles and beamwidth in azimuth and elevation planes.

of antenna elements in the UPA, the beamwidth can be adjusted to optimize the coverage that is sufficient enough to cover the UEs in the group. Let $x_m \in \mathbb{R}^2$ denote the Cartesian coordinates of the mth UE. Then the maximum diameter $\mathcal{D}_j$ of the spot covering the $\mathcal{K}_j$ UEs of j^{th} group is

$$\mathcal{D}_j = \max_{m,n \in \mathcal{K}_j} (||x_m - x_n||_2). \tag{5.9}$$

Thus, the UAV refines each beam's azimuth and elevation beamwidth depending on the UE positions within in the group to focus maximum beam radiation towards the UEs (Fig. 5.1(b)). The half-power azimuth beamwidth Φ_j and elevation beamwidth Θ_j for jth beam are the set as

$$\Phi_j = \tan^{-1} \frac{\mathcal{D}_j/2}{\mathcal{R}_j};\ \Theta_j = \tan^{-1}\left(\frac{\mathcal{R}_j}{h_U}\right) - \tan^{-1}\left(\frac{\mathcal{R}_j - \mathcal{D}_j/2}{h_U}\right) \tag{5.10}$$

where $\mathcal{R}_j$ is the 2D distance of jth group center from the UAV.

$\sqrt{N_T} \times \sqrt{N_T}$ UPA is partitioned into $N_B^{k\text{-means}}$ subarrays of dimensions $\sqrt{N_j} \times \sqrt{N_j}$ such that $\sum_{j=1}^{N_{RF}} \sqrt{N_j} \times \sum_{j=1}^{N_{RF}} \sqrt{N_j} = \sqrt{N_T} \times \sqrt{N_T}$. The value of N_j is determined as follows [109]

$$N_j = \min\left(\left\lceil \frac{2.782}{\pi \sin(\max\{\Phi_j, \Theta_j\}) \cos(\tan^{-1} \frac{d_k}{h_U})} \right\rceil, N_{max}\right) \tag{5.11}$$

where N_{max} is the upper bound on the active number of antenna elements in a sub-array. The steering direction of jth beam in azimuth and elevation plane, respectively, are

$$\tilde{\phi}_j = \mathop{\mathbb{E}}_{l,k \in \mathcal{K}_j}(\phi_{k,l});\ \tilde{\theta}_j = \mathop{\mathbb{E}}_{l,k \in \mathcal{K}_j}(\theta_{k,l}). \tag{5.12}$$

However, the phase shifters connected to antenna elements are controlled by b bits. Therefore, a beam can be steered in some specified direction only. The possible the possible steering directions can range from the set $\mathcal{F} = \{2\pi i/2^b | i = 0, \ldots, 2^b - 1\}$. Therefore, the optimal steering directions for beam j in azimuth and elevation plane are

$$\bar{\phi}_j = \underset{\phi \in \mathcal{F}}{\text{argmax}} |\phi - \tilde{\phi}_j|; \ \bar{\theta}_j = \underset{\theta \in \mathcal{F}}{\text{argmax}} |\theta - \tilde{\theta}_j|. \tag{5.13}$$

Therefore, the analog precoding matrix $\mathbf{A}$ of the hybrid precoder is of the form

$$\mathbf{A} = \{\mathbf{a}^1, \ldots, \mathbf{a}^{N_B^k\text{-means}}\} \in \mathbb{C}^{N_T \times N_B^k\text{-means}}. \tag{5.14}$$

Here $\mathbf{a}^j \in \mathbb{C}^{N_T \times 1}$ is the RF weight vector of jth beam and is independent of frequency. For a beam steered at angle $(\bar{\phi}_j, \bar{\theta}_j)$ RF weights for the array are given by (5.15).

$$\mathbf{a}^j = \begin{cases} e^{-j\frac{2\pi}{\lambda_c}\frac{f_n}{f_c}d' \sin\bar{\theta}_j\left[(m-1)\cos\bar{\phi}_j + (n-1)\sin\bar{\phi}_j\right]} & \forall n, m \in \left[\left(\sum_{i=1}^{j-1}\sqrt{N_i}\right) + 1 : \sum_{i=1}^{j}\sqrt{N_i}\right], \\ 0 & \text{otherwise.} \end{cases} \tag{5.15}$$

5.4 Subcarrier and Baseband Precoder Design with QoS Constraint

5.4.1 Problem Formulation

In the proposed system model employing k-means clustering, the RF beams are steered in the direction of UE clusters, thus rendering them non-orthogonal. Additionally, the practical radiation pattern of a beam consists of sidelobes. Therefore, the UEs in group j served by beam j will experience side-lobe interference from the sidelobes of beam $i \neq j$ where $j = \{1, 2, \cdots, N_B\}$.

Let $\mathbf{B}_n = \text{diag}\{b_n^j\} \in \mathbb{C}^{N_B \times N_B}$ and $\mathbf{x}_n = \{x_n^j\} \in \mathbb{C}^{N_B \times 1}\ \forall$ denote the UAV baseband precoder and unit energy transmit signal at nth subcarrier, respectively. Here b_n^j and x_n^j denote the complex baseband weight and input signal, respectively, on nth subcarrier of jth RF unit. Then the received signal over nth subcarrier at UE k served by beam j can be written as

$$y_{k,n} = \underbrace{\mathbf{h}_{k,n}\mathbf{a}^j b_n^j x_n^j}_{\text{desired signal}} + \underbrace{\sum_{i=1, i\neq j}^{N_B} \mathbf{h}_{k,n}\mathbf{a}^i b_n^i x_n^i}_{\text{inter-user interference}} + z_{k,n} \tag{5.16}$$

where $z_{k,n}$ is complex Gaussian noise with distribution $\mathcal{N}(0, \sigma^2)$. The baseband precoder minimizes the inter-user interference effect at the transmitter end. A receive beamforming weight equivalent to a equalizer minimizes the inter-user interference at the UE. Let $u_{k,n}$ denote the linear equalizer of kth UE at nth frequency. Then the estimated signal of UE k is $\hat{y}_{k,n} = u_{k,n}^H y_{k,n}\ \forall k, n$. Subsequently, the signal-to-interference-plus-noise ratio $\Gamma_{k,n}^j$ of kth UE over the nth subcarrier served by beam j is represented as

$$\Gamma_{k,n}^j = \frac{|\mathbf{h}_{k,n}\mathbf{a}^j b_n^j|^2 G_r}{\frac{N_0 B}{N_c} + \sum_{i=1, i\neq j}^{N_B} |\mathbf{h}_{k,n}\mathbf{a}^i b_n^i|^2 G_r}. \tag{5.17}$$

Therefore, the data rate of kth UE over the nth subcarrier in jth beam is

$$r_{k,n}^j = \frac{B}{N_c}\log_2(1 + \Gamma_{k,n}^j). \tag{5.18}$$

In this work, we consider that the backhaul link operates at the same frequency as the fronthaul link. Since the backhaul link is aligned and narrow, we assume the UAV backhaul antenna panel gain $G_b \approx N_b G_0$ and the gNB backhaul antenna panel gain $G_g \approx N_g G_0$. Let R_k^j denote the instantaneous rate of a UE k served by beam j, given by

$$R_k^j = \sum_{n=1}^{N_c} \pi_{k,n}^j r_{k,n}^j \tag{5.19}$$

where the variable $\pi_{k,n}^j = 1$ if kth UE assigned nth subcarrier on jth beam; 0 otherwise. Moreover, the backhaul capacity should be at least equal to the fronthaul sum rate, i.e., $\sum_j \sum_{k\in\mathcal{K}_j} R_k^j$. Then the required backhaul power is

$$P_B = \frac{2^{\sum_j \sum_{k\in\mathcal{K}_j} R_k^j/B} - 1}{|h_B|^2 G_b G_g \mathrm{PL}_B / N_0 B} \tag{5.20}$$

where h_B and PL_B are the small scale fading channel and pathloss of backhaul link, respectively. Thus the value of P_B is a function of the instantaneous fronthaul rate that depends on the precoding, subcarrier allocation, and P_T. Additionally, given a limit on total communication module power P_{limit}, from (5.6) the power available for fronthaul transmission is

$$P_T = \frac{P_{limit} - (N_B + 1)P_{RF}}{1 + \eta_{PA}} - P_B. \tag{5.21}$$

We optimize the subcarrier and baseband precoders to maximize the sum throughput with the specified QoS requirement R_0, given N_B and the accompanying RF precoder

design. Therefore, the downlink sum rate optimization problem at the UAV is represented as

$$
\begin{aligned}
(\mathcal{P}1): \quad & \max_{\pi^j_{k,n},\mathbf{B}} \sum_{j=1}^{N_B} \sum_{k\in\mathcal{K}_j} \left(\sum_{n=1}^{N_c} \pi^j_{k,n} r^j_{k,n} \right) \\
\text{s.t.} \quad & C11: \sum_{k=1}^{K_s} \pi^j_{k,n} \leq 1,\ \forall n, j;\ C12: \pi^j_{k,n} \in \{0,1\},\ \forall k, n, j \\
& C13: \sum_{n=1}^{N_c} \pi^j_{k,n} r^j_{k,n} \geq R_0\ \forall k;\ C14: \sum_{n=1}^{N_c} \text{Tr}(\mathbf{B}_n \mathbf{B}_n^H) \leq P_T.
\end{aligned} \tag{5.22}
$$

In each group in an epoch, the subcarriers are allocated only to a subset of UEs $k \in \mathcal{K}_j$ that are not in complete outage. We define kth UE to be in complete outage if with unit power $\max_{n\in\mathcal{N}_c} \{\Gamma^j_{k,n}\} < \Gamma_{th}$. Here, Γ_{th} denote the threshold value. The above problem is non-convex since the objective function and constraint $C13$ are non-convex. $(\mathcal{P}1)$ can be solved used using alternating optimization method which iteratively solves for $\pi^j_{k,n}$ while fixing $\mathbf{B}$ and P_T, and vice versa, until convergence is obtained. However, this is a computationally intensive procedure and may not guarantee convergence. Additionally, the constraint $C14$ requires optimization of P_T. This is because, as given in (5.21), P_T is a function of P_B that depends on UE sum rate which in turn is an increasing function of P_T. Hence, P_B and P_T have positive covariance. As a result, to solve $\mathcal{P}1$ the value of P_T is estimated using golden-section search method such that sum rate is maximized while (5.21) holds. The starting value of P_T is chosen by assuming negligible power consumption in backhaul, i.e.,

$$
P_T = \frac{P_{limit} - (N_B + 1)P_{RF}}{1 + \eta_{PA}}. \tag{5.23}
$$

5.4.2 Proposed Subcarrier Allocation and Baseband Precoder Design

This subsection presents the proposed approach to find optimal subcarrier allocation, UAV baseband precoder design, and equalizer weights at the UEs to maintain QoS. The process is divided in two steps. Initially assuming zero inter-user interference, equal power per subcarrier, $\mathbf{B} = \sqrt{P_T/N_c N_B}\mathbf{I}_{N_B}$, and unity equalizers at UEs, subcarriers are allocated to the UEs to maximize the sum throughput while assuring minimum QoS to the UEs that are not in a complete outage. Next, baseband precoder and equalizer weights are estimated along with subcarrier reallocation in an iterative manner to maintain QoS.

The baseband precoder and equalizers are designed by converting the sum rate maximization problem using weighted MMSE (WMMSE) precoder. The cost function is used to reallocate subcarriers.

5.4.2.1 Part 1: Initial Subcarrier Allocation

Given $\{\mathbf{A}, N_B\}$, fixing $\{P_T\}$, $\mathbf{B} = \sqrt{P_T/N_c N_B}\mathbf{I}_{N_B}$, and unity equalizers at UEs in $\mathcal{P}1$, we perform an initial subcarrier allocation to maximize the sum rate while satisfying minimum QoS rate requirements of all UEs assuming zero inter-beam interference. To solve this problem we use a sub-optimum approach leveraging the combination of direct search and external point search that yields a sub-optimal solution close to the optimal solution. In this, first the subcarriers are allocated to maximize the sum rate by relaxing $C13$. This gives a solution that is not from the feasible set but acts as the initial point for the search. Thereafter, the subcarrier allocation is adjusted on UE-by-UE basis to satisfy constraint $C13$. The steps involved in are:

(i) With the consideration of $\mathbf{B} = \sqrt{P_T/N_c N_B}\mathbf{I}_{N_B} \in \mathbb{C}^{N_B \times N_B}$ and zero inter-user interference, we calculate $r^j_{k,n}\ \forall k, n, j$ using (5.17).

(ii) Because of zero inter-user interference assumption, subcarrier allocation in each beam is carried out independently. In beam j, each subcarrier is assigned to a UE with the best channel condition. Hence, the optimal UE assignment over nth subcarrier in jth beam is found as

$$\hat{k}_{n,j} = \underset{k \in \mathcal{K}_j}{\text{argmax}}\ r^j_{k,n}\ \forall n, j. \tag{5.24}$$

As a result, $\pi^j_{\hat{k}_{n,j},n} = 1$ and $\pi^j_{k,n} = 0\ \forall k \neq \hat{k}_{n,j}$.

(iii) Let $\mathcal{K}'_j \subset \mathcal{K}_j$ represent the set of UEs that violate constraint $C13$ from step (ii). We employ the error minimization method to allocate subcarriers on a UE-by-UE basis to all UEs $k \in \mathcal{K}'_j$ to satisfy $C13$ (unless the UE is in complete outage). The error function is defined for all $k \in \mathcal{K}'_j\ \forall n$ as [68]

$$E^j_{k,n} = \frac{r^j_{\hat{k}_{n,j},n} - r^j_{k,n}}{r^j_{k,n}}$$

where $\hat{k}_{n,j}$ is the UE that is initially assigned to nth subcarrier on jth beam from step (ii). The error is proportional to the reduction in overall sum rate.

(iv) The UE $k \in \mathcal{K}'_j$ that has minimum error is allocated a subcarrier, i.e., $\tilde{n} = \underset{n}{\text{argmin}}\ E^j_{k,n}$. It should be noted that during subcarrier reallocation, a subcarrier $\tilde{n}$ should not be reassigned to the UE k if it violates the minimum rate requirements of the UE originally allocated to $\tilde{n}$ subcarrier., i.e, if $R^j_{\hat{k}_{\tilde{n},j}} - r^j_{\hat{k}_{n,j},\tilde{n}} < R_0$, where $R^j_{\hat{k}_{n,j}} = \sum_{n=1}^{N_c} \pi^j_{\hat{k}_{n,j},n} r^j_{\hat{k}_{n,j},n}$ is the rate of optimal UE $\hat{k}_{n,j}$ over nth subcarrier on jth beam found using (5.24). If $R^j_k \geq R_0$ then $\mathcal{K}'_j = \mathcal{K}'_j/k$.

(v) Steps (iii) and (iv) are repeated until $\mathcal{K}'_j = \emptyset$ or subcarriers cannot be further reassigned.

(vi) Steps (ii) and (v) are repeated for all $j = \{1, \ldots, N_B\}$.

Remark 5.3. *In case $|\mathcal{K}_j| > N_c$, only N_c among $|\mathcal{K}_j|$ UEs with best channel conditions are allocated subcarriers fulfilling their QoS rate requirements while the remaining $|\mathcal{K}_j| - N_c$ UEs are considered in outage in that epoch.*

5.4.2.2 Joint Baseband Precoding and Subcarrier Reallocation

Now we iteratively design UAV baseband precoder $\mathbf{B}$ and UE equalizer weights $\mathbf{u}$ and reallocate the subcarriers. We begin with the knowledge of initial subcarrier allocation from section 5.4.2.1. Then at each iteration by relaxing C13 we estimate $\{\mathbf{B}, \mathbf{u}\}$ using WMMSE precoder to maximize the sum rate.

The steps to design baseband precoder design and equalizer weights using WMMSE are given in Algorithm 5.1. Let $k^*_{n,j}$ denote the optimal UE assignment over subcarrier n on beam j. For fixed $(\mathbf{A}_{RF}, \{\pi^j_{k^*_{n,j},n}\}_{\forall n,j})$, the optimal baseband precoders $\mathbf{B}$ and $\mathbf{u} = \{u^j_{k^*_{n,j},n}\}_{\forall n,j}$ that maximizes total rate are found by solving the given problem

$$\begin{aligned} (\mathcal{P}2): \quad & \max_{\mathbf{u},\mathbf{B}} \sum_{j=1}^{N_B} \sum_{n=1}^{N_c} r^j_{k^*_{n,j},n} \\ \text{s.t.} \quad & C21: \sum_{n=1}^{N_c} \text{Tr}(\mathbf{B}_n \mathbf{B}_n^H) \leq P_T \end{aligned} \tag{5.25}$$

Assuming Gaussian signaling, the rate of UE $k^*_{n,j}$ assigned on nth subcarrier beam in j is

$$r^j_{k^*_{n,j},n} = \log_2 \left(1 + {Z^j_{k^*_{n,j},n}}^{-1} \left| \mathbf{h}^*_{n,j,n} \mathbf{a}^j b^j_n \right|^2 \right) \tag{5.26}$$

where $Z^{j}_{k^*_{n,j},n}$ is the noise covariance on nth subcarrier from rest of the beams that is given by

$$Z^{j}_{k^*_{n,j},n} = \sigma^2 + \sum_{i \neq j} \left| \mathbf{h}_{k^*_{n,j},n} \mathbf{a}^i b^i_n \right|^2. \tag{5.27}$$

The MMSE receiver $u^{j}_{k^*_{n,j},n}$, is given as [91]

$$u^{j}_{k^*_{n,j},n} = \frac{\mathbf{h}_{k^*_{n,j},n} \mathbf{a}^j b^j_n}{Z^{j}_{k^*_{n,j},n} + \left| \mathbf{h}_{k^*_{n,j},n} \mathbf{a}^j b^j_n \right|^2}. \tag{5.28}$$

Applying MMSE receiver, the error at UE $k^*_{n,j}$ is

$$\begin{aligned} e^{j}_{k^*_{n,j},n} &= \mathbb{E}\left[(u^{j}_{k^*_{n,j},n} y^{j}_{k^*_{n,j},n} - x^j_n)(u^{j}_{k^*_{n,j},n} y^{j}_{k^*_{n,j},n} - x_j[n])^H \right] \\ &= \left(1 + Z^{j}_{k^*_{n,j},n}{}^{-1} \left| \mathbf{h}_{^*_{n,j},n} \mathbf{a}^j b^j_n \right|^2 \right)^{-1}. \end{aligned} \tag{5.29}$$

Now we transform the sum rate maximization problem $\mathcal{P}2$ into weighted sum-rate mean square error (WMMSE) minimization problem as [91]

$$\begin{aligned} (\mathcal{P}3): \quad & \min_{\mathbf{w},\mathbf{u},\mathbf{B}} \sum_{j=1}^{N_{RF}} \sum_{n=1}^{N_c} \left(w^{j}_{k^*_{n,j},n} e^{j}_{k^*_{n,j},n} - \log_2(w^{j}_{k^*_{n,j},n}) \right) \\ \text{s.t.} \quad & C31: \sum_{n=1}^{N_c} \text{Tr}(\mathbf{B}_n \mathbf{B}_n^H) \leq P_T. \end{aligned} \tag{5.30}$$

Here, $w^{j}_{k^*_{n,j},n}$ denote the positive weight associated with the $k^*_{n,j}$ UE assigned on nth subcarrier in jth RF unit. Problem $\mathcal{P}3$ is convex in all the optimization variables. Hence, the Lagrangian of $\mathcal{P}3$ is given as

$$\mathbf{L} = \sum_{j=1}^{N_{RF}} \sum_{n=1}^{N_c} \left(w^{j}_{k^*_{n,j},n} e^{j}_{k^*_{n,j},n} - \log w^{j}_{k^*_{n,j},n} \right) + \nu \left(\sum_{n=1}^{N_c} \text{Tr}(\mathbf{B}_n \mathbf{B}_n^H) - P_T \right) \tag{5.31}$$

where ν is the positive Lagrangian multiplier. Therefore, solving for one variable by taking partial derivative of (5.31) with respect to that variable, while keeping other variables fixed, gives a local optimal. Therefore, the optimal weights are given as

$$w^{j}_{k^*_{n,j},n} = \frac{1}{e^{j}_{k^*_{n,j},n}}. \tag{5.32}$$

Substituting the values of the equalizers $u^j_{k^*_{n,j},n}$, error $e^j_{k^*_{n,j},n}$, and weights $w^j_{k^*_{n,j},n}$ in $\mathcal{P}3$ we have the equivalence as

$$(\mathcal{P}4): \quad \max_{\mathbf{B}} \sum_{j=1}^{N_{RF}} \sum_{n=1}^{N_c} \log_2 \left(1 + \frac{\left| \mathbf{h}_{k^*_{n,j},n} \mathbf{a}^j b^j_n \right|^2}{\sigma^2 + \sum_{i \neq j} \left| \mathbf{h}_{k^*_{n,j},n} \mathbf{a}^i b^i_n \right|^2} \right) \tag{5.33}$$

$$\text{s.t.} \qquad C31.$$

where $\mathcal{P}4$ is convex in $b^j_n \ \forall j, n$. Consequently, we solve it using KKT to obtain

$$b^*_j[n] = \frac{w^j_{k^*_{n,j},n} (u^j_{k^*_{n,j},n})^H \mathbf{h}_{k^*_{n,j},n} \mathbf{a}^j}{\nu + \sum_i w^i_{k^*_{n,i},n} |{u^i_{k^*_{n,i},n}}^H \mathbf{h}_{k^*_{n,i},n} \mathbf{a}^j|^2} \tag{5.34}$$

where ν is the Lagrangian multiplier corresponding to C31. Substituting value of $b^*_j[n]$ in C31, we have

$$\sum_{n=1}^{N_c} \sum_{j=1}^{N_{RF}} \frac{\left| w^j_{k^*_{n,j},n} (u^j_{k^*_{n,j},n})^H \mathbf{h}_{k^*_{n,j},n} \mathbf{a}^j \right|^2}{\left(\nu + \sum_i w^i_{k^*_{n,i},n} |{u^i_{k^*_{n,i},n}}^H \mathbf{h}_{k^*_{n,i},n} \mathbf{a}^j|^2 \right)^2} \leq P_T. \tag{5.35}$$

Here, (5.35) is a decreasing function of ν and is solved using numerical methods. Therefore, if $\sum_{n=1}^{N_c} \text{Tr}\{\mathbf{B}_n(\nu=0)\mathbf{B}_n(\nu=0)\}^H \leq P_T$, then $\mathbf{B}^*_n = \mathbf{B}_n(\nu=0)$; otherwise ν^* is found using bisection search. The steps to find baseband precoder design and equalizer of UE are given in Algorithm 5.1.

It is notable that solving for $\{\mathbf{B}, \mathbf{u}\}$ using Algorithm 5.1 might violate minimum QoS rate constraint C13 of some UEs. The use of penalty-based WMMSE precoder design optimization is one technique to ensure C13 [110]. However, this approach has an extremely slow convergence rate. Therefore, we propose to jointly reallocate subcarriers to UEs along with the re-design of $\{\mathbf{B}, \mathbf{u}\}$ design such that QoS of UEs is maintained. The steps are listed in Algorithm 5.2, which has a faster rate of convergence.

In Algorithm 5.2 we traverse each subcarrier one-by-one. On nth subcarrier, we find the set of UEs $\mathcal{K}_n = \{k^*_{n,j} | R^j_{k^*_{n,j}} > R_0, \ \forall j\}$. If $\mathcal{K}_n \neq \emptyset$ then we find the cost function at nth subcarrier defined as

$$c_{k^*_{n,j},n} = R^j_{k^*_{n,j}} - r^j_{k^*_{n,j},n} \ \forall k^*_{n,j} \in \mathcal{K}_n. \tag{5.36}$$

Thereafter, we find the UE that has the highest cost using is selected using the relation

$$k'_n = \underset{k^*_{n,j} \forall j}{\text{argmax}} \ c_{k^*_{n,j},n}. \tag{5.37}$$

Algorithm 5.1 WMMSE precoder

Input: $N_{RF}, {\pi^j_{k^*_{n,j},n}}^*, \mathbf{A}_{RF}, \mathbf{h}_{k^*_{n,j},n}\ \forall k, j, n$
Output: $\mathbf{B}_n$ and $u^j_{k^*_{n,j},n}$
Initialize $\mathbf{B}_n = \mathbf{I}_{N_B}\sqrt{P_T/(N_c N_{RF})}$
do
    Find $u^j_{k^*_{n,j},n}$ using (5.28) $\forall j, n$
    Find $w'_{k^*_{n,j},j}[n] \leftarrow w^j_{k^*_{n,j},n}$ using (5.32) $\forall j, n$
    Find ν using (5.35)
    Find b^j_n using (5.34) $\forall j, n$
    Update $w^j_{k^*_{n,j},n}$ (5.32) $\forall j, n$
while $\left|\sum_j \log\det(\sum_n w'^j_{k^*_{n,j},n}) - \log\det(\sum_n w^j_{k^*_{n,j},n})\right| \leq \epsilon$

For the UE k'_n we set $\pi^j_{k'_n,n} = 0$ if and only if $c_{k^*_{n,j}} > R_0$; otherwise go to next subcarrier. We also update $\mathcal{K}_n, R^j_k$ and re-design $\{\mathbf{B}_n, \mathbf{u}_n\}_{\forall n}$ before moving to the next subcarrier. This procedure is repeated over all the N_c subcarriers till the convergence is achieved. The stopping criteria of this algorithm is defined when the $R^j_k > R_0\ \forall k$ or each subcarrier has at most one UE assigned to it and hence, further subcarrier reallocation is not possible. If all the subcarriers have maximum one UE assigned on it and $\mathcal{K}_n \neq \emptyset$, then the process is stopped even though $C13$ is not fulfilled for some of the UEs.

Remark 5.4. *In Algorithm 5.2, the WMMSE method to estimate $\{\mathbf{B}_n, \mathbf{u}_n\}_{\forall n}$ is executed at most N_B times per subcarrier. So, $\{\mathbf{B}_n, \mathbf{u}_n\}_{\forall n}$ are estimated a maximum of $N_c N_B$ times.*

5.4.3 Complexity Analysis

The complexity of k-means clustering for K UEs is $\mathcal{O}(K^2)$. The subcarrier allocation design in Section 5.4.2.1 requires $\mathcal{K}_j N_c$ comparisons in step (ii) , $(\mathcal{K}_j - 1)N_c$ additions and $(\mathcal{K}_j - 1)N_c$ multiplications in step (iii) to find error function, and $2N_c^2$ comparisons for subcarrier allocation in step (iv). Steps (ii)-(iv) are executed for $j = \{1, \ldots, N_B\}$. Therefore, the total complexity of subcarrier allocation is $\mathcal{O}(\sum_{j=1}^{N_B}(2(\mathcal{K}_j - 1)N_c + \mathcal{K}_j N_c + 2N_c^2))$. The dominant computational term in WMMSE precoder design results from the multiplication of $\mathbf{h}_{k^*_n,n}$ and $\mathbf{a}^{j^*}$ terms for all the beams. Let ζ_I denote the iterations required for convergence of Algorithm 5.1. Then the total complexity for WMMSE precoder is $\mathcal{O}(\zeta_\eta \zeta_I N_T N_B N_c^2)$. Further, in Algorithm 5.2 the number of iterations of con-

Algorithm 5.2 Joint subcarrier allocation and baseband precoder design with QoS constraints

Input: Analog precoder, N_c, $\{\mathbf{h}_{k,n}\}_{\forall n,k}$, N_{RF}, R_0, K, P_T
Output: $\{\pi^j_{k,n}\}^*$, $\mathbf{B}_n$, $u^j_{k^*_{n,j},n}$ $\forall k, n, j$
Initially assume zero inter-beam interference
Initialize $\mathbf{B}_n = \mathbf{I}_{N_B}\sqrt{P_T/(N_c N_{RF})}$
Allocate subcarriers using steps in 5.4.2.1
Find $\mathbf{B}_n$ and $u^j_{k^*_{n,j},n}$ using Algorithm 5.1
Update $r^j_{k,n}$ $\forall b$ and R^j_k $\forall k$
do
    for $n = 1$ to N_c **do**
        Find $\mathcal{K}_n = \{k^*_{n,j} | R^j_{k^*_{n,j}} > R_0,\ \forall j\}$
        while $\mathcal{K}_n \neq \emptyset$ **do**
            Find $c_{k^*_{n,j}}$ $\forall j$ using (5.36)
            Find k'_n using (5.37)
            $\pi^j_{k'_n,n} \leftarrow 0$ iff $c_{k^*_{n,j}} > R_0$
        end while
        Update $r^j_{k,n}$ $\forall k, j, n$ and R^j_k $\forall k$
        Re-design $\mathbf{B}_n$ and $u^j_{k^*_{n,j},n}$ $\forall j$ using Algorithm 5.1
    end for
while stopping criteria is satisfied

vergence is limited to $\zeta_P = N_c N_B$. Therefore, the overall complexity of proposed joint subcarrier and baseband precoder design in Algorithm 5.2 is $\mathcal{O}(\zeta_P \zeta_I N_T N_B N_c^2)$.

5.5 UAV Solar Panel Design

In addition to optimal UE grouping and baseband signal processing, the UAV hardware also impacts the overall energy efficiency of the system. To sustain UAV operation for a longer duration we consider solar energy harvesting. When there is no solar insolation (eclipse mode), the UAV payload consists of a battery that supplies backup power. When solar insolation exceeds the minimum needed level, the battery is recharged using solar panels. Let the solar insolation is available for a duration of T_s hours. During eclipse mode of T_c duration the battery sustains the UAV operation. It is worth noticing that solar panel has weight that increases UAV hovering power thereby reducing the energy

efficiency of the system. This section describes the design of the UAV solar panel for a sustainable long-term UAV operation.

The solar photovoltaic (PV) system consists of a PV array composed of solar panels connected in series and parallel combinations and a maximum power point tracker between the battery and the PV array to regulate the solar energy. The foremost requirement to design a PV system is to estimate the total load requirement. During the the solar insolation period T_s, the PV system charges the battery as well as supports the UAV operation. Let C_B denote the battery capacity in amp-hour and μ_c be the battery charging rate. Then, the total watt-hours requirement from solar panels is

$$T_{WH} = \frac{C_B}{\mu_c} + (P_C + P_{hover})T_s. \tag{5.38}$$

Thus, UAV hovering power consumption P_{hover} from (5.8) is

$$P_{hover}(W_{UAV}) = \frac{W_{UAV}^{3/2}}{\sqrt{2g\alpha'\rho\beta}} \tag{5.39}$$

where the total UAV weight given as

$$W_{UAV} = (W_B + W_{PV} + W_0)\text{ kg} \tag{5.40}$$

Here, W_B is battery weight, W_{PV} is PV array weight, and W_0 is the sum of weight of the different components of UAV hardware units like servomotor, engine, and RF circuit as listed in Table 5.3. It is notable that P_{hover} is function of W_{PV}. On the other hand, the value of W_{PV} depend on P_{hover}. Therefore, estimating solar panel size is an iterative process which is presented in Algorithm 5.3. The calculation of battery weight W_B and solar panel weight W_{PV} follows.

5.5.1 Battery Weight

During eclipse mode, the total UAV power consumption is $P_{Tot} = P_C + P_{hover}$ W. Let μ_d denote the battery discharging rate, V_u denote the operating voltage. Then, for the battery to support UAV operation during eclipse mode we have

$$C_B\mu_d V_u = T_c P_{Tot} \Rightarrow C_B \quad = T_c P_{Tot}/(\mu_d V_u). \tag{5.41}$$

A battery of capacity C_B is made up of small cells of capacity C_b, i.e., $C_B = \mathcal{N}_b C_b$, where $\mathcal{N}_b$ is the number of cells. With per unit battery weight W_b, the total battery weight is

$$W_B = m_2 g = \mathcal{N}_b W_b. \tag{5.42}$$

Algorithm 5.3 Solar panel design

1: Input: $\mu_d, \mu_c, \eta_s, T_c, T_s, \mathcal{N}_b$, and C_B
2: Output: $\mathcal{N}_b$ and $\mathcal{N}_{ser}$
3: Initialize $\mathcal{N}_{ser} = 1$, $P_0 = \infty$, and $P_{hover} = 0.2818$
4: **while** $|P_{hover} - P_0| < 0.0001$ **do**
5: $P_0 \leftarrow P_{hover}$
6: Find N_{ser} using (5.44)
7: Calculate W_{PV}
8: Update P_{hover} by using (5.40) and (5.45) in (5.39)
9: **end while**

Table 5.3: UAV design specifications

Component	Quantity	Unit weight
Li-ion battery (W_b)	N_b	0.0465 kg [111]
Solar cell (W_S)	$N_{ser} \times N_{parall}$	0.0065 kg [112]
Servomotor	4	0.0098 kg [113]
Main engine	1	0.055 kg [113]
RF circuit	2	0.026 kg [113]

5.5.2 Solar Panel Weight

Number of solar cells in parallel N_{parall} depends on the voltage rating of a solar cell V_s, voltage rating of the battery V_b, and the voltage rating of the UAV V_u. Therefore,

$$\mathcal{N}_{parall} = \lceil \frac{\max(V_b, V_u)}{V_s} \rceil \tag{5.43}$$

The number of solar cells in series $\mathcal{N}_{ser}$ depends on UAV load and the available radiation. Let the average radiation level per solar cell during solar insolation hours be I_s W/m^2/hr, charging efficiency of PV array be η_s, and per unit area of a solar cell be A_s. Then, the number of solar panels in series N_{ser} required to satisfy estimated demand is found as

$$\mathcal{N}_{ser} = \left\lceil \frac{\text{Total watt-hour required}}{\text{Watt-hour produced per cell}} \right\rceil = \left\lceil \frac{T_{WH}}{A_s I_s T_s \eta_s} \right\rceil. \tag{5.44}$$

Therefore, if W_S is the unit solar cell weight, then the total weight of the PV array is

$$W_{PV} = m_3 g = \mathcal{N}_{ser} \mathcal{N}_{prarall} W_S. \tag{5.45}$$

5.6 Results and Discussion

This section presents the numerical results and discussion of the various results to study the proposed system model. The results are generated in MATLAB using Monte Carlo simulations. UEs are distributed using the Cox point process over a circular area of radius $\mathcal{R} = 100$ m. The value of other system parameters considered in the system simulation setup are given in Table 5.4. The analysis for both mmWaves and sub-6 GHz range are carried out. The superscript 'mm' denotes the mmWave parameter, and the 'sub' denotes sub-6 GHz parameters.

5.6.1 Sectorization versus k-means Clustering at mmWaves

Let $\sigma_{spread} = 360^o/\chi$ represent the angular spread of the UEs over $\mathcal{A}$, where, $\chi \in (1, 360)$ is the skewness parameter. When $\chi = 1$, the UEs are uniformly distributed over 360^o; when $\chi = 360$ the UEs are confined to an angular area of 1^o and the skewness is maximum.

Further, for serving a number of UEs which is greater than the number of RF chains at

Table 5.4: Simulation parameters

Parameter	Value	Parameter	Value
N_c	64	K	30
f_c	5 GHz, 28 GHz	N_0	-174 dBm/Hz
B^{mm}	400 MHz	B^{sub}	20 MHz
N_t^{mm}	64×64	N_t^{sub}	12×12
N_b^{mm}	8×8	N_b^{sub}	2×2
N_g^{mm}	8×8	N_g^{sub}	2×2
η_{PA}^{mm}	47% [107]	η_{PA}^{sub}	60% [114]
κ^{mm}	12.6 dB	κ^{sub}	0 dB
h_U	100 m	$d_{UAV-gNB}$	400m
h_{gNB}	30 m	ς	500 [115]
R_0	$\{1, 2, 5, 10, 20\}$ Mbps	N_B^{max}	$64/N_B$
ξ	0.3 [115]	ω	15 [115]
α'	4 [98]	β	0.045 m^2 [98]
ρ	1.225 kg/m^3 [98]	C_b	2000 mAh
A_s	125×125 mm^2	I_s	1.37 KWH/m^2
μ_d	80%	μ_c	20%
V_s	6 V	V_u	12 V
V_b	12 V	η_s	22%

the UAV, we compare the proposed UE grouping using k-means with the sector based UE grouping scheme in [31]. To form identical sectors, we the place UAV at the center of the area $\mathcal{A}$. In [31] it is shown that the lateral projection of a 3D beam can be approximated close to a sector formation. Therefore, for the sectorization of an area, we consider that each RF beam covers a single sector. Subsequently, the area $\mathcal{A}$ having total K UEs is divided into sectors equal to the number of RF beams $N_B = N_B^{\text{sector}}$ at the UAV, as shown in Fig. 5.2. Therefore, the half-power azimuth beamwidth Φ and half-power elevation beamwidth Θ are equal for all the beams and are given as

$$\Phi = \frac{360^o}{N_B^{\text{sector}}};\ \Theta \ = \tan^{-1}\left(\frac{\mathcal{R}}{h_U}\right) - \tan^{-1}\left(\frac{\mathcal{R}-\mathcal{R}_0}{h_U}\right) \tag{5.46}$$

where $\mathcal{R}$ is radius of area $\mathcal{A}$ and $\mathcal{R}_0$ is the interior radius beyond which no beam coverage can be extended, as shown in Fig. 5.2. Hence, the $\sqrt{N_T} \times \sqrt{N_T}$ UPA is divided into N_B^{sector} non-overlapping subarrays of equal dimensions $\sqrt{N_e} \times \sqrt{N_a}$, where N_e and N_a denote the number of active antenna elements in elevation and azimuth plane, respectively. The values of N_e and N_a are determined as follows [109]:

$$\begin{aligned} N_e &= \min\left(\left\lceil \frac{2.782}{\pi \sin(\Theta)\cos(\tan^{-1}(d_k/h_U))}\right\rceil, \frac{N_T}{N_B^{\text{sector}}}\right) \\ N_a &= \min\left(\left\lceil \frac{2.782}{\pi \sin(\Phi)\cos(\tan^{-1}(d_k/h_U))}\right\rceil, \frac{N_T}{N_B^{\text{sector}}}\right). \end{aligned} \tag{5.47}$$

Consequently, steering directions of jth beam in azimuth and elevation plane, respectively, are

$$\bar{\phi}_j = \frac{1}{2}\frac{360^o}{\Phi} + (j-1)\frac{360^o}{\Phi};\ \bar{\theta}_j \ = \tan^{-1}\left(\frac{\mathcal{R}/2}{h}\right). \tag{5.48}$$

The analog precoding matrix $\mathbf{A}$ of the hybrid precoder is obtained by substituting these values in (5.15).

Remark 5.5. *The sectorization scheme considered in this chapter assume number of sectors S equal to number of beams N_B, each generated from a RF unit. Therefore, unlike in Chapter 2 and Chapter 3, round robin scheduling is not required.*

Let $\Delta G_R = G_R^{k\text{-means}} - G_R^{\text{sector}}$, where $G_R^{k\text{-means}}$ and G_R^{sector} respectively denote the geometric mean rate achieved with UE grouping using k-means clustering and sectoring method. Geometric mean is given as $G_R = (\prod_{j=1}^{N_B}\prod_{k\in\mathcal{K}_j} R_k^j)^{(1/K)}$.

Fig. 5.3(a) shows the variation of ΔG_R as a function of skewness parameter χ for different number of RF units N_B at the UAV. We observe that the value of ΔG_R increases

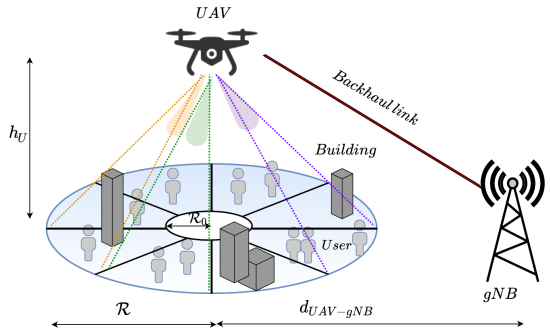

Figure 5.2: Illustration of UE grouping by partitioning the area into $N_B^{\text{sector}} = 8$ sectors with each sector served by one RF beam.

with skewness since all of the UEs are concentrated over a smaller area. In the sectoring approach, the closely located UEs are served by number of beams $N'_B < N_B$ that have UEs in corresponding sectors. Therefore, it is not able to exploit full spatial multiplexing gain. On the other hand, the proposed UE grouping with k-means clustering uses full degree of spatial multiplexing by dividing the UEs into the available number of beams. It is notable that, in k-means clustering the number of beams N_B decides total number of UE groups, whereas in sectoring N_B decides the total number of sectors. Moreover, the adjustable beamwidth and beam steering with k-means clustering method allows to direct maximum energy and beam towards the UEs to maximize the sum rate. Thus, sectoring approach is not suitable for mmWave UAV communications.

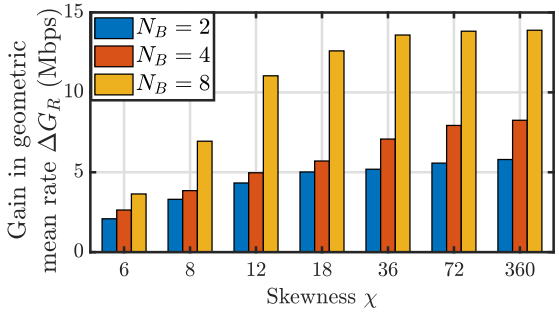

Figure 5.3: Plot of gain in geometric mean rate ΔG_R achieved by using k-means clustering over sectoring approach at mmWaves, given $P_{limit} = 5$ W and $N_B = N_B^{k\text{-means}} = N_B^{\text{sector}}$.

5.6.2 Performance of Proposed Joint Subcarrier and Baseband Precoder Algorithm

We compare the performance of the proposed joint subcarrier optimization design method, named as 'Proposed based design', over a benchmark method, which we call 'Penalty based design' [110]. In penalty based method subcarrier allocation and baseband precoder design occurs separately. Subcarrier allocation occurs using error based method as given in Section 5.4.2.1, and baseband precoder and equalizers are estimated using penalty based WMMSE optimization to maintain QoS. Penalty based design optimizes the baseband precoder such that it increases the rate of all UEs that have $R_k < R_0$ while decreasing the rate of UEs having $R_k > R_0$, so that the sum rate is maximized and the UEs in bad channel conditions achieve $R_k > R_0$. In contrast, joint subcarrier and baseband method (Algorithm 5.2) achieves QoS by removing a UE k'_n (cf. (5.37)) that has $R_k \gg R_0$ on a subcarrier and allocating it to another UE. Therefore, as shown in Fig. 5.4(a), joint subcarrier and baseband method results in proportional rate allocation among the UEs. Furthermore, as shown in Fig. 5.4(b), the number of iterations required for convergence of WMMSE precoder for penalty based design is quite high.

Besides, we first designs an RF precoder followed by joint subcarrier allocation and baseband precoder optimization. In contrast, works in the contemporary literature [116] first assign subcarriers and then schedule UEs using joint RF and baseband precoding to maximize sum throughput. Therefore, as a benchmark comparison we consider a system in which UEs are assigned subcarriers while meeting a minimum QoS constraint, and then

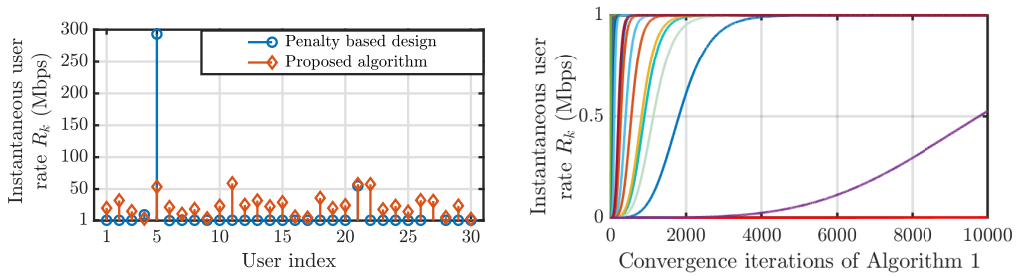

(a) (b)

Figure 5.4: (a) Comparison of UE rates achieved with proposed joint subcarrier and baseband design algorithm and penalty based design algorithm at mmWaves. (b) Illustration of the convergence of rate of UEs with penalty based design algorithm. Here, rate convergence of only those UEs is shown that initially had $R_k^j < R_0$.

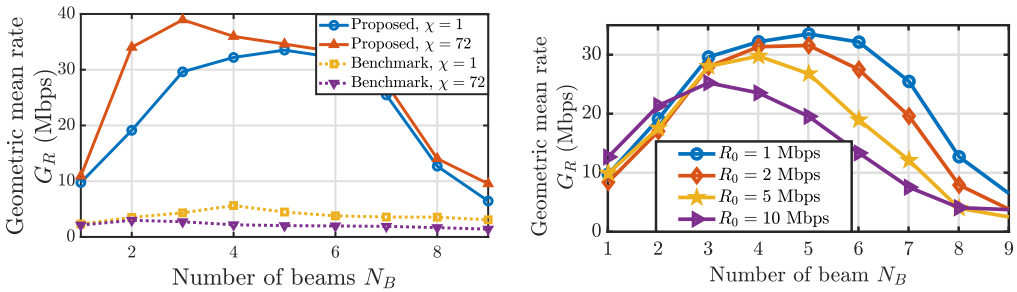

Figure 5.5: (a) Performance comparison of the proposed subcarrier and precoder algorithm over the benchmark scheme [29] at mmWaves, given $P_{limit} = 5$ W. (b) Illustration of geometric mean rate $\bar{R}$ as a function of number of beams N_B at mmWaves, given $P_{limit} = 5$ W, and $\chi = 1$.

RF and baseband precoders are optimized to minimize inter-user interference. Additionally, after precoding optimization power allocation is adjusted to maintain UE QoS [29]. Fig. 5.5(a) shows that our proposed subcarrier allocation and precoding scheme offers a significantly higher G_R than the benchmark scheme over different values of χ. This is because in a benchmark system, the UE with the best channel receives the maximum rate while the rest of the UEs receive the minimum rate, resulting in poor UE fairness G_R.

5.6.3 Optimal N_B Selection at mmWaves

As the number of beams increases, the power per beam decreases, and the RF power waste increases as given by (5.6). On the other hand, an increasing number of beams allows enhanced spatial multiplexing and narrow beams of higher directivity to cover the same set of UEs. As a result, the power requirements for UAVs and the achievable rates at mmWaves depend on N_B. Given P_{limit}, G_R is a concave function of N_B, as seen in Fig.

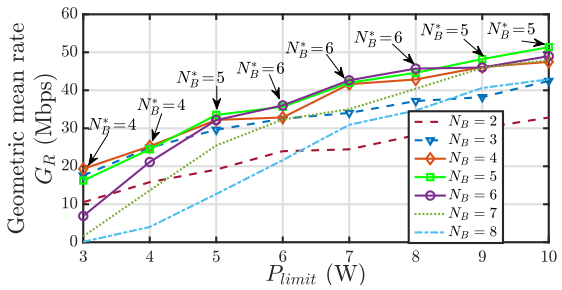

Figure 5.6: Plot of optimal N_B^* value as a function of available power P_{limit} for transmission module at UAV at mmWave range for $\chi = 1$.

5.5(b). Thus, there exists an optimal number of beams that provide the best performance while ensuring that all UEs receive minimum rate support. We estimate optimal N_B^* in this chapter by solving $\mathcal{P}1$ for different values of N_B. The value of N_B determines the number of UE groups that can be formed and the RF precoder design that accompanies it, as discussed in Section 5.3. Subcarrier allocation and baseband precoder are designed as described in Section 5.4.2 for each value of N_B. Furthermore, we investigate the optimal number of beams selection at UAV using the geometric mean rate measure. The choice of N_B is also influenced by R_0. The value N_B^* drops as R_0 is increased.

Further, Fig. 5.6 shows that for a given value of N_B, the value of G_R increases as P_{limit} increases, which is quite intuitive. On the other hand, the optimal N_B^* is a non-linear function of P_{limit}. To this end, operating at the optimal number of RF units N_B^* for maximum performance gain is crucial for a long-term UAV operation.

5.6.4 Analysis of Solar Panel Design at mmWaves

We also investigate the solar design aspects for a comprehensive view. As discussed in Section 5.5, the weight of a UAV increases with the number of solar cells, thus requiring more hovering power that corresponds to an increased solar panel size to sustain UAV operation. This is illustrated in Fig. 5.7 (a). We set $P_{Tot} = 5$ W, $T_s = 8$ hours, $T_c = 16$ hours for this simulation result, and the remainder of the design parameters are listed in Table 5.4. Fig. 5.7(b) shows the reduction in energy efficiency during eclipse mode because of additional weight of solar panel that increase P_{hover}, and hence resulting in reduced power available for the communication module. The curves in Fig. 5.7(b) are not

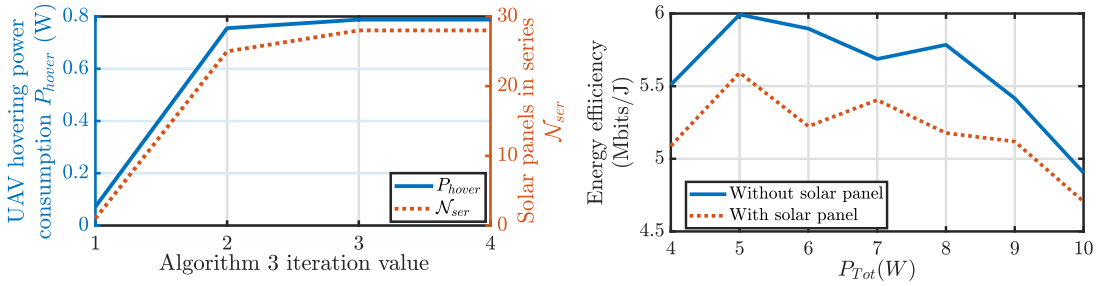

(a) (b)

Figure 5.7: (a) Convergence of P_{hover} and $\mathcal{N}_{ser}$ when $P_{Tot} = 5$ W. (b) Illustration of energy efficiency of UAV with and without considering solar panels weight optimization.

smooth because the number of solar panels is an integer variable. Also, as shown in Fig. 5.7(b) UAV is energy efficient when it is operated at $P_{Tot} = 5$ W.

5.6.5 UAV Communication Performance Comparison at Sub-6 GHz Versus at mmWaves

We also study the UAV performance and power requirements at the sub-6 GHz range for a comprehensive analysis. In simulations, we keep same antenna aperture for both the sub-6 GHz and mmWave systems. Hence, when $N_t^{mm} = 64 \times 64$ at mmWaves then $N_t^{mm} = 12 \times 12$. Also, 3GPP new radio (NR) defines a sector of $60^o \sim 65^o$ beamwidth in sub-6 GHz range. Therefore, in this work we consider $N_B^{sub} = 6$.

Notably, higher frequencies allow packaging of many antenna elements, thereby providing high beam gain and reduced transmit power. Moreover, a dedicated antenna panel with a large number of antenna elements is used at mmWaves to generate a pointed backhaul link. Along with that, mmWave operation offers bandwidth of around 400 MHz. As a result, the backhaul power at mmWaves is significantly less, on the order of mW. Consequently, more power is available for fronthaul transmission. In contrast, sub-6 GHz allows a small number of antenna elements resulting in low beam gain and thus, requiring high transmit power. Additionally, sub-6 GHz requires high power in backhaul P_B (Fig. 5.8) and thus reduced power available for fronthaul communication. Therefore, as shown in Fig. 5.8, the geometric mean rate G_R is higher at mmWaves than at sub-6 GHz range for the same power budget P_{limit}. Further, the value of P_B limits the overall fronthaul rate at sub-6 GHz. For example, when the total backhaul rate is 0.4 Gbps in sub-6 GHz range, P_B is as high as 8.45 W.

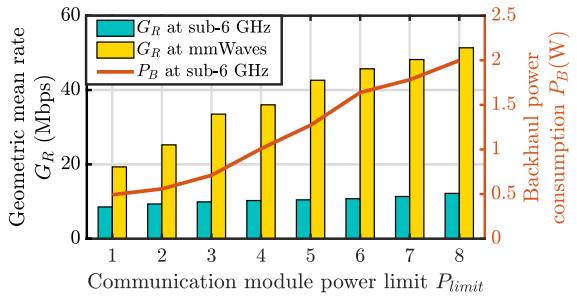

Figure 5.8: Comparison of $\bar{R}$ at sub-6 GHz and mmWaves at the UAV as a function of P_{limit} and illustration of P_B at sub-6 GHz. Here, $\chi = 1$, $R_0 = 1$ Mbps, $N_B^{sub} = 6$, and $N_B^{mm} = N_B^*$ (the optimal value that gives best performance at mmWaves).

5.7 Summary

This chapter has demonstrated that low-altitude UAVs serving multiple UEs via OFDMA at mmWaves offer more than double the rates achieved at sub-6 GHz frequency for the same UAV power budget. This gain is due to increased gain from large antenna arrays and high bandwidth at mmWaves. It is also shown that grouping UEs using k-means clustering and adjusting beam coverage to target maximal radiation on the UEs is superior to sectorizing the area from both rate and energy efficiency perspective.

Accordingly, an RF precoder for the sub-array hybrid precoder architecture is designed. A combined subcarrier and baseband precoding technique is also proposed for the sub-array hybrid precoding architecture. It has a faster convergence rate and provides fair rate allocation to the UEs while meeting the minimum rate guarantee. To design baseband beamforming weights and equalizers, WMMSE method has been used to reduce inter-beam interference. It is also verified that with a given power budget, increasing the number of RF chains does not necessarily increase the system performance as the associated power waste in the RF circuitry increases. Moreover, the number of beams should be optimized for a sustainable operation for energy-constrained UAV-assisted communications at mmWaves. Finally, aiming at long-term UAV-assisted communications at mmWaves, the battery capacity and solar panel have been jointly optimized for the solar-powered UAV acting as an ambient powered 3D wireless base station.

Acknowledgement

The content of this chapter has been based on the research publication:

(i) N. Varshney and S. De, "Design optimization for UAV aided sustainable 3D wireless communication at mmWaves," *IEEE Trans. Veh. Technol.*, vol. 72, no. 3, pp. 3274-3287, March 2023.

Chapter 6

Reduced Complexity Beamforming for RIS-assisted Indoor mmWave Communications

6.1 Introduction

mmWave signals are easily obstructed by objects such as buildings, walls, metals, and so on. In an outdoor environment, a UAV can be used as an airborne base station to offer service to obstructed UEs, as discussed in the preceding chapter. However, a UAV cannot be operated indoors. In this chapter, we look at mmWave communication in an obstructed indoor environment. Indoor wireless communication is also expected to benefit from mmWave technology. However, a large number of access points (APs) must be deployed to provide complete coverage in indoor mmWave communications. Since, the cost of deploying a dense network at mmWave is quite large thus, increasing the number of APs beyond a certain limit is not feasible. To this end, several studies have investigated the use of low cost passive RISs to improve indoor coverage and proposed various joint transmitter and RIS beamforming designs to maximize spectral and energy efficiency of the system [117, 118].

Another contemporary technology is backscatter communication that will play a crucial role in the development of smart indoor environments in near future by connecting low-power wireless devices. By leveraging the existing backscatter infrastructure, the performance of an indoor mmWave communication system can be improved without incurring any extra capital cost. The tags, when in idle mode, can be used to create a

additional LoS link at mmWave range between the AP and the legacy UE. The investigation in [35] of employing backscatter devices with MIMO systems to create an artificial rich scattering was performed at sub-6 GHz with single antenna tags, and transmitters and receivers employed digital beamforming with an equivalent number of RF chains as the number of antenna elements.

Therefore, towards achieving a low cost and low power adaptive backscatter environment for high data rate indoor communication at mmWaves, we consider the AP as well as the UE are equipped with a single RF chain connected with the respective antenna array. All devices at mmWave range, including AP, UE, and tags, have several antenna elements to combat high attenuation. Consequently, in this chapter, the multi-antenna tags-assisted mmWave communication system is analogous to distributed RIS-assisted mmWave communication system, in which the multi-antenna backscatter devices are essentially the same as small sized RISs distributed over an area.

Furthermore, similar to RIS, the reflection coefficient vector of multi-antenna tags can be optimized using CSI or angular information estimated during beam training [36]. However, it is computationally difficult to estimate the exact CSI of the cascaded channel between the AP, tag and UE. Therefore, we use the angular information to optimize the weights at the tags. For this, we need to estimate angle ϕ between a tag and the UE and the angle ϕ' between the AP and a tag. The traditional sub-spaced based algorithms, such as MUSIC and estimation of signal parameters via rotational invariance (ESPRIT), and others are incapable of estimating the angle with a single RF chain [119]. This is because these algorithms require the same number of RF chains as the number of antenna elements to determine spatial correlation. The works in [120] and [121] used the retro-reflective property for localization and beamforming in backscatter communication at mmWave range. When an antenna array is configured in retro-reflective mode it reflects the signal back in the same direction. Therefore, ϕ and ϕ' can be estimated independently at UE and AP end, respectively, without depending on the cascaded channel information. And this information can be exchanged with tags over sub-6 GHz for optimizing the tags' coefficients. Moreover, the size of the antenna array connected to a single RF chain at the AP or/and UE affects the performance of backscatter assisted communications. This is so because with increasing array size, the error in angle estimation decreases while the number of effective tags falling within a beam reduces. Therefore, it is interesting to investigate system performance at mmWaves in relation to antenna array size.

6.1.1 Contributions

The key contributions of this chapter are as follows.

- A novel backscatter-assisted indoor mmWave communication system is proposed and investigated, in which AP and UE are each equipped with a single RF chain connected to an antenna array, and each passive tag has multiple reflecting elements.
- For UE with unknown coordinates, a ML based AoA estimator is proposed to estimate the direction of arriving signals from all the tags that are configured in retro-reflective antenna mode. The initial AoA estimate is obtained using orthogonal matching pursuit (OMP) algorithm. Thereafter, the tags' reflection coefficients are optimized based on the estimated angles. Furthermore, the CRLB of the estimator is also derived.
- Different methods for determining optimal beam steering direction at the UE are also investigated. Additionally, the performance of backscatter-assisted indoor mmWave communication system is compared to that of a single RIS-assisted indoor mmWave communication system for different antenna array sizes at the UE.

6.1.2 Chapter Organization

The chapter organization is as follows. The system model is presented in Section 6.2. Link establishment procedure is presented in Section 6.3 and the AoA estimation along with its CRLB are presented in Section 6.4. The steering vector of is optimized in Section 6.5. The simulation results are presented in Section 6.6, and the summary is presented in Section 6.7.

6.2 System Model

Consider a wideband system having an AP, a mobile UE, and T backscatter tags in a 2-D scenario, as shown in Fig. 6.1. The LoS path between the AP and the mobile UE is completely blocked by a wall. The AP and UE are equipped with a broadside ULA, having N_{AP} and N_U antenna, respectively, placed along the y-axis. Both AP and UE are equipped with a single RF chain. The tags are distributed homogeneously with density λ

tags/m^2. Also, as the tags are passive devices, each tag is assumed to have N_T reflecting elements placed along y-axis.

Let the wideband channel of bandwidth B be divided into N_c subcarriers. Let the AP transmits signal $x[n]$ of power P through its ULA steered at an angle Ω_{AP}, where $n = \{1, \ldots, N_c\}$. Then the signal received at the UE via ith tag over nth subcarrier is [36]

$$y_i[n] = \boldsymbol{b}^H(\Omega_U)\boldsymbol{H}_i[n]\boldsymbol{\Gamma}_i\boldsymbol{G}_i[n]\boldsymbol{b}(\Omega_{AP})[n]x[n] + z_i[n] \tag{6.1}$$

where $\boldsymbol{G}_i[n]$ is the downlink channel from AP to ith tag and $\boldsymbol{H}_i[n]$ is the downlink channel from ith tag to UE over nth subcarrier. $\boldsymbol{b}(\Omega_{AP})$ and $\boldsymbol{b}(\Omega_U)$ are analog steering vector of AP steered at an angle Ω_{AP} and analog combiner of UE steered at an angle Ω_U, respectively. $z_i[n]$ is noise variable with distribution $\mathcal{N}(0, \sigma^2)$. $\boldsymbol{\Gamma}_i \in \mathbb{C}^{N_T \times N_T}$ denotes the reflection coefficient matrix of ith tag which is of the form

$$\boldsymbol{\Gamma_i} = \text{diag}\{\zeta e^{j\nu_{i,1}}, \ldots, \zeta e^{j\nu_{i,N_T}}\}. \tag{6.2}$$

In (6.2), ζ represents the amplitude attenuation and $\nu_{i,m}$ represents the phase shift of the mth reflecting element of ith tag. The array steering vector of a ULA having N antennas at the angle Ω is given as

$$\mathbf{b}(\Omega) = \frac{1}{\sqrt{N}}\left[1, e^{-j\frac{2\pi d'}{\lambda_c}\sin\Omega} \ldots, e^{-j\frac{2\pi d'}{\lambda_c}(N-1)\sin\Omega}\right]^T \in \mathbb{C}^{N\times 1} \tag{6.3}$$

where λ_c is the carrier wavelength and $d' = \lambda_c/2$ is the inter element spacing. Considering only LoS path, the mmWave channel over a subcarrier between AP and ith tag, and

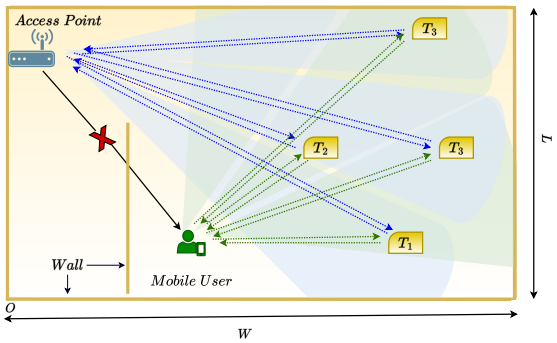

Figure 6.1: Illustration of backscatter-assisted mmWave communications system model with tags configured in retro-reflective mode.

between ith tag and UE, respectively, are

$$\begin{aligned}\boldsymbol{G}_i[n] &= \sqrt{N_T N_{AP}} g_i q(n,\tau_g) \mathbf{a}_{\mathrm{R}}(\phi_{i,g}) \mathbf{a}_{\mathrm{T}}^H(\theta_{i,g}) \in \mathbb{C}^{N_T \times N_{AP}} \\ \boldsymbol{H}_i[n] &= \sqrt{N_T N_U} h_i q(n,\tau_h) \mathbf{a}_{\mathrm{R}}(\phi_{i,h}) \mathbf{a}_{\mathrm{T}}^H(\theta_{i,h}) \in \mathbb{C}^{N_U \times N_T}\end{aligned} \tag{6.4}$$

where g_i and h_i are distance dependent Ricean faded channel gain of AP-ith tag channel and ith tag-UE channel, respectively. $q(n,\tau) = e^{-j2\pi(n-1)\Delta f \tau}$ is phase shift at nth subcarrier with delay τ. τ_g and τ_h are path delay of AP-ith tag channel and ith tag-UE channel, respectively. Δf is the subcarrier bandwidth, $\phi_{i,g}$ is AoA at ith tag from AP, $\theta_{i,g}$ is angle-of-departure (AoD) of AP to ith tag, $\phi_{i,h}$ is the AoA at UE from ith tag, and $\theta_{i,h}$ is AoD of ith tag. Here, $\mathbf{a}_{\mathrm{T}}(\cdot)$ and $\mathbf{a}_{\mathrm{R}}(\cdot)$ are respectively transmit and receive array manifold. The array manifold of a ULA having N antennas at an angle ω is as

$$\mathbf{a}(\omega) = \frac{1}{\sqrt{N}} \left[1, e^{-j\frac{2\pi d'}{\lambda_c}\sin(\omega)} \ldots, e^{-j\frac{2\pi d'}{\lambda_c}(N-1)\sin(\omega)}\right]^T \mathbb{C}^{N\times 1}. \tag{6.5}$$

Note, AoAs' and AoDs' are measured with respect to the broadside of an ULA. Assuming that the reflecting surface of all the tags face the UE and the plane of reflecting surface of tags lie in the plane of UE's ULA, we have $\phi_{i,h} = \theta_{i,h} = \phi_i$. Similarly, $\phi_{i,g} = \theta_{i,g} = \phi'_i$. Therefore, the signal received at UE from T tags over a subcarrier n is

$$\begin{aligned} y[n] =& \boldsymbol{b}^H(\Omega_U) \sum_{i=1}^{T} \boldsymbol{H}_i[n] \boldsymbol{\Gamma_i} \boldsymbol{G}_i[n] \boldsymbol{b}(\Omega_{AP}) x[n] + z[n] \\ =& N_T \sqrt{N_{AP} N_U} \boldsymbol{b}^H(\Omega_U) \left(\sum_{i=1}^{T} h_i g_i q(n,\tau_h) q(n,\tau_g) \right. \\ & \left. \mathbf{a}_{\mathrm{R}}(\phi_i) \mathbf{a}_{\mathrm{T}}^H(\phi_i) \boldsymbol{\Gamma_i} \mathbf{a}_{\mathrm{R}}(\phi'_i) \mathbf{a}_{\mathrm{T}}^H(\phi'_i) \boldsymbol{b}(\Omega_{AP}) x[n] \right) + z[n] \end{aligned} \tag{6.6}$$

Since the beams of the tags do not point to each other so the signal bouncing from tag to another can be considered to be very weak and is thus ignored. Therefore, the achievable downlink rate over N_c subcarriers is

$$R = \sum_{n=1}^{N_c} \frac{B}{N_c} \log_2 \left(1 + \frac{y[n] y^H[n]}{\sigma^2}\right). \tag{6.7}$$

In this paper, we assume that the UE is mobile. Hence, its relative location from the tags is unknown. Therefore, to establish a link between the AP and the UE we need to optimize $\{\boldsymbol{\Gamma}_i\}_{\forall i}$, Ω_{AP} and Ω_U. In a given indoor communication scenario, the location of AP and tags are fixed. Since the AP has high processing capabilities therefore, for

analysis simplicity we assume that the channel $\mathbf{G}_i$ is known a prior. Thus, $\{\phi'_i\}_{\forall i}$ for all $i = \{1, \ldots, T\}$ and Ω_{AP}, are known perfectly at the AP and tags. Hence, in this paper we only estimate $\{\phi_i\}_{\forall i}$ and based on that optimize Ω_U and $\{\boldsymbol{\Gamma}_i\}_{\forall i}$.

6.3 Link Establishment Procedure

The complete link establishment process is divided into three phases as shown in Fig. 6.2. In first phase, denoted by angle estimation phase, all the tags are configured in retro reflective mode. Therefore, an incident signal get reflected in the same direction. Further, a UE equipped with a ULA having N_U antenna elements generates a narrow directional beam. Subsequently, the 2π angular area around the UE is divided in S identical sectors of angular width equal to the HPBW of the beam which is $2/N_U$ radians. In each sector, UE transmit pilot symbols that are reflected by T_s tags falling within the sector. The UE employs maximum likelihood estimator to estimate the ϕ_i of the reflected signals from T_s tags.

In the second phase, denoted by feedback phase, using sub-6 GHz control plane the UE obtains unique identification number of each tag and then feedback the estimated angle $\hat{\phi}_i$ information to the respective tag. In the last phase, called optimization phase, each tag optimizes its $\boldsymbol{\Gamma}_i$ corresponding to the estimated $\hat{\phi}_i$ and ϕ'_i to direct the incident signal from AP to the UE. Moreover, using information of estimated direction between UE and tags, the UE optimizes its beam steering direction to achieve maximum rate support. Thereafter, the data transmission phase begins.

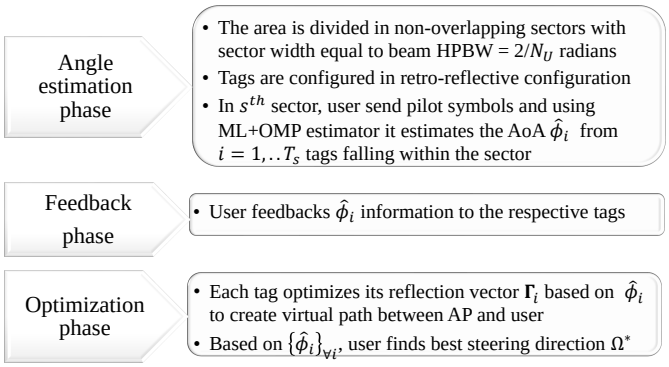

Figure 6.2: Flowchart for link complete virtual link establishment between AP and UE.

6.4 AoA Estimation

This section deals with estimation of AoA of the reflected signals from all the tags at the UE. It is not possible to use a sub-spaced based algorithm since a ULA coupled to an RF unit only provides one measurement. Therefore, we propose employing an ML estimator to estimate $\{\phi_i\}_{\forall i}$ at the UE equipped with a single RF chain.

We use ULA based geometry to design the tag reflection coefficient matrix $\boldsymbol{\Gamma}$ based only on angular information. Then, to reflect an incoming signal having incident angle ω_i to a direction an angle ω_r, the phase shift of the mth reflecting element in $\boldsymbol{\Gamma}_i$ for ith tag given as [120, 121]

$$\nu_{i,m} = (2\pi d'/\lambda_c)(m-1)(\sin\omega_i - \sin\omega_r). \tag{6.8}$$

During AoA estimation phase, all tags are assumed to be in a retro-reflective configuration, meaning that the angle of reflection at each tag is equal to the angle of incidence, i.e., $\omega_r = \omega_i$. As a result, the a signal transmitted by a UE at an angle ϕ towards a tag is received back from the same direction, providing spatial filtering and thus, $\boldsymbol{\Gamma}_i = \zeta \mathbf{I}_{N_T}$. The UE estimates the AoA from T tags by sequentially estimating AoA from T_s at a time that falls within a sector s, where $s = \{1, \ldots, S\}$. To estimate T_s AoAs in a sector s, the UE sweeps each sector in L' directions by varying its steering angle Ω in steps of Δ with the sector s, i.e.,

$$\Omega \in \left\{ \frac{2(s-1)}{N_U} + \Delta, \ldots, \frac{2(s-1)}{N_U} + L'\Delta \right\} \equiv \boldsymbol{\Omega} \tag{6.9}$$

where $\Delta = 2\pi/2^b$. Here, b represents the number of quantization bits.

Let the UE transmit same pilot signal x of power P over all N_c subcarriers through its beam steered at an angle $\Omega_l \in \boldsymbol{\Omega}$. Then the RF signal received at the antenna array of ith tag is

$$\mathbf{y}_l[n] = \boldsymbol{H}_i[n]\boldsymbol{b}(\Omega_l)x. \tag{6.10}$$

Owing to channel reciprocity, the uplink channel between UE and ith tag is

$$\boldsymbol{H}'_i[n] = \sqrt{N_T N_U} h_i q(n, \tau_h) \mathbf{a}_{\mathrm{R}}(\phi_i) \mathbf{a}_{\mathrm{T}}^H(\phi_i) \in \mathbb{C}^{N_T \times N_U}. \tag{6.11}$$

Reflected signal from all tags are received by the UE using the same beam steered at

Ω_l. Therefore, assuming perfect self interference cancellation, the received signal is

$$\begin{aligned} y_l[n] =& \boldsymbol{b}^H(\Omega_l) \sum_{i=1}^{T_s} \boldsymbol{H}_i'[n] \boldsymbol{\Gamma}_i \boldsymbol{H}_i[n] \boldsymbol{b}(\Omega_l) x + z_l[n] \\ =& N_T N_U \boldsymbol{b}^H(\Omega_l) \left(\sum_{i=1}^{T_s} (h_i q(n, \tau_h))^2 \mathbf{a}_{\mathrm{R}}(\phi_i) \mathbf{a}_{\mathrm{T}}^H(\phi_i) \boldsymbol{\Gamma}_i \, \mathbf{a}_{\mathrm{T}}(\phi_i) \mathbf{a}_{\mathrm{R}}^H(\phi_i) \boldsymbol{b}(\Omega_l) x \right) + z_l[n] \end{aligned} \tag{6.12}$$

where $z_l[n] \sim \mathcal{N}(0, \sigma^2)$. Since $\boldsymbol{\Gamma}_i = \zeta \mathbf{I}_{N_T}$, (6.12) reduces to

$$y_l[n] = N_T N_U \boldsymbol{b}^H(\Omega_l) \sum_{i=1}^{T_s} (h_i q(n, \tau_h))^2 \mathbf{a}_{\mathrm{R}}(\phi_i) \mathbf{a}_{\mathrm{R}}^H(\phi_i) \boldsymbol{b}(\Omega_l) x + z_l[n]. \tag{6.13}$$

It is notable that in (6.13) $\mathbf{a}_{\mathrm{R}}(\phi_i) = \mathbf{a}(\phi_i)_{N=N_U}$. Further, let $\beta_i[n] = N_T N_U (h_i q(n, \tau_h))^2$ and $\boldsymbol{\beta}[n] = [\beta_1[n], \dots \beta_{T_s}[n]]^T$. Then

$$\begin{aligned} y_l[n] &= \sum_{i=1}^{T_s} \boldsymbol{b}^H(\Omega_l) \mathbf{a}(\phi_i) \mathbf{a}^H(\phi_i) \boldsymbol{b}(\Omega_l) \beta_i[n] x + z_l[n] \\ &= (\boldsymbol{b}^H(\Omega_l) \mathbf{A} \odot (\mathbf{A}^H \boldsymbol{b}(\Omega_l)^T) \boldsymbol{\beta}[n] x + z_l[n]. \end{aligned} \tag{6.14}$$

Here $\mathbf{A} = [\mathbf{a}(\phi_1), \dots \mathbf{a}(\phi_{T_s})] \in \mathbb{C}^{N_U \times T_s}$ and $\odot$ denotes element wise product. Let $\bar{\boldsymbol{\beta}} = \{\boldsymbol{\beta}[1], \dots, \boldsymbol{\beta}[N_c]\} \in \mathbb{C}^{T_s \times N_c}$. Then the received signal vector over all subcarriers is

$$\mathbf{y}_l = (\boldsymbol{b}^H(\Omega_l) \mathbf{A} \odot (\mathbf{A}^H \boldsymbol{b}(\Omega_l))^T) \bar{\boldsymbol{\beta}} x + \mathbf{z}_l \in \mathbb{C}^{1 \times N_c}. \tag{6.15}$$

Over all L' steering directions in a sector sweep, the received signal is

$$\mathbf{Y} = (\boldsymbol{B}^H \mathbf{A} \odot (\mathbf{A}^H \boldsymbol{B})^T) \bar{\boldsymbol{\beta}} x + \mathbf{Z} \in \mathbb{C}^{L' \times N_c} \equiv \bar{\mathbf{D}} \bar{\boldsymbol{\beta}} + \mathbf{Z} \tag{6.16}$$

where $\boldsymbol{B} = [\mathbf{b}(\Omega_1), \dots \mathbf{b}(\Omega_L)] \in \mathbb{C}^{N_U \times L'}$ and $\mathbf{Z} \in \mathbb{C}^{L' \times N_c}$ is the noise matrix. (6.16) is the sum of reflected signals coming from only a small number of directions. Hence, the solution to AoA estimation at the UE is sparse. Therefore, in each sector s, we employ ML estimator to recover T_s directions of arrival $\{\phi_i\}$. Let $\boldsymbol{\phi} = \{\phi_1, \dots, \phi_{T_s}\}$, then the ML estimator for sector s is represented as

$$\begin{aligned} (\mathcal{P}1) : & \underset{\boldsymbol{\phi}}{\operatorname{argmin}} \, \|\mathbf{Y} - \mathbf{D}\mathbf{D}^{\dagger}\mathbf{Y}\|^2 \\ & \text{s.t. } 2(s-1)/N_U \leq \phi_i \leq 2s/N_U \; \forall i = \{1, \dots, T_s\}. \end{aligned} \tag{6.17}$$

Here, $\mathbf{D}^{\dagger}$ represents Moore–Penrose inverse of a matrix $\mathbf{D}$. Each column of dictionary matrix $\mathbf{D} \in \mathbb{C}^{L' \times T_s}$ is given as

$$\mathbf{d}(\phi) = \boldsymbol{B}^H \mathbf{a}(\phi) \odot (\mathbf{a}^H(\phi) \boldsymbol{B})^T. \tag{6.18}$$

Algorithm 6.1 OMP

Input: $i = 0$, $\mathbf{r}_i = \mathbf{Y}$, $\mathbf{d}(\phi)$, $\delta = 0.001$
Output: $\{\phi_1, \dots \phi_{T_s}\}$
Initialize
do
    $\phi^* = \underset{\phi \in \Phi}{\text{argmax}} \|\mathbf{d}(\phi)^H \mathbf{r}_i\|$
    Update $\phi_e = \phi_e \cup \phi^*$
    Increment i
    $\mathbf{Q} = \mathbf{d}(\phi_e)\mathbf{d}(\phi_e)^H \mathbf{d}(\phi_e))^{-1} \mathbf{d}(\phi_e)^H$
    $\mathbf{r}_i = (\mathbf{I} - \mathbf{Q})\mathbf{Y}$
while $i \leq T_s$ and $\mathbf{r}_i \geq \epsilon$

Problem $(\mathcal{P}1)$ is non-convex. Therefore, we find local minima around an initial estimate. We procure the initial estimate of AoAs using OMP estimator [122]. For analytically simplicity, we assume that the number of tags falling within the beam's coverage area T_s is known a priori. The steps of the OMP estimator are given in Algorithm 6.1.

Therefore, from (6.8), the mth optimal reflecting coefficient of ith tag is given as

$$\nu^*_{i,m} = (2\pi d'/\lambda_c)(m-1)(\sin\phi'_i - \sin\hat{\phi}_i) \tag{6.19}$$

where $\hat{\phi}_i$ is the estimated AoA at UE from ith tag.

6.4.1 CRLB Analysis

Next, we derive the lower bound on the AoA estimation using CRLB. From (6.14), the received signal over L' snapshots on nth subcarrier within a sector s is

$$\boldsymbol{y}[n] = \boldsymbol{\mu}[n] + \boldsymbol{z}[n] \tag{6.20}$$

where $\boldsymbol{\mu}[n]$ denotes the noiseless part of received signal. Let the vector of unknown parameters in (6.20) over a subcarrier n is given by $\boldsymbol{\eta} = [\boldsymbol{\phi}, Re\{\boldsymbol{\beta}\}, Im\{\boldsymbol{\beta}\}] \in \mathbb{C}^{3T_s \times 1}$.

Subsequently, for I snapshots, the FIM $\boldsymbol{J}(\boldsymbol{\eta}) \in \mathbb{R}^{3T_s \times 3T_s}$ for sth sector is defined as [72]

$$\boldsymbol{J}(\boldsymbol{\eta}) = \frac{2}{\sigma^2} \sum_{i=1}^{I} \sum_{n=1}^{N_c} Re\left\{ \frac{\partial[\boldsymbol{\mu}[n]]_i}{\partial \boldsymbol{\eta}} \left(\frac{\partial[\boldsymbol{\mu}[n]]_i}{\partial \boldsymbol{\eta}} \right)^H \right\} \tag{6.21}$$

where

$$\begin{aligned}
\frac{\partial[\mu_l[n]]_i}{\partial\phi_k} &= -j\frac{2\pi d'}{\lambda_c}\frac{\beta_k[n]\cos\phi_k}{N_U N_U}\sum_{n=1}^{N_u}\sum_{m=1}^{N_u}(m-n)e^{-\frac{j2\pi d'}{\lambda_c}(m-n)(\sin\phi_i-\sin\Omega_l)}x \\
\frac{\partial[\boldsymbol{\mu}[n]]_i}{\partial Re(\beta_k[n])} &= (\boldsymbol{B}^H\mathbf{a}(\phi)\odot\boldsymbol{B}^H\mathbf{a}(\phi))x \\
\frac{\partial[\boldsymbol{\mu}[n]]_i}{\partial Im(\beta_k[n])} &= j(\boldsymbol{B}^H\mathbf{a}(\phi)\odot\boldsymbol{B}^H\mathbf{a}(\phi))x.
\end{aligned} \tag{6.22}$$

Using (6.21), the Angle Error Bound (AEB) of ϕ_k is

$$\text{AEB} = \sqrt{\text{diag}[\mathbf{J}^{-1}(\boldsymbol{\eta})]_{k,k}}. \tag{6.23}$$

Thus, AEB is the lower bound on ϕ_k estimate.

6.5 Steering Vector Optimization

Following AoA estimation at the UE and optimization of tag reflection coefficients, as discussed in the previous section, in this section we optimize the analog combiner at the UE. Since a UE only has one RF unit connected to a ULA, optimizing the analog combiner is equivalent to determining the best steering direction. Below we describe the various schemes for optimizing UE steering direction.

- Sectoring scheme: As discussed in Section 6.4, area around the UE is divided into S sectors. So, a codebook is made up of fixed steering vectors corresponding to steering angles in $\boldsymbol{\Omega}_S = \{(2s-1)/N_U | s = \{1,\ldots,S\}\}$ radian. Then, the optimal UE steering angle is $\Omega^* = \underset{\Omega\in\boldsymbol{\Omega}_S}{\text{argmax}}\, R(\Omega)$, where $R(\Omega)$ denotes the rate achieved by UE when its beam is steered at direction Ω.

- Grouping scheme: The tags are grouped using k-means clustering. Given N_U, the number of clusters is equal to the number of sectors with at least one tag i.e, $k = \sum_{s=1}^{|\Omega_S|}\pi_s$ where $\pi_s = 1$ if $T_s \geq 1$; 0 otherwise. Further, the steering angle Ω_g of the gth cluster is equal to the median of all the AoAs in group g. Therefore, the set of steering angles is $\boldsymbol{\Omega}_G = \{\Omega_g | g = \{1,\ldots,k\}\}$. Consequently, optimal UE steering direction is $\Omega^* = \underset{\Omega\in\boldsymbol{\Omega}_G}{\text{argmax}}\, R(\Omega)$.

- Exhaustive scheme: This scheme is similar to sectoring except that there are E scanning directions separated by $\delta\phi = 2\pi/E$ radian intervals regardless of beamwidth.

Therefore, the set of all steering directions in the codebook is $\boldsymbol{\Omega}_E = \{0, \delta\phi, \ldots, (E-1)\delta\phi\}$. The optimal beam direction at UE is the found as $\Omega^* = \underset{\Omega \in \boldsymbol{\Omega}_E}{\text{argmax}}\, R(\Omega)$.

A comparative analysis of all the above discussed schemes is presented in the following section.

6.6 Results and Discussions

In this section, we present the numerical results obtained from MATLAB Monte Carlo simulations. Table 6.1 lists the values of various simulation parameters used. In addition, we use the thinning method to simulate the non-homogeneous tag distribution, with thinning intensity equal to 3 [124].

Fig. 6.3 shows the root mean squared error (RMSE) of the proposed AoA estimator and compares it to the AEB for various N_U values. Notably, a higher value of N_U results in a narrower beam, reducing the effective number of tags and hence total number of reflecting elements $\bar{N}_T$ that contribute to virtual paths between the AP and the UE, as shown in Fig. 6.4. As illustrated in Fig. 6.3(a), with $N_U = 16$ and $\lambda = 1$ tags/m^2, only one tag falls within a sector on average, and the RMSE reaches the AEB at high SNR values. The average number of tags per sector increases to two and three when

Table 6.1: Simulation parameters

Parameter	**Variable**	**Value**
Length of room	L	5m
Width of room	W	10 m
Carrier frequency	f_c	28 GHz
Number of subcarriers	N_c	30
Bandwidth	B	100 MHz
Bits	b	10
Rician fading parameter	κ	18 dB
Noise power spectral density	N_0	-174 dbm/Hz/s
Reflection amplitude attenuation	ζ	0.5
Number of reflecting elements at tag	N_T	8
Number of antenna elements at AP	N_{AP}	4
Wall tip 2D coordinates	$[x_W, y_W]$	$[1.44, L/2]$ m
AP 2D coordinates	$[x_{AP}, y_{AP}]$	$[0, L]$ m
RIS 2D coordinates	$[x_R, y_R]$	$[W/2, L/2]$ m
AP transmit power	P	33 dBm [123]

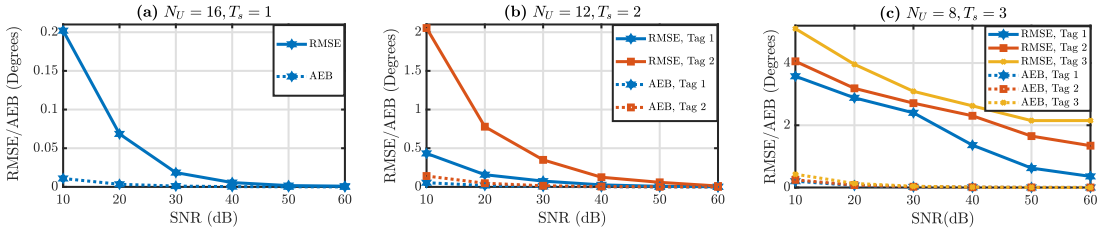

Figure 6.3: RMSE and AEB of proposed AoA estimator.

$N_U = 12$ and $N_U = 8$, respectively. Subsequently, the RMSE also increases, as shown in Fig. 6.3(b) and Fig. 6.3(c). There are two reasons for the increase in RMSE. First, the correlation in the OMP algorithm decreases as the number of closely located tags T_s increases. Furthermore, OMP is a residue-based algorithm. Therefore, the error in initial AoA estimate of first tag propagates into the initial AoA estimate of second tag, and so on. Moreover, because the ML estimator is non-convex, we can only find local minimums near the initial points. As a result, the output of ML estimator is affected by the initial AoA estimates obtained from OMP algorithm. Fig. 6.5 illustrates the reduction in rate at the UE when using erroneous estimated AoAs to design tags' reflection coefficients and combiner at UE as compared to using exact AoAs.

Following that, we compare the data rate obtained with tags for three different UE beam steering strategies discussed in Section 6.5. We also compare the results to those obtained when a fixed linear RIS is used to assist the communication between the AP and blocked UE. Since the location of UE is unknown hence, in simulation we consider RIS coordinates as $[W/2, L/2]$ to provide coverage at all points behind the wall. For a fair comparison, we take the number of reflecting elements at RIS to be equal to $\bar{N}_T$. Additionally, we compare the results with another scheme in which the tags have random $\boldsymbol{\Gamma}_i$ and UE beam sweeps the area in a round-robin fashion. As a result, no initial angle estimation, feedback, or reflection coefficient optimization are required.

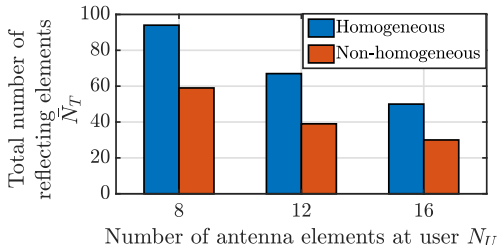

Figure 6.4: Average number of reflecting elements $\bar{N}_T$ aiding AP to UE communication when tags are distributed homogeneously and non-homogeneously with $\lambda = 2$ and $N_T = 8$.

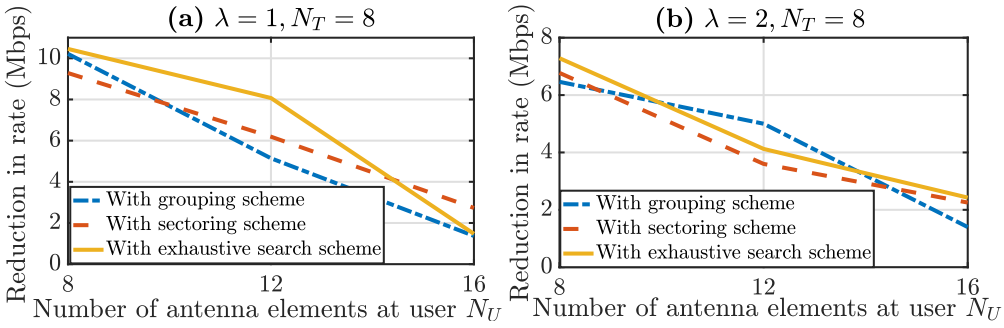

Figure 6.5: Reduction in rate when using estimated AoAs as compared to using true AoAs to design tags' reflection coefficients and UE steering direction in case of homogeneously distributed tags.

Fig. 6.6 depicts the rate achieved with different schemes for different simulation scenarios. As illustrated, the achievable rate with sectoring, grouping and exhaustive search schemes improves with N_U despite the fact that average number of reflecting elements $\bar{N}_T$ decreases as N_U increases. This is because of higher array gain at UE and lower RMSE of the AoA estimator at higher value of N_U. Moreover, Fig. 6.6, shows that using tags distributed over an area gives better rate support than using a single RIS with having $\bar{N}_T$ number of reflecting elements. Further, at high value of N_U and small value of $\bar{N}_T$, rate achieved by using random weights at tags approaches the rate achieved using RIS, as shown in Fig. 6.6(a) and Fig. 6.6(d).

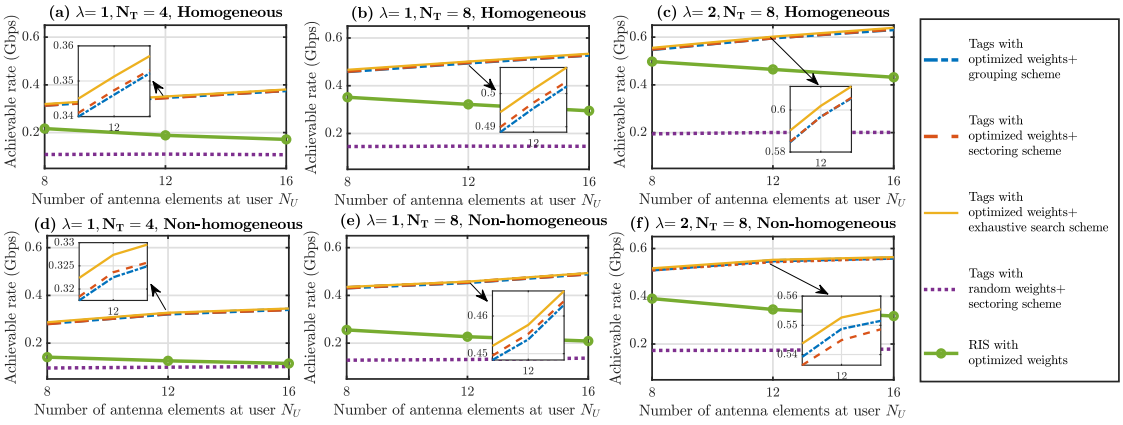

Figure 6.6: Comparison of achievable rate with different schemes for homogeneously distributed and non-homogeneously distributed tags.

6.7 Summary

In this chapter, a strategy has been proposed to utilize the existing backscatter infrastructure to provide connectivity to a blocked UE with unknown coordinates in an indoor mmWave communication system. First, by configuring the tags in retro-reflective mode, a novel method has been proposed for estimating the AoA from tags to the UE. Following that, a joint OMP and ML estimator has been proposed to estimate the AoAs at the UE equipped with a single RF chain. It has been observed that at a sufficiently high SNR and a large number of antenna elements at the UE, the estimator's RMSE reaches AEB. This condition deteriorates with decreasing ULA size of the UE. Furthermore, the UE steering direction and tag weights are optimized to maximize the UE's achievable rate. The findings has demonstrated that the existing backscatter infrastructure can support mmWave communications while providing improved gains over that achieved using a single RIS with an equivalent number of reflecting elements as at the tags. Although few tags contributes to the less number of paths between AP and UE, a narrow beam of high gain nevertheless achieves a higher gain in both homogeneous and non-homogeneous tag distribution cases.

The primary goal of this chapter has been to demonstrate the potential for using tags to enhance the performance of UEs. However, the AoA estimator utilized in this study was based on the assumption that the plane of the UE's ULA and the plane of the tags' reflecting elements were parallel to each other. This assumption may not always hold true in practical scenarios. Therefore, there is a need for a more general AoA estimator that can accurately detect the AoA of LoS links, regardless of the orientation of the ULA. Additionally, a protocol for exchanging control information regarding AoA between the tags and AP, as well as between the UE and the tags, over sub-6 GHz band, must be designed.

Acknowledgement

The content of this chapter has been based on the research publication:

(i) N. Varshney, R. Ghazalian, R. Jäntti, and S. De, "BackScatter-assisted Indoor mmWave Communications with Directional Beam at User," in *Proc. IEEE Int. Conf. Commun. (ICC)*, 2023. (Accepted Jan. 2023)

Chapter 7

Concluding Remarks and Future Works

7.1 Concluding Remarks

In this dissertation, several energy-efficient and spectrally-efficient reduced complexity frameworks with a constraint on the number of RF chains have been presented to serve users over wideband mmWave channel in different standalone mmWave communication systems. The frameworks have been investigated by studying the interplay of various factors for beamforming optimization at mmWave range.

First, a multi-user wideband mmWave terrestrial standalone communication system has been explored. In this context, a sectored-cell framework has been suggested to service a large UE population with a single RF chain generating a directional beam that serves the sectors in a round-robin method. For the proposed sectored-cell framework, the effect of UE localization error, UE population, and UE distribution on the selection of optimal beamwidth (equivalent optimal cell sectorization) for maximizing the UEs' QoS has been studied. The results reveal that, while narrow beams have a better spatial reuse factor and energy efficiency, they do not always attain the best average long-run UE rates in both homogeneous and non-homogeneous UE distribution scenarios. Furthermore, the localization error does not alter the beamwidth selection for the case of static UEs.

Further, the sectored-cell framework developed in Chapter 2 has been analyzed when multiple analog beams concurrently serve different sectors of a cell. While taking into account inter-beam sidelobes interference and beam squint, the optimal beamwidth and optimal number of RF chains has been estimated for different homogeneous UE population. For the case of non-homogeneous UE distribution, the sector sojourn time has been optimized with the granularity of 1 OFDM symbol to improve UE fairness and QoS.

Moreover, to optimally utilize the wide bandwidth and reduced latency in initial access, a modified initial access along with a variable time frame structure has been proposed for the sectored-cell framework with TTI as small as 1 OFDM symbol. For efficient bandwidth utilization the proposed variable time frame structure also allows for simultaneous transmission to connected UEs and initial access for new UEs trying to connect to the network. The sectored-cell framework in conjunction with variable time frame structure showed good performance gain in case of skewed UE distribution. With extensive simulation studies it has been shown that besides avoiding high signaling and computational complexity of beamforming of existing methods like SVD, OMP, and JSDM, among others, the sectored-cell framework offers improved QoS and UE fairness with reduced hardware complexities.

Thereafter, the beam squint effect at mmWaves has been addressed. Serving multiple UEs using OFDMA with hybrid precoder in wideband mmWave channel requires subcarrier allocation, RF precoder optimization, and baseband precoder optimization. By making use of the inherent beam squint effect at mmWaves, a RF-SC-BB strategy has been proposed to optimize the achievable rate. The RF-SC-BB strategy describes optimal order of optimization of the SC allocation and RF precoder, and then optimizes the baseband precoder for a sub-array based hybrid precoder using WMMSE. The effectiveness of the proposed method has been validated by simulation results.

Next, a low complex beamforming and UE grouping solutions has been presented in Chapter 5 for serving obstructed UEs by using a power-constrained solar-UAV as a fronthaul unit in a sustainable manner. It is also shown that grouping UEs using k-means clustering and adjusting beam coverage to target maximal radiation on the UEs is superior to sectorizing the area from both rate and energy efficiency perspective. It is also verified that with a given power budget, increasing the number of RF chains does not necessarily increase the system performance as the associated power waste in the RF circuitry increases. Thus, the number of beams should be optimized along with optimization of UAV battery capacity and solar panel for a sustainable operation for energy-constrained UAV-assisted communications at mmWaves.

Finally, the beamforming feasibility using the existing infrastructure of backscatter devices (acting as distributed RIS) has been analyzed to serve an obstructed UE in indoor mmWave communication system. The beamforming weights at the AP, UE and backscatter devices has been designed based solely on AoA information thereby bypassing the requirement of estimating cascaded channel CSI. Furthermore, an AoA estimator

has been proposed that requires single RF chain at the UE for estimating the angle.

The implementation of optimization-based approaches has been central to providing solutions to a variety of problems throughout this dissertation. Nonetheless, it is beneficial to consider the potential of machine learning-based approaches. For example, in Chapter 3, machine learning techniques could be utilized to determine the optimal sectorization scheme, the ideal number of RF chains, and the optimized sector sojourn time, based on UE distribution and population. Additionally, in Chapter 5, state-of-the-art supervised and unsupervised machine learning algorithms could be applied to optimize the number of beams to be activated at the UAV and the optimal user grouping, given a power budget. Furthermore, supervised machine learning could be employed to estimate the Angle of Arrival (AoA) at UEs in Chapter 6. However, it is important to note that as UE density/tag density and antenna array size increase, a larger training set would be required and the system training complexity would also increase in mobile mmWave environment.

In conclusion, it is anticipated that the beamforming designs and frameworks proposed in this dissertation using sub-array-type hybrid structures in various scenarios will aid in the design of low-cost and low-complexity energy-efficient architectures for standalone wideband mmWaves communication networks for 5G+ networks. These frameworks are generic and applicable in numerous ways. For example, the sectored-cell framework with optimized sector sojourn time can be used to service a large number of machines in a private enterprise, the variable time frame structure can be optimized to provide low latency services, and the proposed AoA estimator with a single RF chain offers a cost-effective solution for RIS-assisted communications.

7.2 Future Works

Below, we highlight some possible extensions of our works.

- Design variable time frame structure for sectored-cell framework applicable for combined enhanced Mobile Broadband (eMBB), massive Machine Type Communication, (mMTC) and Ultra Reliability and Low Latency Communication (URLLC) applications.

- Study the modifications required at UE equipment because of the variable time frame structure and the resulting implications on signaling overhead and power consumption.

- Investigate the effect of spatial and temporal correlation at mmWaves to propose reduced complexity and reduced training overhead beamforming designs in a multi-user aerial-RIS assisted mmWave communication system.

Bibliography

[1] I. S. 802.11ad 2012, *Part 11: Wireless LAN Medium Access Control (MAC) and Physical Layer (PHY) Specifications. Amendment 3: Enhancements for Very High Throughput in the 60 GHz Band*, 2012.

[2] S. Kutty and D. Sen, "Beamforming for millimeter wave communications: An inclusive survey," *IEEE Commun. Surveys Tuts.*, vol. 18, no. 2, pp. 949–973, 2015.

[3] L. Zhang, H. Zhao, S. Hou, Z. Zhao, H. Xu, X. Wu, Q. Wu, and R. Zhang, "A survey on 5G millimeter wave communications for UAV-assisted wireless networks," *IEEE Access*, vol. 7, pp. 117 460–117 504, 2019.

[4] Z. Xiao, L. Zhu, Y. Liu, P. Yi, R. Zhang, X.-G. Xia, and R. Schober, "A survey on millimeter-wave beamforming enabled UAV communications and networking," *IEEE Commun. Surveys Tuts.*, vol. 24, no. 1, pp. 557–610, 2021.

[5] W. Khawaja, I. Guvenc, D. W. Matolak, U.-C. Fiebig, and N. Schneckenburger, "A survey of air-to-ground propagation channel modeling for unmanned aerial vehicles," *IEEE Commun. Surveys Tuts.*, vol. 21, no. 3, pp. 2361–2391, 2019.

[6] S. Kang, M. Mezzavilla, A. Lozano, G. Geraci, W. Xia, S. Rangan, V. Semkin, and G. Loianno, "Millimeter-wave UAV coverage in urban environments," pp. 1–6, 2021.

[7] H. Lu, Y. Zeng, S. Jin, and R. Zhang, "Aerial intelligent reflecting surface: Joint placement and passive beamforming design with 3D beam flattening," *IEEE Trans. Wireless Commun.*, vol. 20, no. 7, pp. 4128–4143, 2021.

[8] A. Goldsmith, *Wireless Communications*. Cambridge university press, 2005.

[9] X. Wang, L. Kong, F. Kong, F. Qiu, M. Xia, S. Arnon, and G. Chen, "Millimeter wave communication: A comprehensive survey," *IEEE Commun. Surveys Tuts.*, vol. 20, no. 3, pp. 1616–1653, 2018.

[10] I. Ahmed, H. Khammari, A. Shahid, A. Musa, K. S. Kim, E. De Poorter, and I. Moerman, "A survey on hybrid beamforming techniques in 5G: Architecture and system model perspectives," *IEEE Commun. Surveys Tuts.*, vol. 20, no. 4, 2018.

[11] J. Lee, G.-T. Gil, and Y. H. Lee, "Channel estimation via orthogonal matching pursuit for hybrid MIMO systems in millimeter wave communications," *IEEE Trans. Commun.*, vol. 64, no. 6, pp. 2370–2386, 2016.

[12] J. Zhang, X. Yu, and K. B. Letaief, "Hybrid beamforming for 5G and beyond millimeter-wave systems: A holistic view," *IEEE Open J. Commun. Society*, vol. 1, pp. 77–91, 2019.

[13] Y. Liu, X. Liu, X. Mu, T. Hou, J. Xu, M. Di Renzo, and N. Al-Dhahir, "Reconfigurable intelligent surfaces: Principles and opportunities," *IEEE Commun. Surveys Tuts.*, vol. 23, no. 3, pp. 1546–1577, 2021.

[14] O. El Ayach, S. Rajagopal, S. Abu-Surra, Z. Pi, and R. W. Heath, "Spatially sparse precoding in millimeter wave MIMO systems," *IEEE Trans. Wireless Commun.*, vol. 13, no. 3, pp. 1499–1513, 2014.

[15] G. Kwon and H. Park, "Limited feedback hybrid beamforming for multi-mode transmission in wideband millimeter wave channel," *IEEE Trans. Wireless Commun.*, vol. 19, no. 6, pp. 4008–4022, 2020.

[16] V. N. Ha, D. H. Nguyen, and J.-F. Frigon, "Subchannel allocation and hybrid precoding in millimeter-wave OFDMA systems," *IEEE Trans. Wireless Communs.*, vol. 17, no. 9, pp. 5900–5914, 2018.

[17] Q. Xue, X. Fang, M. Xiao, and L. Yan, "Multiuser millimeter wave communications with nonorthogonal beams," *IEEE Trans. Veh. Technol.*, vol. 66, no. 7, pp. 5675–5688, 2016.

[18] H. Shokri-Ghadikolaei, C. Fischione, G. Fodor, P. Popovski, and M. Zorzi, "Millimeter wave cellular networks: A MAC layer perspective," *IEEE Trans. Commun.*, vol. 63, no. 10, pp. 3437–3458, 2015.

[19] A. Adhikary, E. Al Safadi, M. K. Samimi, R. Wang, G. Caire, T. S. Rappaport, and A. F. Molisch, "Joint spatial division and multiplexing for mm-wave channels," *IEEE J. Sel. Areas Commun.*, vol. 32, no. 6, pp. 1239–1255, 2014.

[20] M. Nair, Q. Z. Ahmed, J. Wang, and H. Zhu, "Low-complexity hybrid digital-to-analog beamforming for millimeter-wave systems with high user density," in *2017 IEEE 85th IEEE Veh. Technol. Conf. (VTC Spring)*, 2017, pp. 1–5.

[21] L. Qianrui, "Hybrid precoding for wideband multi-user MIMO millimeter wave system," in *Proc. IEEE Wireless Commun. Netw. Conf.*, 2019, pp. 1–6.

[22] V. N. Ha, D. H. Nguyen, and J.-F. Frigon, "Subchannel allocation and hybrid precoding in mmWave OFDMA systems," *IEEE Trans. Wireless Commun.*, vol. 17, no. 9, pp. 5900–5914, 2018.

[23] M. Mozaffari, W. Saad, M. Bennis, Y.-H. Nam, and M. Debbah, "A tutorial on UAVs for wireless networks: Applications, challenges, and open problems," *IEEE Commun. Surveys Tuts.*, vol. 21, no. 3, pp. 2334–2360, 2019.

[24] Y. Kawamoto, H. Nishiyama, N. Kato, F. Ono, and R. Miura, "Toward future unmanned aerial vehicle networks: Architecture, resource allocation and field experiments," *IEEE Wireless Commun.*, vol. 26, no. 1, pp. 94–99, 2019.

[25] C. Zhang, W. Zhang, W. Wang, L. Yang, and W. Zhang, "Research challenges and opportunities of UAV millimeter-wave communications," *IEEE Wireless Commun.*, vol. 26, no. 1, pp. 58–62, 2019.

[26] G. Fontanesi, A. Zhu, and H. Ahmadi, "Outage analysis for millimeter-wave fronthaul link of UAV-aided wireless networks," *IEEE Access*, vol. 8, pp. 111 693–111 706, 2020.

[27] M. Gapeyenko, V. Petrov, D. Moltchanov, S. Andreev, N. Himayat, and Y. Koucheryavy, "Flexible and reliable UAV-assisted backhaul operation in 5G mmWave cellular networks," *IEEE J. Sel. Areas Commun.*, vol. 36, no. 11, pp. 2486–2496, 2018.

[28] J. Sabzehali, V. K. Shah, H. S. Dhillon, and J. H. Reed, "3D placement and orientation of mmWave-based UAVs for guaranteed LoS coverage," *IEEE Wireless Commun. Lett.*, vol. 10, no. 8, pp. 1662–1666, 2021.

[29] G. Niu, Q. Cao, and M. Pun, "Block diagonal hybrid precoding and power allocation for QoS-aware BDMA downlink transmissions," *Sensors*, vol. 20, no. 16, p. 4497, 2020.

[30] Z. Xiao, H. Dong, L. Bai, D. O. Wu, and X.-G. Xia, "Unmanned aerial vehicle base station (UAV-BS) deployment with millimeter-wave beamforming," *IEEE Internet Things J.*, vol. 7, no. 2, pp. 1336–1349, 2019.

[31] S. Kumar, S. Suman, and S. De, "Dynamic resource allocation in UAV-enabled mmWave communication networks," *IEEE Internet Things J.*, vol. 8, no. 12, pp. 9920–9933, 2020.

[32] Z. Chen, N. Zhao, D. K. C. So, J. Tang, B. Tang, X. Zhang, and K. K. Wong, "Joint altitude and hybrid beamspace precoding optimization for UAV-enabled multiuser mmWave MIMO System," *IEEE Trans. Veh. Technol.*, pp. 1–1, 2021.

[33] Y. Liu, X. Liu, X. Mu, T. Hou, J. Xu, M. Di Renzo, and N. Al-Dhahir, "Reconfigurable intelligent surfaces: Principles and opportunities," *IEEE Commun. Surveys Tut.*, vol. 23, no. 3, pp. 1546–1577, 2021.

[34] J. Kimionis, A. Georgiadis, S. N. Daskalakis, and M. M. Tentzeris, "A printed millimetre-wave modulator and antenna array for backscatter communications at gigabit data rates," *Nature Electronics*, vol. 4, no. 6, pp. 439–446, 2021.

[35] A. Al-Nahari, R. Jantti, and M. U. Sheikh, "Artificial rich scattering-assisted mimo systems using passive backscatter devices," in *3rd Information Commun. Technol. Conf. (ICTC)*, 2022, pp. 19–24.

[36] B. Zheng, C. You, W. Mei, and R. Zhang, "A survey on channel estimation and practical passive beamforming design for intelligent reflecting surface aided wireless communications," *IEEE Commun. Surveys & Tut.*, vol. 24, no. 2, pp. 1035–1071, 2022.

[37] C. Singh, K. Singh, and K. Liu, "Fast beam training for RIS-assisted uplink communication," *arXiv preprint arXiv:2107.14138*, 2021.

[38] M. Dunna, C. Zhang, D. Sievenpiper, and D. Bharadia, "ScatterMIMO: Enabling virtual MIMO with smart surfaces," in *Proc. 26th Annual Int. Conf. Mobile Computing and Networking*, 2020, pp. 1–14.

[39] Z. Chen, P. Chen, Z. Guo, and X. Wang, "A RIS-based passive DOA estimation method for integrated sensing and communication system," *arXiv preprint arXiv:2204.11626*, 2022.

[40] Z. Ding, P. Fan, and H. V. Poor, "Random beamforming in millimeter-wave NOMA networks," *IEEE Access*, vol. 5, pp. 7667–7681, 2017.

[41] F. Sohrabi and W. Yu, "Hybrid analog and digital beamforming for mmWave OFDM large-scale antenna arrays," *IEEE J. Sel. Areas Commun.*, vol. 35, no. 7, pp. 1432–1443, 2017.

[42] B. Wang, M. Jian, F. Gao, G. Y. Li, and H. Lin, "Beam squint and channel estimation for wideband mmWave massive MIMO-OFDM systems," *IEEE Trans. Sig. Process.*, vol. 67, no. 23, pp. 5893–5908, 2019.

[43] G. Li, H. Zhao, and H. Hui, "Beam squint compensation for hybrid precoding in millimetre-wave communication systems," *Electronics Lett.*, vol. 54, no. 14, pp. 905–907, 2018.

[44] Y. Chen, D. Chen, T. Jiang, and L. Hanzo, "Channel-covariance and angle-of-departure aided hybrid precoding for wideband multiuser millimeter wave MIMO systems," *IEEE Trans. Commun.*, vol. 67, no. 12, pp. 8315–8328, 2019.

[45] Y. Chen, Y. Xiong, D. Chen, T. Jiang, S. X. Ng, and L. Hanzo, "Hybrid precoding for wideband millimeter wave MIMO systems in the face of beam squint," *IEEE Trans. Wireless Commun.*, vol. 20, no. 3, pp. 1847–1860, 2020.

[46] G. Femenias and F. Riera-Palou, "Wideband cell-free mmwave massive MIMO-OFDM: Beam squint-aware channel covariance-based hybrid beamforming," *IEEE Trans. Wireless Commun.*, vol. 21, no. 7, pp. 4695–4710, 2021.

[47] A. Alkhateeb, Y.-H. Nam, M. S. Rahman, J. Zhang, and R. W. Heath, "Initial beam association in millimeter wave cellular systems: Analysis and design insights," *IEEE Trans. Wireless Commun.*, vol. 16, no. 5, pp. 2807–2821, 2017.

[48] J. Zhang, Y. Huang, C. Zhang, S. He, M. Xiao, and L. Yang, "Cooperative multi-subarray beam training in millimeter wave communication systems," in *Proc. IEEE Global Commun. Conf.*, 2017, pp. 1–6.

[49] H. Soleimani, R. Parada, S. Tomasin, and M. Zorzi, "Fast initial access for mmWave 5G systems with hybrid beamforming using online statistics learning," *IEEE Commun. Mag.*, vol. 57, no. 9, pp. 132–137, 2019.

[50] Y. Li, J. G. Andrews, F. Baccelli, T. D. Novlan, and C. J. Zhang, "Design and analysis of initial access in millimeter wave cellular networks," *IEEE Trans. Wireless Commun.*, vol. 16, no. 10, pp. 6409–6425, 2017.

[51] Z. Xiao, P. Xia, and X.-G. Xia, "Codebook design for millimeter-wave channel estimation with hybrid precoding structure," *IEEE Trans. Wireless Commun.*, vol. 16, no. 1, pp. 141–153, 2016.

[52] M. Giordani, M. Polese, A. Roy, D. Castor, and M. Zorzi, "A tutorial on beam management for 3GPP NR at mmWave frequencies," *IEEE Commun. Surveys Tuts.*, vol. 21, no. 1, pp. 173–196, 2018.

[53] S. Dutta, M. Mezzavilla, R. Ford, M. Zhang, S. Rangan, and M. Zorzi, "Frame structure design and analysis for millimeter wave cellular systems," *IEEE Trans. Wireless Commun.*, vol. 16, no. 3, pp. 1508–1522, 2017.

[54] I. S. Association *et al.*, "Part 11: Wireless LAN medium access control (MAC) and physical layer (PHY) specifications," *IEEE Std.*, vol. 802, 2012.

[55] B. Schultz, "802.11 ad–WLAN at 60 GHz–A technology introduction," *Rohde & Schwarz*, 2013.

[56] 3GPP, "Physical layer procedures for data – Rel. 15," 2019, TS 38.214 V15.5.0.

[57] ——, "5G: NR Physical layer procedures for data–Rel. 15," 2018, TS 38.214 V15.3.0.

[58] N. Eshraghi, V. Shah-Mansouri, and B. Maham, "Fair beamwidth selection and resource allocation for indoor millimeter-wave networks," in *2017 IEEE Int. Conf. Commun. (ICC)*, 2017, pp. 1–6.

[59] S. Doğan, M. Karabacak, and H. Arslan, "Optimization of antenna beamwidth under blockage impact in millimeter-wave bands," in *IEEE 29th Int. Symp. Personal, Indoor and Mobile Radio Commun. (PIMRC)*, 2018, pp. 1–5.

[60] B. Thors, D. Colombi, Z. Ying, T. Bolin, and C. Törnevik, "Exposure to RF EMF from array antennas in 5G mobile communication equipment," *IEEE Access*, vol. 4, pp. 7469–7478, 2016.

[61] T. S. Rappaport, J. H. Reed, and B. D. Woerner, "Position location using wireless communications on highways of the future," *IEEE Commun. Mag.*, vol. 34, no. 10, pp. 33–41, 1996.

[62] A. Fascista, A. Coluccia, H. Wymeersch, and G. Seco-Granados, "Millimeter-wave downlink positioning with a single-antenna receiver," *IEEE Trans. Wireless Commun.*, vol. 18, no. 9, pp. 4479–4490, 2019.

[63] M. Koivisto, M. Costa, J. Werner, K. Heiska, J. Talvitie, K. Leppänen, V. Koivunen, and M. Valkama, "Joint device positioning and clock synchronization in 5g ultra-dense networks," *IEEE Trans. Wireless Commun.*, vol. 16, no. 5, pp. 2866–2881, 2017.

[64] D. J. Daley and D. Vere-Jones, *An introduction to the theory of point processes: volume II: General theory and structure*. Springer Science & Business Media, 2007.

[65] M. R. Akdeniz, Y. Liu, M. K. Samimi, S. Sun, S. Rangan, T. S. Rappaport, and E. Erkip, "Millimeter wave channel modeling and cellular capacity evaluation," *IEEE J. Sel. Areas Commun.*, vol. 32, no. 6, pp. 1164–1179, 2014.

[66] W. Yu and R. Lui, "Dual methods for nonconvex spectrum optimization of multi-carrier systems," *IEEE Trans. Commun.*, vol. 54, no. 7, pp. 1310–1322, 2006.

[67] S. Boyd, S. P. Boyd, and L. Vandenberghe, *Convex optimization*. Cambridge university press, 2004.

[68] Y. J. Zhang and K. B. Letaief, "Multiuser adaptive subcarrier-and-bit allocation with adaptive cell selection for OFDM systems," *IEEE Trans. Wireless Commun.*, vol. 3, no. 5, pp. 1566–1575, 2004.

[69] A. B. Sediq, R. H. Gohary, and H. Yanikomeroglu, "Optimal tradeoff between efficiency and Jain's fairness index in resource allocation," in *2012 IEEE 23rd Int. Symp. Personal, Indoor and Mobile Radio Commun. (PIMRC)*, 2012, pp. 577–583.

[70] C. Jiang, Y. Shi, Y. T. Hou, and S. Kompella, "On optimal throughput-energy curve for multi-hop wireless networks," in *2011 Proc. IEEE INFOCOM*, 2011, pp. 1341–1349.

[71] C. A. Balanis, *Antenna Theory: Analysis and Design*. John wiley & sons, 1997.

[72] S. M. Kay, *Fundamentals of statistical signal processing: Estimation theory*. Prentice-Hall, Inc., 1993.

[73] D. Dardari, E. Falletti, and M. Luise, *Satellite and terrestrial radio positioning techniques: A signal processing perspective*. Academic Press, 2012.

[74] T. Zhou, C. Tao, L. Liu, and Z. Tan, "Ricean K-factor measurements and analysis for wideband radio channels in high-speed railway U-shape cutting scenarios," in *IEEE Veh. Technol. Conf. (VTC Spring)*, May, 2014.

[75] T. S. Rappaport, S. Sun, R. Mayzus, H. Zhao, Y. Azar, K. Wang, G. N. Wong, J. K. Schulz, M. Samimi, and F. Gutierrez, "Millimeter wave mobile communications for 5G cellular: It will work!" *IEEE Access*, vol. 1, pp. 335–349, 2013.

[76] T. S. Rappaport, F. Gutierrez, E. Ben-Dor, J. N. Murdock, Y. Qiao, and J. I. Tamir, "Broadband millimeter-wave propagation measurements and models using adaptive-beam antennas for outdoor urban cellular communications," *IEEE Trans. Antennas and Propag.*, vol. 61, no. 4, pp. 1850–1859, 2012.

[77] H. Shokri-Ghadikolaei and C. Fischione, "The transitional behavior of interference in millimeter wave networks and its impact on medium access control," *IEEE Trans. Commun.*, vol. 64, no. 2, pp. 723–740, 2015.

[78] G. Sanfilippo, O. Galinina, S. Andreev, S. Pizzi, and G. Araniti, "A concise review of 5G new radio capabilities for directional access at mmWave frequencies," *Internet of Things, Smart Spaces, Next Generation Netw. Syst.*, pp. 340–354, 2018.

[79] 3GPP, "Study on channel model for frequency spectrum above 6 GHz–Rel. 14," 2017, TR 38.900 V14.2.0.

[80] L. N. Ribeiro, S. Schwarz, M. Rupp, and A. L. de Almeida, "Energy efficiency of mmWave massive MIMO precoding with low-resolution DACs," *IEEE J. Sel. Topics Sig. Process.*, vol. 12, no. 2, pp. 298–312, 2018.

[81] 3GPP, "Physical channels and modulation – Rel. 15," 2020, TR 38.211 V15.8.0.

[82] N. Atteya, S. maximov, and M. A. El-saidny, "A new era for enhanced mobile broadband (White paper)," Mediatek, 2018.

[83] L. Zhang, C. Jin, and W. Zhou, "Decomposition proportional fairness algorithm for multiuser OFDM systems," in *Proc. IEEE Int. Conf. Commun. Workshops*, 2008, pp. 21–25.

[84] A. Masmoudi and T. Le-Ngoc, "User grouping and hybrid RF/baseband precoding for multi-user massive MIMO systems," *IEEE Trans. Veh. Technol.*, vol. 69, no. 10, pp. 11 308–11 322, 2020.

[85] E. Kim, J. Kwak, and S. Chong, "Virtual beamforming and user scheduling for sub-array architecture in mmWave networks," *IEEE Commun. Lett.*, vol. 23, no. 1, pp. 168–171, 2018.

[86] H. Li, M. Li, Q. Liu, and A. L. Swindlehurst, "Dynamic hybrid beamforming with low-resolution pss for wideband mmWave MIMO-OFDM systems," *IEEE J. Sel. Areas Commun.*, vol. 38, no. 9, pp. 2168–2181, 2020.

[87] X. Sun and C. Qi, "Codeword selection and hybrid precoding for multiuser millimeter-wave massive MIMO systems," *IEEE Commun. Lett.*, vol. 23, no. 2, pp. 386–389, 2018.

[88] Y. Liu and J. Wang, "Low-complexity OFDM-based hybrid precoding for multiuser massive MIMO systems," *IEEE Wireless Commun. Lett.*, vol. 9, no. 3, pp. 263–266, 2020.

[89] L. Kong, S. Han, and C. Yang, "Hybrid precoding with rate and coverage constraints for wideband massive MIMO systems," *IEEE Trans. Wireless Commun.*, vol. 17, no. 7, pp. 4634–4647, 2018.

[90] M. Cai, K. Gao, D. Nie, B. Hochwald, J. N. Laneman, H. Huang, and K. Liu, "Effect of wideband beam squint on codebook design in phased-array wireless systems," in *Proc. IEEE GLOBECOM*, 2016, pp. 1–6.

[91] Q. Shi, M. Razaviyayn, Z.-Q. Luo, and C. He, "An iteratively weighted MMSE approach to distributed sum-utility maximization for a MIMO interfering broadcast channel," *IEEE Trans. Sig. Process.*, vol. 59, no. 9, 2011.

[92] D. J. Daley and D. Vere-Jones, *An introduction to the theory of point processes: volume I: Elementary theory and methods*. Springer, 2003.

[93] L. Wang, Y. L. Che, J. Long, L. Duan, and K. Wu, "Multiple access mmWave design for UAV-aided 5G communications," *IEEE Wireless Commun.*, vol. 26, no. 1, pp. 64–71, 2019.

[94] A. N. Uwaechia and N. M. Mahyuddin, "A comprehensive survey on millimeter wave communications for fifth-generation wireless networks: Feasibility and challenges," *IEEE Access*, vol. 8, pp. 62 367–62 414, 2020.

[95] C. Qiu, Z. Wei, Z. Feng, and P. Zhang, "Backhaul-aware trajectory optimization of fixed-wing UAV-mounted base station for continuous available wireless service," *IEEE Access*, vol. 8, pp. 60 940–60 950, 2020.

[96] D. Hong, S. Lee, Y. H. Cho, D. Baek, J. Kim, and N. Chang, "Least-energy path planning with building accurate power consumption model of rotary unmanned aerial vehicle," *IEEE Trans. Veh. Technol.*, vol. 69, no. 12, pp. 14 803–14 817, 2020.

[97] Y. Zeng, J. Xu, and R. Zhang, "Energy minimization for wireless communication with rotary-wing UAV," *IEEE Trans. Wireless Commun.*, vol. 18, no. 4, pp. 2329–2345, 2019.

[98] Y. Sun, D. Xu, D. W. K. Ng, L. Dai, and R. Schober, "Optimal 3D-trajectory design and resource allocation for solar-powered UAV communication systems," *IEEE Trans. Commun.*, vol. 67, no. 6, pp. 4281–4298, 2019.

[99] X. Song, Z. Chang, X. Guo, P. Wu, and T. Hämäläinen, "Energy efficient optimization for solar-powered UAV communications system," in *Proc. IEEE Int. Conf. Commun. Workshops (ICC Workshops)*, 2021, pp. 1–6.

[100] U. Demir, M. Ç. İpek, C. Toker, and Ö. Ekici, "Energy-efficient rotary-wing UAV deployment under flight dynamics and QoS constraints," in *Proc. IEEE Int. Black Sea Conf. Commun. Networking (BlackSeaCom)*, 2019, pp. 1–5.

[101] P. Susarla, Y. Deng, G. Destino, J. Saloranta, T. Mahmoodi, M. Juntti, and O. Sílven, "Learning-based trajectory optimization for 5G mmWave uplink UAVs," in *IEEE Int. Conf. Commun. Workshops (ICC Workshops)*, 2020, pp. 1–7.

[102] W. Feng, N. Zhao, S. Ao, J. Tang, X. Zhang, Y. Fu, D. K. C. So, and K.-K. Wong, "Joint 3D trajectory and power optimization for UAV-aided mmWave MIMO-NOMA networks," *IEEE Trans. Commun.*, vol. 69, no. 4, pp. 2346–2358, 2021.

[103] S. Naqvi, J. Chakareski, N. Mastronarde, J. Xu, F. Afghah, and A. Razi, "Energy efficiency analysis of UAV-assisted mmWave HetNets," in *IEEE Int. Conf. Commun (ICC)*, 2018, pp. 1–6.

[104] Z. Xiao, H. Dong, L. Bai, D. O. Wu, and X.-G. Xia, "Unmanned aerial vehicle base station (UAV-BS) deployment with millimeter-wave beamforming," *IEEE Internet Things J.*, vol. 7, no. 2, pp. 1336–1349, 2020.

[105] M. Gapeyenko, D. Moltchanov, S. Andreev, and R. W. Heath, "Line-of-sight probability for mmWave-based UAV communications in 3D urban grid deployments," *IEEE Trans. Wireless Commun.*, vol. 20, no. 10, pp. 6566–6579, 2021.

[106] A. Basaligheh, P. Saffari, S. Rasti Boroujeni, I. Filanovsky, and K. Moez, "A 28–30 GHz CMOS reflection-type phase shifter with full 360 phase shift range," *IEEE Trans. Circuits and Systems II: Express Briefs*, vol. 67, no. 11, pp. 2452–2456, 2020.

[107] T. Despoisse, "5G 28 GHz high efficiency integrated phased array transceivers," Ph.D. dissertation, Univ. Bordeaux, 2020.

[108] J. Zhang, J. F. Campbell, D. C. Sweeney II, and A. C. Hupman, "Energy consumption models for delivery drones: A comparison and assessment," *Transportation Research Part D: Transport and Environment*, vol. 90, p. 102668, 2021.

[109] C. A. Balanis, *Antenna theory: Analysis and design*. John wiley and sons, 2015.

[110] A. C. Cirik, O. Taghizadeh, L. Lampe, R. Mathar, and Y. Hua, "Sum-power minimization under rate constraints in full-duplex MIMO systems," in *2016 IEEE 84th Veh. Technol. Conf. (VTC-Fall)*. IEEE, 2016, pp. 1–5.

[111] L. EEMB Co. (2010) Lithium-ion battery data sheet. [Online]. Available: http://eemb.com

[112] Sunpower. (2017) Maxeon solar cells.

[113] A. G. Escobar-Ruiz, O. Lopez-Botello, L. Reyes-Osorio, P. Zambrano-Robledo, L. Amezquita-Brooks, and O. Garcia-Salazar, "Conceptual design of an unmanned fixed-wing aerial vehicle based on alternative energy," *Int. J. Aerospace Eng.*, vol. 2019, 2019.

[114] D. Schnaufer and B. Peterson, "Realizing 5G sub-6-GHzz massive MIMO using GaN," *Microw. RF*, 2018.

[115] H. Shakhatreh, A. Khreishah, and B. Ji, "UAVs to the rescue: Prolonging the lifetime of wireless devices under disaster situations," *IEEE Trans. Green Commun. and Netw.*, vol. 3, no. 4, pp. 942–954, 2019.

[116] Y. Liu and J. Wang, "Low-complexity ofdm-based hybrid precoding for multiuser massive mimo systems," *IEEE Wireless Commun. Lett.*, vol. 9, no. 3, pp. 263–266, 2019.

[117] Z. Li, H. Hu, J. Zhang, and J. Zhang, "Enhancing indoor mmwave wireless coverage: Small-cell densification or reconfigurable intelligent surfaces deployment?" *IEEE Wireless Commun. Lett.*, vol. 10, no. 11, pp. 2547–2551, 2021.

[118] M. Naderi Soorki, W. Saad, M. Bennis, and C. S. Hong, "Ultra-reliable indoor millimeter wave communications using multiple artificial intelligence-powered intelligent surfaces," *IEEE Tran. Commun.*, vol. 69, no. 11, pp. 7444–7457, 2021.

[119] M. McCloud and L. Scharf, "A new subspace identification algorithm for high-resolution doa estimation," *IEEE Trans. Antennas and Propagation*, vol. 50, no. 10, pp. 1382–1390, 2002.

[120] E. Soltanaghaei, A. Prabhakara, A. Balanuta, M. Anderson, J. M. Rabaey, S. Kumar, and A. Rowe, "Millimetro: mmwave retro-reflective tags for accurate, long range localization," in *Proc. 27th Annual Int. Conf. Mobile Computing and Networking*, 2021, pp. 69–82.

[121] M. H. Mazaheri, A. Chen, and O. Abari, "mmtag: a millimeter wave backscatter network," in *Proc. ACM SIGCOMM 2021 Conference*, 2021, pp. 463–474.

[122] T. T. Cai and L. Wang, "Orthogonal matching pursuit for sparse signal recovery with noise," *IEEE Trans. Info. Theory*, vol. 57, no. 7, pp. 4680–4688, 2011.

[123] 3GPP. (2018) 5G NR; User Equipment (UE) radio transmission and reception; Part 2: Range 2 Standalone, Rel-15. 3GPP TS 38.101-2 V15.2.0.

[124] A. Baddeley, I. Bárány, and R. Schneider, "Spatial point processes and their applications," *Stochastic Geometry: Lectures notes*, pp. 1–75, 2007.

Publications

Refereed Journals

(i) **N. Varshney** and S. De, "Optimum downlink beamwidth estimation in mmWave communications," *IEEE Trans. Commun.* , vol. 69, no. 1, pp. 544-557, Jan. 2021.
(Chapter 2)

(ii) **N. Varshney** and S. De, "Multi-RF Beamforming-Based Cellular Communication Over Wideband mmWaves," *IEEE Trans. Commun.* , vol. 70, no. 4, pp. 2772-2787, April 2022.
(Chapter 3)

(iii) **N. Varshney** and S. De, "RF Beamforming and Subcarrier Allocation Using Beam Squint in mmWave Systems," *IEEE Wireless Commun. Lett.* , vol. 11, no. 4, pp. 678-682, April 2022.
(Chapter 4)

(iv) **N. Varshney** and S. De, "Design optimization for UAV aided sustainable 3D wireless communication at mmWaves," *IEEE Trans. Veh. Technol.*, vol. 72, no. 3, pp. 3274-3287, March 2023.
(Chapter 5)

Refereed Conferences

(i) **N. Varshney** and S. De, "Joint Beamwidth and Number of Concurrent Beams Estimation in Downlink mmWave Communications," in *Proc. Nat. Conf. Commun. (NCC)*, Kanpur, India, pp. 1-6, 2021.
(Chapter 3)

(ii) **N. Varshney**, R. Ghazalian, R. Jäntti, and S. De, "BackScatter-assisted Indoor mmWave Communications with Directional Beam at User," in *Proc. IEEE Int. Conf. Commun. (ICC)* 2023. (Accepted Jan. 2023)
(Chapter 6)

Biodata of the Author

Nancy Varshney

Email Id: Nancy.Varshney@dbst.iitd.ac.in, nancyv.ece16@itbhu.c.in

Education

July 2018-April 2023	**Doctor of Philosophy (Ph.D.)** Bharti School of Telecommunication Technology & Management, Indian Institute of Technology Delhi, New Delhi, India CPGA 9.00 | Division I
July 2016-June 2018	**Master of Technology (M. Tech.)** Department of Electronics Engineering, Indian Institute of Technology, Banaras Hindu University, Varanasi, Indial Graduated, June 2018 CGPA 9.53 | Division I
July 2011- May 2015	**Bachelor of Technology (B. Tech.)** Department Electronics & Communication Engineering, Moradabad Institute of Technology, Dr. A.P.J Abdul Kalam Technical University, Lucknow, India Percentage 81.36% | Division I Honors
July 2009-May 2011	**Intermediate** St. Paul's College, ISC Board Moradabad, Uttar Pradesh Percentage 89.93%
June 2009	**High School** St. Paul's College, ISC Board Moradabad, Uttar Pradesh Percentage 90.85%

Current Research Interests

- Beamforming for 5G and beyond communication networks

- Design of beamforming at wideband mmWave networks
- RIS-aided communications for wideband mmWave networks
- UAV-assisted communications for mmWave networks
- Energy harvesting and communication for backscatter systems at mmWaves

Academic Projects

- Ph.D. Dissertation: Optimal Beamforming Strategies At mmWaves for 5G+ Networks
  Supervisor: Prof. Swades De, IIT Delhi
  The objective of the dissertation was to investigate and design energy and spectrally efficient reduced complexity terrestrial and aerial mmWave communications frameworks/architectures with a limited number of RF chains for 5G and beyond (5G+) communication networks.

- M. Tech. Thesis: Anti-jamming Techniques for LTE Networks
  Supervisor: Dr. K. V. Srinivas, IIT BHU, India
  The objective of the thesis was to design a precoding schemes to make downlink LTE communications. The work involved modeling and system-level simulations in MATLAB.

- B.Tech Project: Design of Automatic Guitar Tuner
  Mentor: Dr. Kshitij Shinghal, Moradabad Institute of Technology
  A prototype of an automatic guitar tuner was designed using an AT89S52 microcontroller to wind and unwind the strings to reach the desired frequency by bypassing the musician's efforts of tuning guitar strings.

Awards, Honors and Scholarships

- Awarded **MediaTek-India Research 2022** fellowship
- Visiting scholar under Prof. Riku Jäntti in Aalto University, Finland, from June 2022-October 2022

- Recipient of the **Best Paper Awards** presented at the National Conference on Communications, 2021
- Assistantship by Ministry of Human Resource and Development, Government of India during M. Tech. from July 2016 - May 2018
- Secured 1031 All India Rank in Graduate Aptitude Test in Engineering (GATE) 2016
- Institute scholarship by Dr. A.P.J Abdul Kalam Technical University during B. Tech. from July 2011- May 2015
- Secured 2nd position at Moradabad Institute of Technology, Moradabad during B. Tech.

Peer Reviewer for Notable Journals

- IEEE Transactions on Communications
- IEEE Communications Letters
- IEEE Wireless Communications Letters
- IEEE Transactions on Vehicular Technology
- Elsevier Computer Communication
- IEEE Global Communications Conference (GLOBECOM)
- IEEE International Conference on Communications (ICC)

Position of Responsibilities

- Teaching assistant in EC-521 (Decision and Estimation Theory) course at IIT BHU, Varanasi (July-Nov'17)
- Teaching assistant in ELL-205 (Signals and Systems) course at IIT Delhi (July-Nov'18, July-Nov'19)
- Teaching assistant in ELL-725 (Wireless Communications Theory) course at IIT Delhi (Jan-April'20, July-Nov'19)

- Teaching assistant in ELP-725 (Wireless Communications Lab) course at IIT Delhi (Jan-April'20, Jan-April'23)